FINAL REPORT

For the period: August 1, 2002 - July 31, 2004

for

NASA grant NAG5-12407

Precipitation Modeling over the Greenland and Antarctic Ice Sheets and the Relationship to the Surface Mass Balance and Climate

Principal Investigator: David H. Bromwich

Co-Principal Investigator: Qiu-shi Chen

25 July 2005

Table of Contents

5. Modeled Antarctica precipitation and mass balance

1. Methodology for precipitation modeling over Greenland and Antarctica

1.1 Polar MM5 and regional climate simulation

The local or regional climate can be analyzed by using observations but descriptions are incomplete because the observations are concentrated at low elevations. In particular it is difficult or impossible to analyze the wind fields and precipitation forced by terrain using only observational data. Two alternative modeling approaches can be used to reconstruct regional historical climate. One is regional reanalysis in which a state-of-the-art data assimilation system is used to reprocess all past environmental observations by combining them with short-term forecasts that are driven by global reanalysis at the lateral boundaries (such as North American Regional Reanalysis, http://www.emc.ncep.noaa.gov/mmb/rreanl/). However, regional reanalysis is too complicated and computationally demanding to use for most regional climate applications. The other approach is regional climate simulation using a regional climate model or weather forecasting model in a limited area where the horizontal resolution typical for the mesoscale is applied to a small region of interest.

Regional climate simulations, based on the concept of "dynamic downscaling" and implying that regional climate is conditioned but not completely determined by the larger scale state, consistently improve the spatial and temporal detail of simulated climate compared to global climate models (GCMs) (Rinke et al. 1999a,b; Rinke and Dethloff 2000). They show promise in being able to reproduce the regional detail in surface climate as forced by topography, lakes, coastlines and variations in land surface type. A global model provides the lateral boundary conditions for the regional climate model. However, the difference in horizontal resolution between the global and regional models (a factor of ~5) needs to be addressed with respect to the treatment at the lateral boundaries (von Storch et al. 2000).

Several approaches are generally used to simulate regional climate. One is long period simulations that have the advantage of keeping the long-term forcing uninterrupted but the model atmosphere in the domain interior can drift from the observations because of model limitations such as inaccurate numerics and errors in physical parameterizations (Pan et al. 1999, Qian et al. 2003). Long period simulation is often used for climate sensitivity studies to investigate the regional response to a particular forcing.

Another regional climate simulation method is dynamical downscaling using short segment integrations which applies a numerical weather prediction model to hindcast regional or local atmospheric states from global analysis data. This method can minimize possible drift caused by accumulated model errors but the spin up problems introduced by the reinitializations must be addressed. With this method the atmospheric behavior is determined not only by the model physical processes along with regional terrain and land use but also by the initial conditions. The short segments are generally less than 72 hours with 6-24 hours spin up time. Because of the short integration time, the effects of lateral boundary errors are minimized. Regional climate simulation studies of the Greenland area using this method obtained skillful results (Bromwich et al. 2001, Cassano et al. 2001, Box et al 2004) in part because the large scale flow in the middle and upper troposphere is across the integration domain.

a. Polar MM5

The Polar MM5 model is a regional atmospheric model based on the PSU–NCAR MM5 (Dudhia 1993, Grell et al. 1994), and has been adapted specifically for ice sheet environments

by the Polar Meteorology Group of the Byrd Polar Research Center at The Ohio State University (Bromwich et al. 2001a; Cassano et al. 2001). This model is being used to produce real-time mesoscale and synoptic forecasts in the Antarctica (Powers et al. 2003), and it has proved to be skillful in simulating the atmospheric circulation over polar regions (Cassano et al. 2001; Bromwich et al. 2001a; Guo 2002; Guo et al. 2003). Given the skill present in Polar MM5 simulations over polar ice sheets, the model output can be used to study the precipitation and accumulation over Greenland and Antarctica. The changes made to the standard version of MM5 for use in polar regions are summarized below. This is followed by a description of the model configuration used for each simulation.

For the Polar MM5 simulations, moist physics are solved with the explicit cloud and precipitation prediction scheme (Dudhia 1993; Grell et al. 1994). The Reisner explicit microphysics parameterization (Reisner et al. 1998) is used to represent the resolvable scale cloud and precipitation processes, and the Grell parameterization (Grell et al. 1994) is used to represent the subgridscale cloud processes. In order to eliminate the cloudy bias in polar simulations with MM5 the equation for ice nuclei concentration from Meyers et al. (1992) was used to replace the Fletcher (1962) equation in the explicit microphysics parameterization.

The transfer of shortwave and longwave radiation through the atmosphere is predicted with a modified version of the NCAR Community Climate Model, version 2 (CCM2), radiation parameterization (Hack et al. 1993). For the Polar MM5 simulations, the cloud ice and cloud water paths and their radiative effects are included in the modified CCM2 radiation parameterization, and predicted cloud water and ice mixing ratios from the Reisner explicit microphysics parameterization are used to determine the radiative properties of the modeled cloud cover.

Turbulent fluxes in the atmosphere, and the turbulent fluxes between the atmosphere and the surface, are parameterized using the 1.5-order turbulence closure parameterization used in the NCEP Eta Model (Janjic′1994). Heat transfer through the model substrate (i.e., snow and ice) is predicted using a multiplayer "soil" model.

b. Regional climate simulation for Iceland and Greenland

For this project, the nonhydrostatic Polar MM5 has been applied to simulate the regional climate and surface mass balance for Greenland and Iceland using forcing at the lateral boundaries from the European Centre for Medium-Range Weather Forecasts Tropical Ocean - Global Atmosphere (ECMWF TOGA) operational analyses. Three nested model domains (Fig. 1.1) are used to get reasonable lateral boundary conditions from the global analyses for the mesoscale simulation. The horizontal resolution and grid points are 72km, 85x73 for domain 1; 24km, 103x121 for domain 2; and 8km, 85x73 for domain 3. The vertical discretization consists of 28 irregularly spaced σ-levels. The model top is set at 10 hPa and the rigid lid upper boundary condition is used. The model physics options are: mixed phase explicit moisture scheme for three domains (Reisner et. al. 1998); Grell cumulus scheme; CCM2 atmospheric radiation scheme; and the MRF planetary boundary layer scheme. The 2.5° horizontal resolution ECMWF TOGA surface and upper air operational analyses are used to provide the initial and lateral boundary conditions for the model. The integration strategy for 1991-2000 is a sequence of 30 h simulations, with the first 6h being discarded for spin-up reasons. Model output at 6h intervals was saved for analysis. A sixth-order finite-difference scheme (Chu and Fan 1997) is implemented here to calculate the horizontal pressure gradient force more accurately to reduce the computational error and improve the simulation over the steep topography.

2
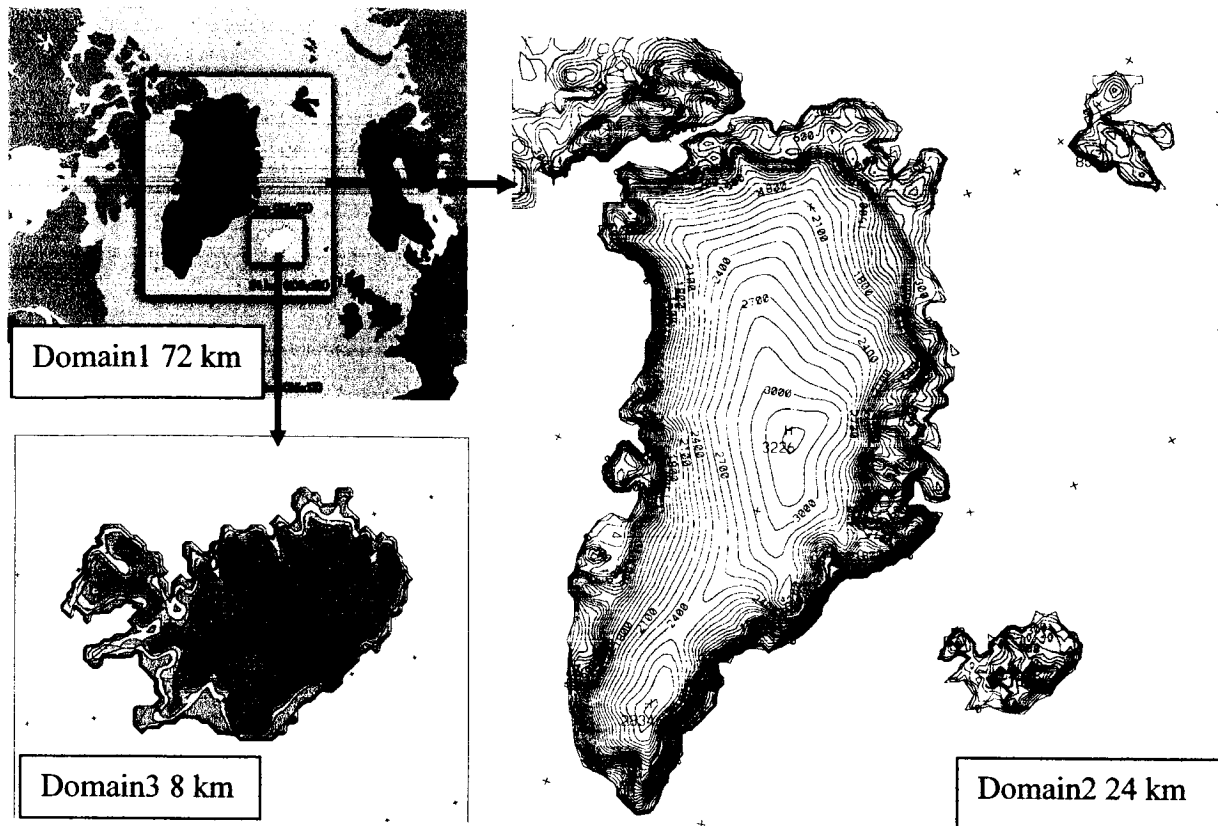
Figure 1.1 The North Atlantic model domains and terrain, elevation contour interval is 100m.

c. Regional climate simulation for Antarctica

For the precipitation simulations over Antarctica, a square model domain is used and consists of 120 grid points in each direction, centered at the South Pole, with a horizontal resolution of 60 km (Fig 1.2). The top pressure is set at 10 hPa, and a rigid lid upper boundary condition is used in the simulations. A total of 32 sigma levels are used in the vertical, of which seven are located within the lowest 400 m of the atmosphere. The lowest sigma level is located at a nominal height of 12 m above ground level (AGL). This relatively high resolution near the surface is required to accurately represent the evolution of the shallow katabatic layer over the Antarctic ice sheet. The model topography data over the Antarctic continent are also interpolated from the 5 km resolution DEM data of Antarctica (Liu et al., 1999). The areas for Filchner-Ronne Ice Shelf and Ross Ice Shelf are manually identified from climatic maps. The surface height and landuse type for both ice shelves are set 50 m and permanent ice with constant albedo of 0.80, respectively.

The ECMWF TOGA surface and upper air operational analyses are used to provide the initial and boundary conditions for the model atmosphere. The 1.125° ECMWF TOGA global surface analyses are used to specify the initial surface temperature (and sea surface temperature) and model substrate soil temperature. The daily polar gridded sea ice concentration data with 25- km horizontal resolution obtained from the National Snow and Ice Data Center are used to identify the sea ice surface type and its fractional coverage at each model grid. The Polar MM5 is used to produce short duration (36 h) simulations of the atmospheric state over Antarctica

3

from July 1996 through June 1999. This 36 month period had two well-defined cold events with positive Southern Oscillation Index (SOI) values in 1996 and 1998/99 and a warm event with negative SOI values in 1997/98, and was selected to capture the temporal variability of Antarctic precipitation over an entire ENSO cycle. The model is initialized with the 00 UTC ECMWF analyses for each preceding day, with the 12–36 h forecasts used for data analyses. Using the 12-36 h forecasts allows for model "spin up" to resolve inconsistencies in the initial conditions.
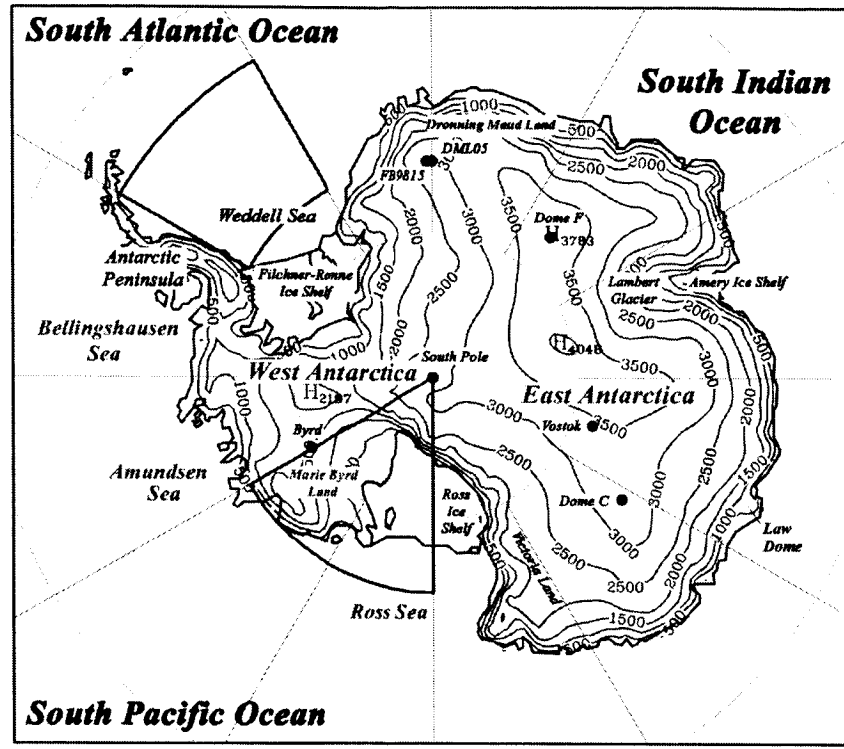
Figure 1.2. Antarctica with topographic features and West Antarctic sectors that are of particular interest. The dots indicate the locations of stations used in this study. Elevation contour interval is 500 m.

1.2 Dynamic retrieval method for precipitation prediction over Antarctica

The dynamic retrieval method (DRM) uses the dynamic association among meteorological variables to retrieve precipitation values. Bromwich et al. (1993) use a statistical diagnostic approach to calculate precipitation over Greenland from the advection of relative geostrophic vorticity at the 500-hPa level. Chen et al. (1997a) and Bromwich et al. (2001a) developed this method to derive the precipitation over Greenland from a vertical motion calculation, and it has proved to be a relatively economical method to retrieve the snow accumulation over Greenland with good spatial and temporal resolution. The topographic effects on precipitation and atmospheric motion are greatly influenced by the computational accuracy of the horizontal pressure gradient force over mountainous regions (Colle et al. 1999), especially near the steep slopes of mountains and ice sheets. In order to improve the estimation of precipitation over steep slopes, the equivalent geopotential and geo-streamfunction in σ-coordinates are used in the generalized ω-equation.

The equivalent geopotential height φ_e is derived from the solution of the following equation (Chen and Bromwich 1999):

$$\nabla^2 \phi_e = \nabla^2 \phi + \left[\frac{\partial}{\partial x}\left(RT \downarrow \frac{\partial \ln p_*}{\partial x} \right) + \frac{\partial}{\partial y}\left(RT \downarrow \frac{\partial \ln p_*}{\partial y} \right) \right], \tag{1.1}$$

where φ, T, and $p*$ are geopotential height, temperature, and surface pressure in σ- coordinates, respectively, and R is the gas constant for dry air. For a limited region, the equivalent isobaric geopotential, and geopotential in σ-coordinates can be separated into its inner part φ_{ei}, φ_i and harmonic part φ_{eh}, φ_h (Chen and Kuo 1992) as:

$$\varphi_e = \varphi_{eh} + \varphi_{ei}, \quad \varphi = \varphi_h + \varphi_i \tag{1.2}$$

Based on (1.1), the inner part of the equivalent isobaric geopotential height in σ- coordinates φ_{ei} can be derived from the solution of the following Poisson equation:

$$\nabla^2 \phi_{ei} = \nabla^2 \phi_i + \left[\frac{\partial}{\partial x}\left(RT \downarrow \frac{\partial \ln p_*}{\partial x} \right) + \frac{\partial}{\partial y}\left(RT \downarrow \frac{\partial \ln p_*}{\partial y} \right) \right], \tag{1.3}$$

with zero Dirichlet boundary value.

The vorticity and divergence equations can be transformed into the equations of the inner parts of the streamfunction and velocity potential, respectively, and they are expressed by

$$\frac{\partial \psi_i \downarrow}{\partial t} + f_0 \chi_i \downarrow = \psi_{adv,i} \downarrow \tag{1.4}$$

$$\frac{\partial \chi_i \downarrow}{\partial t} + \phi_{e,ia} \downarrow = \chi_{adv,i} \downarrow - E_i \downarrow \tag{1.5}$$

where $E_i = [m^2(U^2 + V^2)_i / 2]$, ψ_i and φ_i are inner parts of the streamfunction and velocity potential, respectively, the terms $\psi_{adv,i}$ and $\chi_{adv,i}$ are the variation rates of the inner parts of the streamfunction and velocity potential caused by advection, and m is the map scale factor.

The inner part of the ageostrophic geopotential φ_{eia} (the difference between φ_{ei} and geostrophic geopotential $\varphi_{eig\,i} = f_0\psi_i$ can be written as (Chen et al. 1997b)

$$\frac{\partial \phi_{e,ia} \downarrow}{\partial t} + m_0^2 A \nabla^2 \chi_i \downarrow - f_0^2 \chi_i \downarrow = \Phi_{e,had,ia} \downarrow + m_0^2 A \nabla^2 \chi_{hi} \downarrow, \square \tag{1.6}$$

where m_0 is the average value of the map scale factor in the integration region. $\varphi_{e,had,i}$ is the variation rate of the geopotential caused by advection and diabatic heating, and A is a matrix comprised of T and σ with units of J kg^{-1} (Chen et al. 1997b). Here

$$D_h = D - D_i \tag{1.7}$$

where D_i and D_h are the inner and harmonic parts of the divergence, respectively (Chen and Kuo 1992) If the tendency of ageostrophic geopotential in (1.6) is neglected, this approximation is referred to as a balanced ageostrophic approximation (Chen et al. 1996). Thus, equation (1.6) becomes:

$$m_0^2 A \nabla^2 \chi_i \downarrow - f_0^2 \chi_i \downarrow = \Phi_{e,had,ia} \downarrow + m_0^2 A \nabla^2 \chi_{hi} \downarrow. \tag{1.8}$$

Equation (1.8) is a velocity potential form of the generalized φ-equation for the balanced ageostrophic approximation in σ-coordinates. In this equation, the diabatic and advection terms computed by the ageostrophic wind are the same as those in the generalized φ-equation in p - coordinates (Pauley and Nieman 1992), but the effect of orography on the vertical motion is much better described than that in p-coordinates. If equation (1.8) is transformed into p-coordinates, and the term $\varphi_{e,had\,,ia}$ is computed by the geostrophic wind and expressed by

5

$\varphi_{e,had,ia,g}$, equation (1.8) becomes a velocity potential form of the quasigeostrophic ω-equation. In order to reduce computational errors in the solution of (1.8), a harmonic-sine spectral method (Chen and Kuo 1992) is used. It is seen from the above that the equivalent geopotential is used to develop a generalized φ-equation in σ-coordinates, and this equation can be used to improve ω-calculation over mountainous regions. Using the continuity equation and vertical finite differencing, the pressure vertical velocity ω in σ-coordinates can be calculated by

$$\left(\frac{\omega}{p}\right)\downarrow = m^2(I-C)\left(U\downarrow\frac{\partial \ln p_*}{\partial x} + V\downarrow\frac{\partial \ln p_*}{\partial y}\right) - m^2 CD\downarrow,$$

(1.9)

where I is a unit matrix, C is a lower-triangular matrix comprised of and its vertical difference (Chen et al. 1997b), and u, v are the horizontal wind components. Only large scale condensation is considered (Haltiner and Williams 1980, p. 309) in computing precipitation. The condensation rate can be expressed by

$$\frac{dq_s}{dt} = \delta F\omega, \quad F = \frac{q_s T}{p}\left(\frac{LR - C_p R_v T}{C_p R_v T^2 + q_s L^2}\right).$$

(1.10)

where condensation from saturated air is denoted by dq_s/dt , q_s is the saturation specific humidity, L is the latent heat of condensation, Cp is the specific heat of the air at constant pressure, and Rv is the gas constant for moist air. The Kronecker δ is used to indicate the assumption that the condensation begins at some critical relative humidity r_c when upward vertical motion is present. r_c is a tunable parameter in the model. In this paper, the critical relative humidity r_c is assumed to be 94 percent based upon model tests over the Antarctica continent with different r_c values (the value was found to be relatively insensitive to elevation).

If all of the condensate from saturated expansion is assumed to fall instantly as precipitation, the precipitation per unit area can be calculated from vertical integration of condensation rate dq_s/dt. The precipitation is calculated twice per day based on the ECMWF TOGA at 0000 and 1200 UTC for 1985-1999 and four times a day based on ERA-15 at 0000, 0600, 1200, and 1800 UTC for the years 1979-1993. The retrieved precipitation is produced from the dynamic retrieval mothed with ECMWF reanalysis (1979-1990) and operational analyses (1991-1999). The annual precipitation is derived by adding daily precipitation amounts for the whole year. The 22 σ-levels are used in the vertical, and a 40-km grid size is used in the horizontal. The square model domain used in this study consists of 181 grid points in each orthogonal direction, centered at the South Pole, with a horizontal polar stereographic projection resolution of 40 km (Fig. 1.2). The model topography data over the Antarctic continent are also interpolated from a modern 5-km resolution digital elevation model (DEM) of Antarctica (Liu et al. 1999) using bi-linear interpolation from the nearest points.

2. Climate simulation for Greenland using Polar MM5.

2.1 Background

Greenland, an island the size of the Tibetan Plateau that is 80% covered with ice, has been attracting scientific attention since late 19th century. During the past decade, climatic change and the influence of Greenland have been addressed. Based on the studies of precipitation over Greenland from 1963-1988, Bromwich et al. (1993) discussed the implications for global sea level rise associated with the downward trend in Greenland precipitation. Ice core studies from the summit of the ice sheet provided invaluable information on Earth's climate history (e.g. McManus et al. 1994; Kapsner et al. 1995, Brook et al. 1996). These studies showed that climate variability was much greater near the end of the last glacial period when annual-average temperature changes of about $10°C$ occurred on time scales of years (e.g. Taylor et al. 1993, Taylor et al. 1997, Grootes et al. 1993, Grootes and Stuiver 1997). Kapsner et al. (1995) found sudden dramatic changes in ice accumulation during shifts between climatic states. Their results indicate that variations of storm track position have a profound effect on the ice accumulation, while variations in climatic temperature are much less important; this conclusion is entirely consistent with findings from the modern environment (Bromwich et al. 1993).

The NAO is known to have a variety of important climatic impacts for the North Atlantic basin (Rogers and van Loon 1979, Hurrell 1995). Reductions in Greenland ice accumulation over recent years obtained by Bromwich et al. (1993) can be explained by the tendency towards positive NAO index. Using an ω equation method based on an equivalent isobaric geopotential height in σ coordinates, Bromwich et al. (1999) retrieved the precipitation over Greenland from 1985-1996. They found that if the NAO index increases, the total winter (DJF) precipitation over Greenland decreases, and vice versa. The correlation coefficient between them is −0.75. Over the southern Greenland, where the majority of precipitation falls, this correlation is up to −0.8.

In this study, the regional climate simulation results (domain2, Fig 1.1) (1991-2000) are used to study the climate of Greenland. The main focus of this study is to examine the surface climate of Greenland during different NAO phases, as monitored by Rogers's NAO index (http://polarmet.mps.ohio-state.edu/NAO) (Rogers 1984).

2.2. Verification of Model Output

The verifications are based on monthly mean values. The model predicted monthly means are computed from 6 hourly model output and observed monthly mean values are computed from hourly automatic weather station (AWS) data. The comparisons between simulated and observed show that the monthly mean model values closely follow the observations (not shown). The largest differences between model output and AWS observations occur for the stations on steep slopes, which the model grid does not capture accurately. The best model skill is found for surface pressure, 2-m air temperature and 2-m mixing ratio. The monthly mean wind speed and direction comparisons show less skill because the surface wind fields are more likely affected by local factors. The 10-m model wind speed tends to be stronger than observed during winter and lighter than observed during summer. The 2-m model mixing

ratio tends to be moister than observed especially during winter. Overall the model predicts the monthly mean state variables over Greenland with high skill.

Comparison between simulated P-E (precipitation – evaporation) and annual ice sheet accumulation from PARCA ice cores is shown in Fig 2.1 for the period 1991-1997. It is expected that the overall modeled P-E is higher than the accumulation from ice core records because drifting snow effects remove mass from the surface (Box et al. 2004). The mean bias is 23% higher. The modeled P-E biases along the Greenland summit are less than the drill sites on the steep slopes where surface wind speed is larger than that around the summit. Drifting snow will remove fresh snow, expose old snow or ice, affecting the melting rate during melt season. Box et al. (2004) calculate that drifting snow sublimation (S) could remove up to 15% of ice sheet precipitation. If this percentage is taken into account, the Polar MM5 modeled P-E-S is overestimated by 8% averaged over the ice sheet.
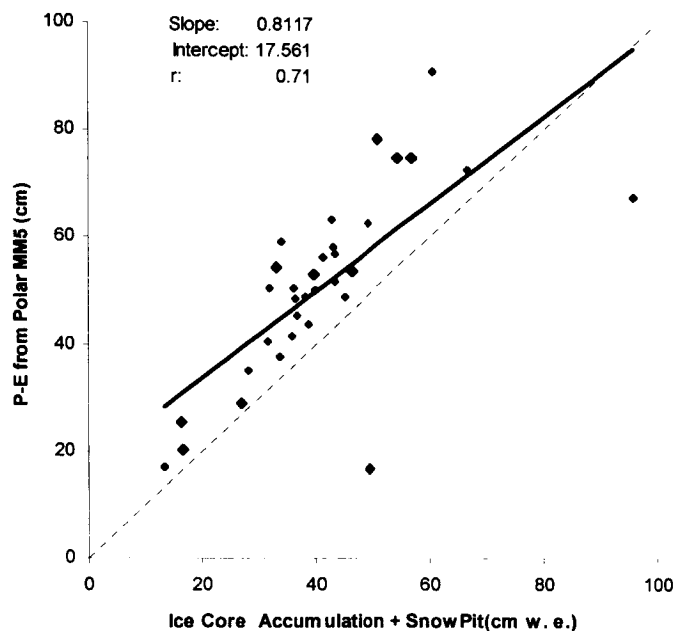
Figure 2.1 P-E from Polar MM5 and accumulation from ice cores and snow pits. The larger diamonds represent the snow pit observation, the smaller diamonds are from ice cores.

2.3. Annual and seasonal climate characteristics from the model output

a. Precipitation

Like the Antarctic Ice Sheet, the Greenland Ice Sheet functions as a major reservoir of fresh water, maintaining present global sea level. Precipitation over the Greenland Ice Sheet is the main source for its ice sheet accumulation. The variation of the precipitation over Greenland Ice Sheet is very important for climate change. Figures 2.2(a) and (b) show the observed annual mean precipitation (cm/year water equivalent) from 1950 to 2000 (from ice cores, coastal weather station and AWS data, and compiled by B. Csatho) and the annual mean precipitation (1991-2000) simulated by Polar MM5, respectively. Comparing the simulated long-term mean annual precipitation by Polar MM5 for 1991-2000 to the observed long-term annual mean, it is

8

seen that the annual mean precipitation distribution over Greenland is reasonably well simulated by Polar MM5.
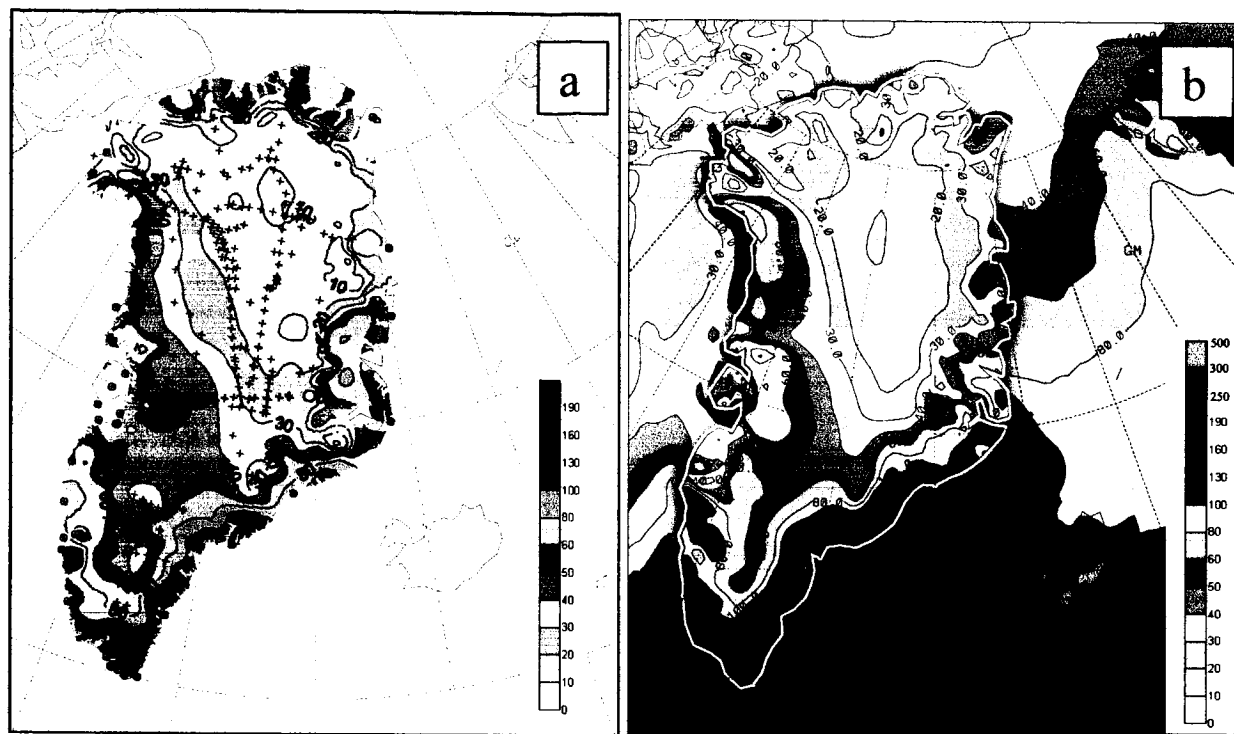
Figure.2.2 (a) Observed annual mean accumulation (cm/year water equivalent) from 1950 to 2000 (from ice cores, coastal weather station and AWS data) and (b) the annual mean precipitation (1991-2000) simulated by Polar MM5 V3.5 (units: cm/year).

The largest precipitation occurs in the southern part of Greenland. More precipitation is simulated along the coast than in the interior. Maximum precipitation is found along the southeastern coast. Along the western side of Greenland, the southwestern coast has more precipitation than the northwestern coast. From the middle of the western coast to the interior between the two peaks of the Greenland Ice Sheet, a large amount of precipitation is simulated by Polar MM5, which is reviewed by Csatho et al. (1997). From the interior of Greenland (near Summit) to the northern coast, the precipitation is very small. The large coastal precipitation is due to the cyclone activity in adjacent regions. The mid west coast maximum and the northwest coastal precipitation center in Greenland are related to the cyclone activity over open sea or polynyas.

Figure 2.3 shows seasonal precipitation from Polar MM5 simulations. The mean seasonal precipitation for spring (MAM), summer (JJA), autumn (SON) and winter (DJF) show that the large amounts of precipitation occur along the coast for all four seasons. In spring, more precipitation occurs in southeast coast than other areas. The mean spring precipitation is less than 90cm. During summer season, the precipitation over the Greenland Ice Sheet is the least among four seasons. In autumn, there is more precipitation along the western coast than that in winter, especially in the middle and northwestern coast, indicating more cyclone activity along the west coast in autumn compared to the winter season. The autumn precipitation over the

southern tip of Greenland is larger than that in winter. Along the southeast coast, the model simulations show more precipitation in winter than in autumn.
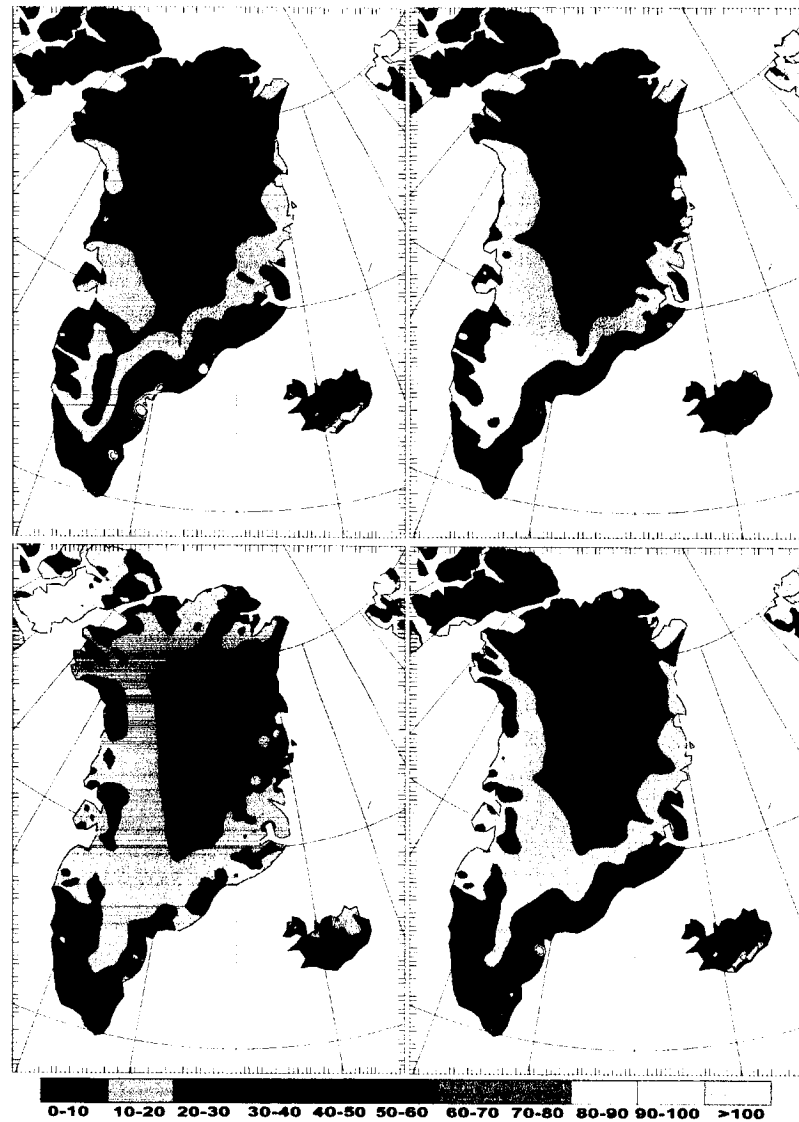
Figure 2.3 Polar MM5 predicted mean annual and seasonal precipitation (cm) from 1991 to 2000. a) DJF, b) MAM, c) JJA, d) SON. (left to right, top to bottom)

b. Surface temperature

For the annual and seasonal mean 2-meter surface air temperature (not shown), there is a cold core ($-30^\circ C$) over the summit of Greenland Ice Sheet. The 2-meter surface temperature then increases toward the coast, with a symmetric pattern on the western and eastern sides. The larger temperature gradient over southeast coast reflects the steeper terrain slope than other areas. The 2-meter surface temperature is around $0^\circ C$ to $-4^\circ C$ on the southern coast, $-8^\circ C$ to $-12^\circ C$ on the middle coast, and $-16^\circ C$ on the northern coast. From south to north, the Greenland Ice Sheet spans 22 degrees latitude, thus the mean 2-meter surface temperature gradient is around $-0.7^\circ C$ /degree latitude.

10

The surface temperature in winter is coldest at Summit ($-42^\circ C$) with the largest south to north temperature gradient. During summer, surface temperature over Summit is only half of the annual mean ($-16^\circ C$). The zero degree isotherm covers from south coast to north coast and there is no south to north temperature gradient, indicating melting along the coastal areas. The mean seasonal variation of the surface temperature at Summit is as large as $26^\circ C$, which is only half of the maximum annual range at $57^\circ C$.

2.4. NAO modulation

a. NAO distribution

The NAO index variability is most pronounced in winter, and the least pronounced in summer. Because the cyclone activity near Greenland is closely related to the NAO, the larger number of positive NAO months in winter indicates more cyclone activity around Greenland and its vicinity. The number of positive NAO months dominates in all four seasons, with winter season positive months constituting more than two thirds of the seasonal total in the 1990s. NAO reflects the strength of the Icelandic Low and subtropical High near Azores' Island. The pressure field variations (not shown) show cyclonic (negative) anomalies over Greenland and Northern Atlantic and Arctic basin. The centers are near southeast Greenland. The winter season anomaly center is located to the east of Iceland. The spring, summer and autumn anomaly centers are located over Denmark Strait, with the summer anomaly being the weakest. During summer there is a secondary negative anomaly center in the Arctic.

b. Precipitation modulation

Figure 2.4 shows the difference between average precipitation for positive and negative NAO months. It can be seen that the annual pattern can be divided into western Greenland precipitation and eastern Greenland precipitation. The dividing line (0 contour line) is from northeastern Greenland, crossing the upper eastern downwind slope, to the middle of the southeast coast. In western Greenland, except for the northwestern area, there is a large precipitation deficit. In eastern Greenland, precipitation increases when the NAO is positive. The maximum precipitation increases are located from the southeast to middle-east coasts. The NAO modulation differs from season to season. In winter, only the northeast coast's precipitation in positive NAO months is more than that in negative NAO months. All other areas have less precipitation during positive NAO months. The most negative areas are located along the southeast coast. The winter precipitation pattern is also determined by the moisture supply (moisture advection). During the positive NAO phase, the strong Icelandic Low is located over Denmark Strait. Because the surface wind close to the southeastern Greenland is parallel to the coastline, the moisture supply for the precipitation over southeastern Greenland is limited. By contrast, during the negative NAO months the Icelandic Low weakens and moves southwestward. The wind field on the eastern side of the Icelandic Low is perpendicular to the southeastern coastline of Greenland, therefore the moisture supply for this area's precipitation is maximized. When the Icelandic Low is situated in Denmark Strait, the wind field is perpendicular to the northeast coastline, resulting in more moisture flux during positive NAO months. In the negative NAO months, weaker cyclonic activity delivers less moisture flux to the northeast coast.

Serreze et al. (1995) state that more cyclones are found along the west coast of Greenland during negative NAO winters, implying more precipitation along the west coast. The sea ice distribution plays an important role in Greenland precipitation. The sea ice coverage expands over Baffin Bay and Davis Strait during positive NAO months, and vice versa in the negative NAO months. Because the sea ice distribution is affected by the surface wind direction, strong northerlies west of Greenland and westerlies south of Greenland advect the sea ice west of Greenland farther south, which reduces the moisture supply for the western Greenland.

In spring and autumn, when the sea ice west of Greenland retreats or expands, the western half Greenland still has less precipitation in positive NAO months than that in negative NAO months, since the polar vortex is still strong. The large precipitation deficits or increases between different NAO phases are found along the coast. In summer, only southeastern and northeastern Greenland have less precipitation in positive NAO months than that in negative NAO months. West coast and middle-east coasts have more precipitation in positive NAO months.
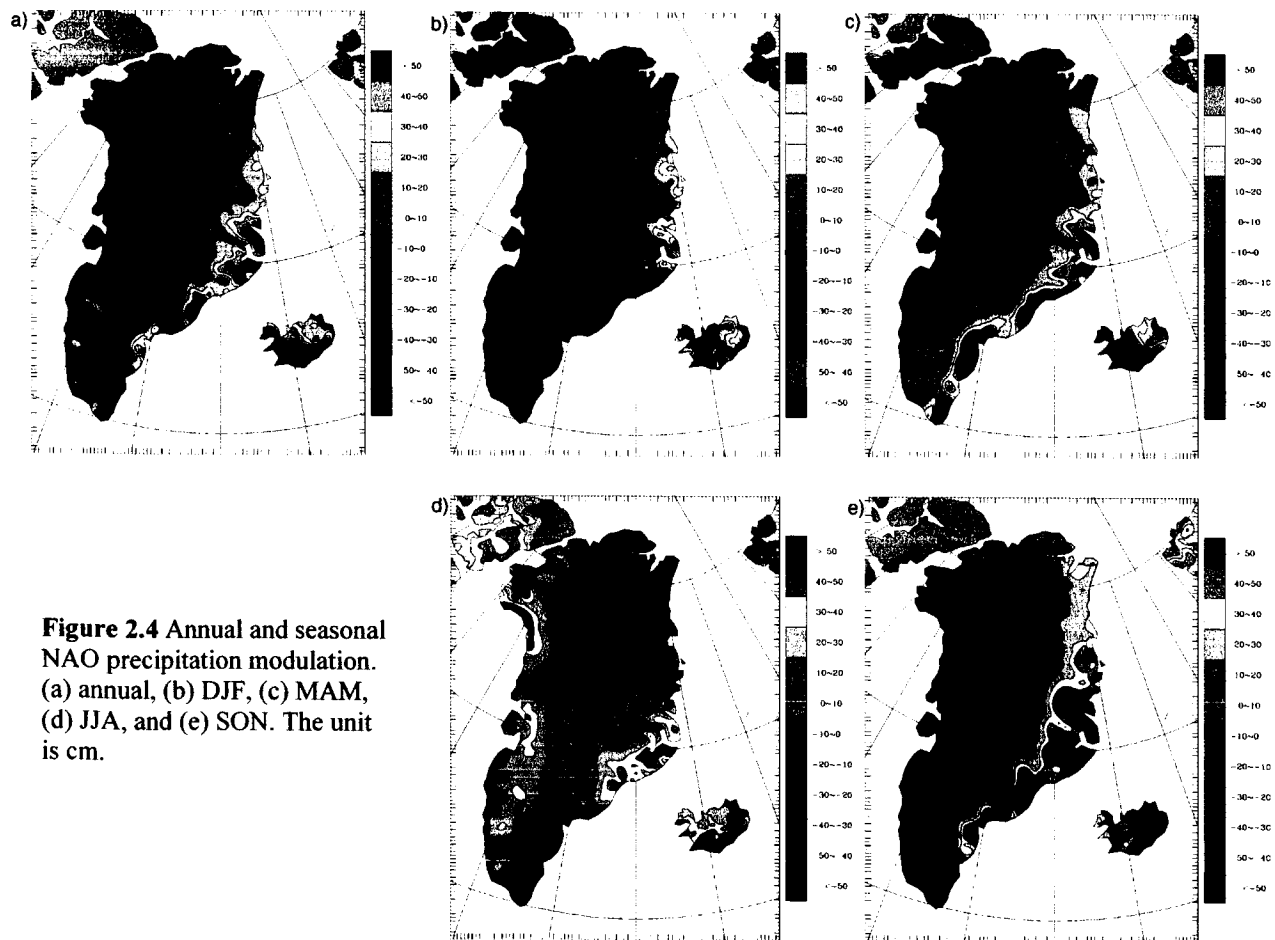
Figure 2.4 Annual and seasonal NAO precipitation modulation. (a) annual, (b) DJF, (c) MAM, (d) JJA, and (e) SON. The unit is cm.

c. 2-meter temperature modulation

The average 2-meter surface temperature has a NAO signature. The 2-meter surface temperature is colder in positive NAO months than that in negative NAO months over the entire ice sheet (not shown). The largest annual decrease $(-6.5^\circ C)$ is located in western Greenland.

The average differences along west and east coasts are $-4^{o}C$ and $-2^{o}C$, respectively. Therefore the western Greenland Ice Sheet displays more temperature change in positive NAO winters than eastern Greenland. The surface temperature modulation is closely related to the change of the large scale atmospheric circulation during different NAO phases (Rogers et al. 1998). During the positive NAO phase, there is a strong cyclonic pressure anomaly southeast of Greenland, producing strong and prevalent northerly geostrophic flow over Greenland. The northerly geostrophic flow is more pronounced over western Greenland. This northerly flow brings cold Arctic air to the Greenland Ice Sheet, with colder surface temperatures in western Greenland. For the negative NAO phase, the anticyclonic pressure anomaly generates southerly geostrophic flow over Greenland, causing the surface temperature to increase over the ice sheet. The winter and spring modulations are very similar to the annual pattern, but are stronger in spring.

In summer, the temperature modulation is less than $2^{o}C$ over the entire ice sheet. The Icelandic Low is very weak over Denmark Strait. For positive NAO summer months, a weak cyclonic pressure anomaly exists over Greenland. For negative NAO summer months, a weak anticyclonic anomaly appears over Greenland. Therefore the weak cyclonic pressure anomaly in positive NAO months creates weak northerly geostrophic flow over Greenland, and weak anticyclonic pressure anomaly produces weak southerly geostrophic flow. The northerly and southerly geostrophic flows bring cold and warm air to the Greenland Ice Sheet, respectively. The autumn temperature modulation, different from other three seasons, has one cold center located at the southwest coast and has warmer temperatures in northeastern Greenland.

2.5 Summary

The seasonal and annual precipitation patterns reflect the cyclonic activity around Greenland. The winter precipitation dominates the annual total due to the strong Icelandic Lows in winter. When seasons change from winter to summer, the precipitation along the southeast coast decreases, and the precipitation along the western coast increases.

The NAO modulation of these surface variables over the Greenland Ice Sheet is strongly associated with the change of atmospheric circulation. For positive NAO winter months, cyclonic pressure anomalies occur in Denmark Strait. Anticyclonic pressure anomalies occur in this region during negative NAO winter months. For the positive NAO summer season, the cyclonic pressure anomaly is replaced by a weak trough to the east of Greenland. This trough moves to west of Greenland during negative NAO summer months. These cyclonic/anticyclonic pressure anomalies and trough to the east/west of Greenland generate northerly geostrophic flow which brings dry and cold air from Arctic region during positive NAO months and southerly geostrophic flow which brings warm and moist air from the mid-latitude ocean during negative NAO months.

3. High Resolution Regional Climate Simulations over Iceland Using Polar MM5

Based on Bromwich, D.H. , L.S. Bai and G. B., Gudmundur, 2005: High Resolution Regional Climate Simulations over Iceland Using Polar MM5. *Mon. Wea. Rev.*, in press. Mostly supported by this project.

3.1 Background

In this study, the high resolution regional climate simulations (8km resolution) of Iceland for 1991-2000 have been performed using Polar MM5 (Fig. 1.1, domain3). Evaluation of the regional simulation over Iceland is presented in Section 3.2, and the simulation results are shown in Section 3.3. Section 3.4 summarizes the main conclusions.

3.2. Evaluation of Polar MM5 simulations over Iceland

The monthly mean climate data for 70 surface observation stations for 1991 to 2000 are used to evaluate the simulation results (Figure 3.1). The evaluation results show that Polar MM5 has very good forecast skill for monthly mean near-surface temperature, 2m dew point and sea level pressure over Iceland. For monthly mean near-surface wind speed, Polar MM5 has good forecast skill and can reasonably simulate the near-surface mesoscale wind climate over Iceland.
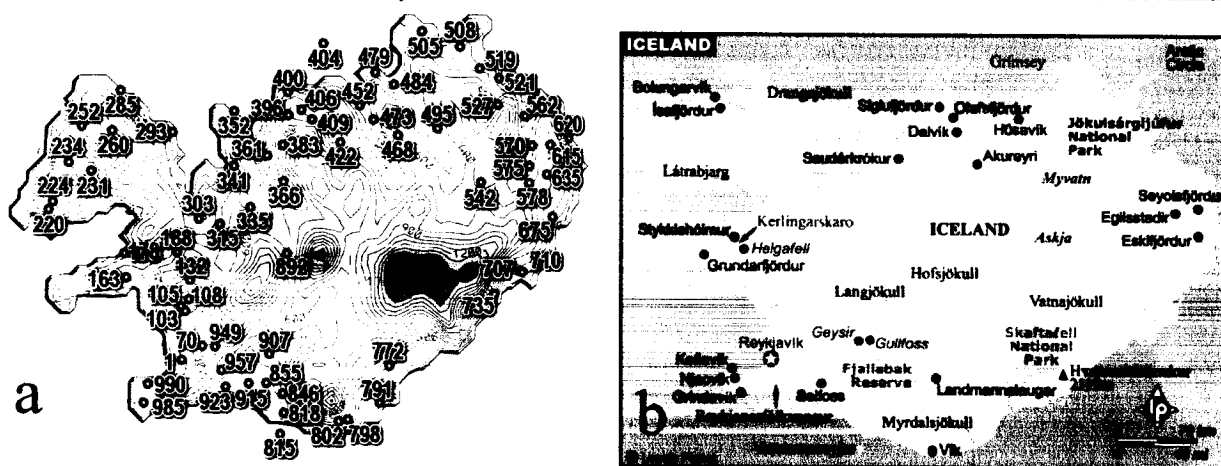
Figure 3.1. (a) Meteorological stations with monthly mean climate data for Iceland. Station numbers are given, (b) Location map of Iceland (http://www.lonelyplanet.com/mapshells/europe/iceland/iceland.htm).

The monthly mean climate data for 70 surface observation stations for 1991 to 2000 are used to evaluate the simulation results. Standard near-surface model outputs are used here. The simulated 2-m temperature is corrected from model terrain height to station elevation by using a lapse rate of 0.009 °C m^{-1}; tests showed that this value gave the best results. The modeled surface pressure is corrected from model height to sea level using the hypsometric equation and the simulated 2-m temperature.

The monthly mean near-surface temperature biases between simulated and observed values are -2.6 °C to 0.9 °C, root mean square errors (RMSs) are 0.6 °C to 2.8 °C, and the correlation coefficients are 0.98-0.99 except for five stations at which the correlation coefficient is 0.97. The mean bias, RMS and correlation coefficient are -0.9 °C, 1.4 °C and 0.99 for the seventy stations respectively. The monthly mean 2-m dew point biases between simulated and observed

are -1.9 °C to 0.9 °C, RMSs are 0.4 °C to 1.9 °C, and the correlation coefficients are 0.99 except for six stations at which it is 0.98. The mean bias, RMS and correlation coefficient are -0.3 °C, 1.0 °C and 0.99. The monthly mean sea level pressure biases are -0.47 to 0.83 hPa, RMSs are 0.54 to 0.96 hPa, and the correlation coefficients are 0.99. The mean bias, RMS and correlation coefficient are 0.1 hPa, 0.7 hPa and 0.99 respectively. Positive sea level pressure biases are found over most of Iceland. The monthly mean near-surface wind speed biases between simulated and observed are -2.5 m s^{-1} to 2.9 m s^{-1}, RMSs are 0.7 to 3.2 m s^{-1}, and the correlation coefficients are 0.48 to 0.94. The correlation coefficients at most stations are larger than 0.70, and only at eight stations are the correlation coefficients smaller than 0.60. The mean bias, RMS and correlation coefficient are 0.4 m s^{-1}, 1.6 m s^{-1} and 0.76 respectively. Slightly larger biases are found along the coast where the terrain is complicated and the model resolution is not high enough to accurately resolve it. Monthly wind direction observations were not available, but forecast directions were tested against 6 h data for January and July 1998 and found to be very accurate on average (not shown). In general Polar MM5 has reasonable forecast skill for monthly mean near-surface wind speed and can simulate the near-surface mesoscale wind climate over Iceland.

The monthly mean precipitation biases between simulated and observed are -69 to 51 mm, RMSs are 22 to 87 mm, and the correlation coefficients are 0.33 to 0.89, with the values larger than 0.60 for all except for eight stations (Fig. 3.2). The mean bias, RMS and correlation coefficient are -0.5mm, 44mm and 0.72 for the seventy stations respectively (Table 1). The simulated precipitation is larger than observed in northern Iceland and smaller in the southern part. The comparatively high correlation coefficient indicates that the Polar MM5 simulations can reasonably reproduce the monthly precipitation variability over Iceland.

The evaluation results show that Polar MM5 can reasonably simulate the spatial patterns and temporal variations of observed monthly and annual mean near-surface temperature, dew point, wind speed, sea level pressure and precipitation over Iceland, The simulation results can be used to investigate the Icelandic mesoscale climate, that is incompletely resolved by the observations.
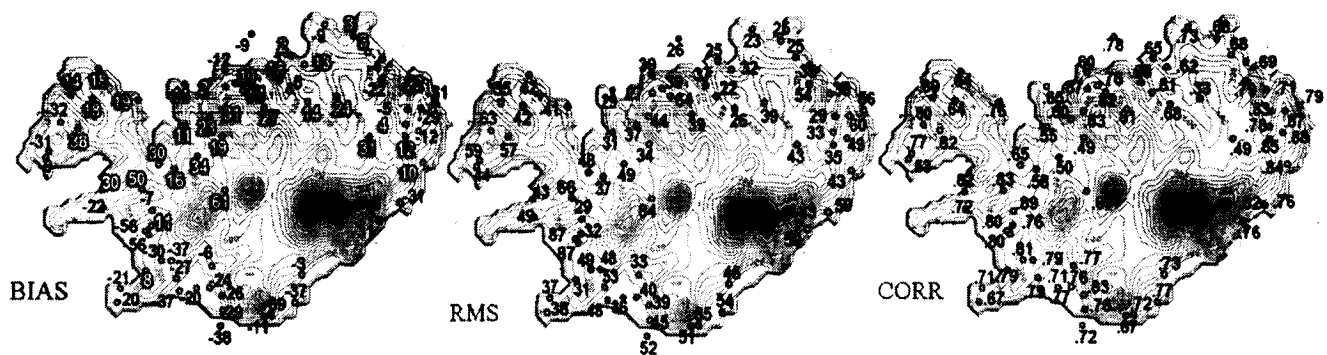
Figure 3.2. The monthly mean precipitation bias, RMS and correlation between observed and simulated by Polar MM5 from 1991 to 2000 for precipitation (mm). Terrain is shaded for reference; contour interval is 200m. Positive bias values are highlighted.

3.3. Simulation results

3.3.1 Long-term mean annual precipitation

Modeling the spatial and temporal distribution of precipitation is one of the most challenging problems for mesoscale regional climate simulations. The seasonal changes in the cyclonic circulation lead to the annual cycle of precipitation and the spatial distribution of precipitation follows the terrain. Furthermore, climate variability in Iceland is enhanced by the NAO phenomenon, primarily during the colder months. As a result of these factors, precipitation is extremely variable in space and time. In a general sense, there are two precipitation seasons, one wet that occurs from October through April, and the other dry from May through September. The annual distribution of precipitation over Iceland is directly dependent on the position of the Icelandic Low.
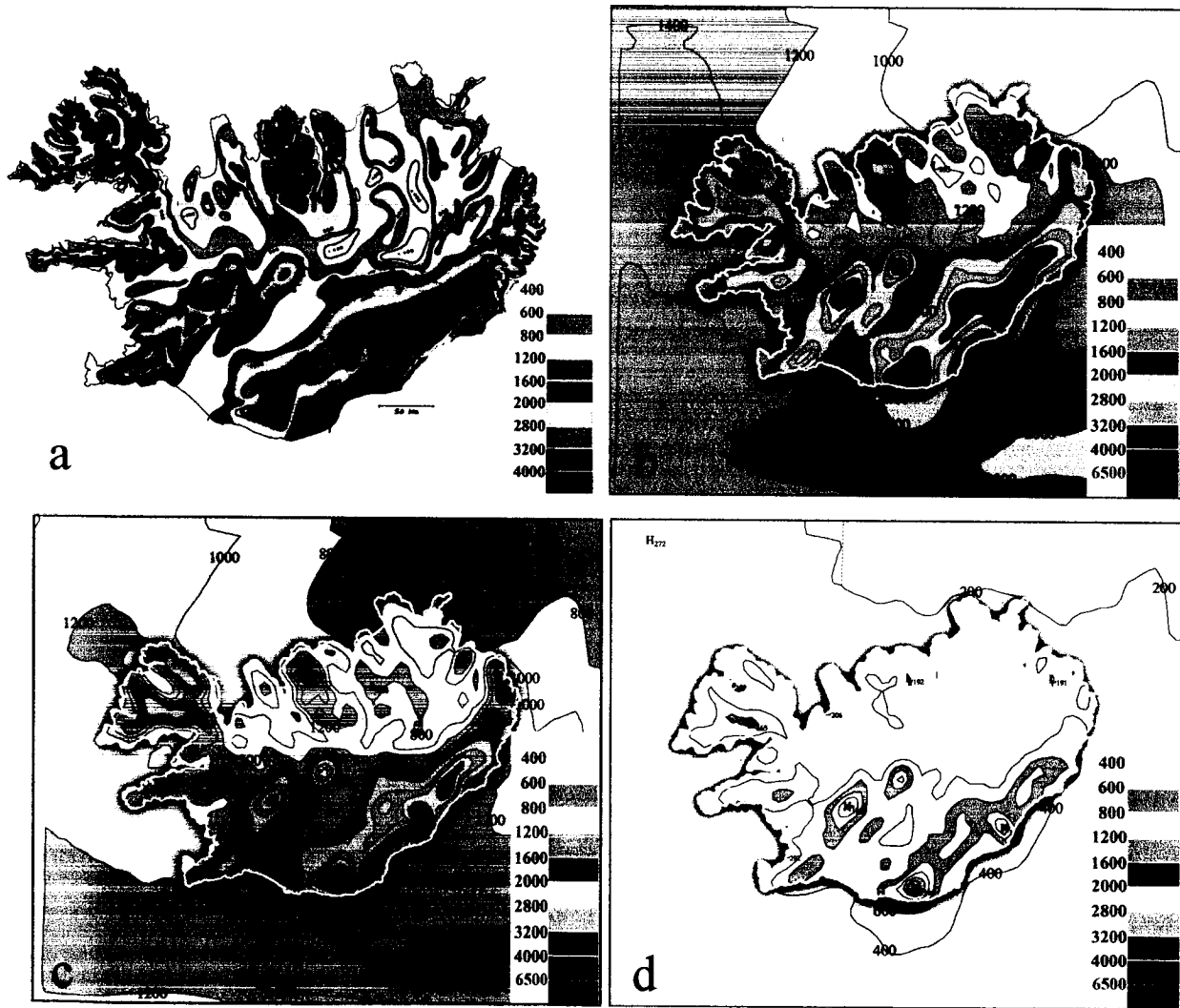
Figure 3.3. (a) The observed mean annual precipitation distribution for 1931-1960 which is derived from station precipitation observations and supplemental data (unit: mm). (b) The annual mean precipitation in (1991-2000) simulated by Polar MM5 V3.5 (unit: mm), (c) The mean winter precipitation for 1991-1999 (September 15 to April 30) simulated by Polar MM5 (mm). (d) Same as (c) but for summer (May 1 – September 14).

The observed mean annual precipitation distribution for 1931-1960 is shown in Fig. 3.3a. This analysis is derived from mostly low elevation station precipitation observations (not corrected for systematic errors, like wind effects) and supplemented by hydrologic observations

and snow accumulation measurements for subjective evaluation in areas with no direct precipitation data (Einarsson 1984; T. Jonsson, personal communication, 2004). The minimum annual precipitation is about 400 mm yr^{-1} and occurs on the northeastern basin regions of Myvatn and Askja. The mountain zones have an average annual precipitation of 2800 mm yr^{-1}. The heaviest precipitation is located near the southeast coast of Iceland, with average values of about 3000 mm yr^{-1} and maxima exceeding 4000 mm yr^{-1} over Myrdalsjökull and south of Vatnajökull. Given that the relationship between large and regional/local scale atmospheric behavior is highly nonlinear (Moss et al. 1994), atmospheric physically-based models need to be extended to these regions and scales to complement approximate observational syntheses.
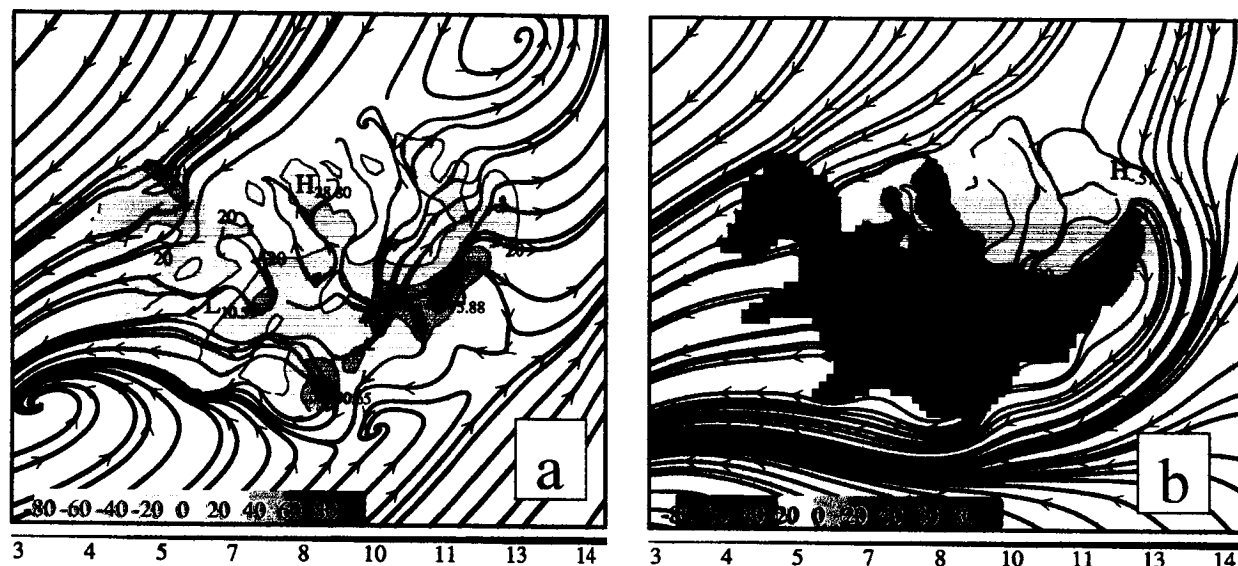
Figure 3.4. The simulated monthly precipitation anomaly and 10m wind for (a) NAO-positive phase, (b) NAO-negative phase 1991-2000. Contour interval is 20 mm and negative values are dashed. Width of streamlines is proportional to wind speed with scale shown at bottom of each figure.

The long-term mean annual precipitation simulated by Polar MM5 for 1991-2000 is shown in Fig. 3.3b. The overall precipitation distribution over Iceland is reasonably well simulated by Polar MM5, especially in the southwest, south and southeast regions. There are shortcomings to many of the simulated smaller scale precipitation features. The model cannot simulate the detailed structure and magnitude of the "observed" precipitation in northwestern and northern Iceland. Rögnvaldsson et al. (2004) applied a statistical model and MM5 to estimate the precipitation in the complex terrain over Iceland. The results suggest that on average MM5 simulates more precipitation than the statistical approach with the contrast being greater in the northern part of Iceland than in the south. To some extent this difference can be explained by gauge measurements not recording all of the solid precipitation during strong wind events, i.e., the observed values in north and northwestern Iceland are probably too small. The computed annual precipitation amounts at Langjökull and Hofsjökull are larger than observed. It seems that the 8 km model resolution is still too coarse to resolve all the observed small-scale variations of precipitation. The winter (September 15-April 30) and summer (May -September 14) precipitation spatial distributions are consistent with the cyclonic forcing changes; the winter amounts are much larger than those during the summer. However, the spatial distribution is maintained in each season, reflecting the dominant control of topography, landuse, model physics and the persistent circulation pattern on the precipitation distribution (Fig 3.3c,d).

Figure 3.4 shows simulated monthly precipitation anomaly and the streamlines of monthly mean near-surface winds for NAO-positive phase and NAO-negative phase simulated by Polar MM5. Rogers (1984) normalized seasonal NAO index (http://polarmet.mps.ohio-state.edu/) is used. The NAO index is taken to be larger than 1 for "NAO-positive phase" and less than -1 for "NAO-negative phase". During NAO-positive phase, the surface wind is stronger than during the negative NAO phase over Iceland. The Icelandic low is stronger in NAO positive phase than during the negative phase and the center of the Icelandic low is located just to the southwest of Iceland. The Greenland high is weaker in the NAO-positive phase and the resulting northerly winds are weaker, and most of Iceland is controlled by southwest winds. The southwesterly near-surface winds flow upslope over most of Iceland and result in the precipitation increase. For NAO-negative phase, Iceland is controlled by northeasterly winds, and precipitation decreases. For both NAO-positive phase and NAO-negative phase in winter, the near-surface wind pattern over Iceland is katabatic.

In general the precipitation over Iceland is positively correlated to the NAO index. In a positive NAO year precipitation over Iceland is larger than average, whereas in negative NAO years the precipitation is reduced.

3.3.2 Trend of annual precipitation over Iceland from 1991 to 2000

Figure 3.5 shows the interannual variations of precipitation simulated by Polar MM5 at T12e and B16d sites over Vatnajökull ice cap, for winter, summer, and annual totals along with observed winter snow accumulation from ice cores for 1991-2000. Snow accumulation is the net result of precipitation, evaporation/sublimation, and drifting. Evaporation/sublimation is likely small in winter, and the net drifting effects are unknown, but should be small, so precipitation is equated with accumulation. The precipitation amounts at the grid points retrieved from simulations are interpolated to the ice core locations.

It is seen that the observed linear decrease of winter accumulation is well captured by the simulated winter precipitation. The precipitation simulated by Polar MM5 is less than observed from 1992 to 1996 in winter, but larger than observed from 1997 to 1999 at site T12e. At site B16d, the simulated precipitation is larger than observed after 1994. T12e is located on the western part of the Vatnajökull ice cap at the northwestern margin of a zone of very large precipitation gradient, and B16d is at south central part of the ice cap where there is also a large precipitation gradient. A slight shift in the model simulation will easily give a different precipitation amount. If the model cannot simulate the mesoscale features, it is difficult to get a good precipitation result at both sites only 40 km apart (or 5 grid lengths), so Polar MM5 has good skill in capturing the terrain-forced precipitation over Iceland. The year-to-year variations in observed winter accumulation are reasonably well represented by the simulated precipitation at B16d and T12e. The winter precipitation decrease determines the annual signal, and there is no significant change in summer. During summer the simulated precipitation is about 500 mm at both sites, and the year-to-year variations are very small.

The spatial distribution of the slope of the linear regression line of annual precipitation from Polar MM5 for 1991-2000 has been computed, and the results are shown in Fig. 3.6. The annual modeled precipitation decreases for all Iceland except the northeastern part, specifically the Askja basin, the northeast coast and the coast close Olafsfjödur where the precipitation increases by about 0-26 mm yr^{-1}. The maximum decreases of modeled precipitation exceed 150 mm yr^{-1} at Hofsjökull, Langjökull, Myrdalsjökull and Vatnajökull ice cap. These simulated results are in

good agreement with those obtained from station precipitation records (Fig. 6b). The model results during winter are similar to the annual results and agree with those obtained from ice core measurements.
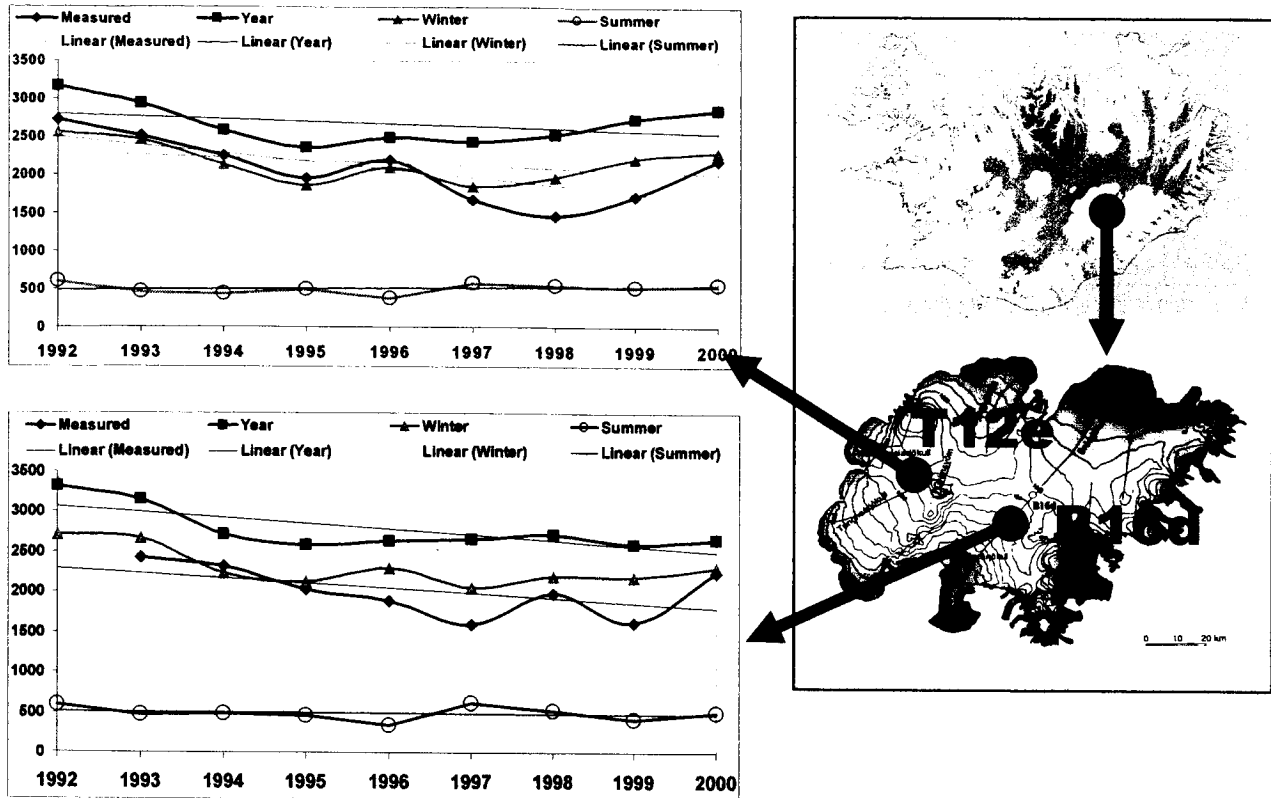
Figure 3.5. The interannual variations of the observed winter (Sep-Apr) accumulation and simulated annual, winter and summer total precipitation (mm) at the sites T12e and B16d over 1992-2000.
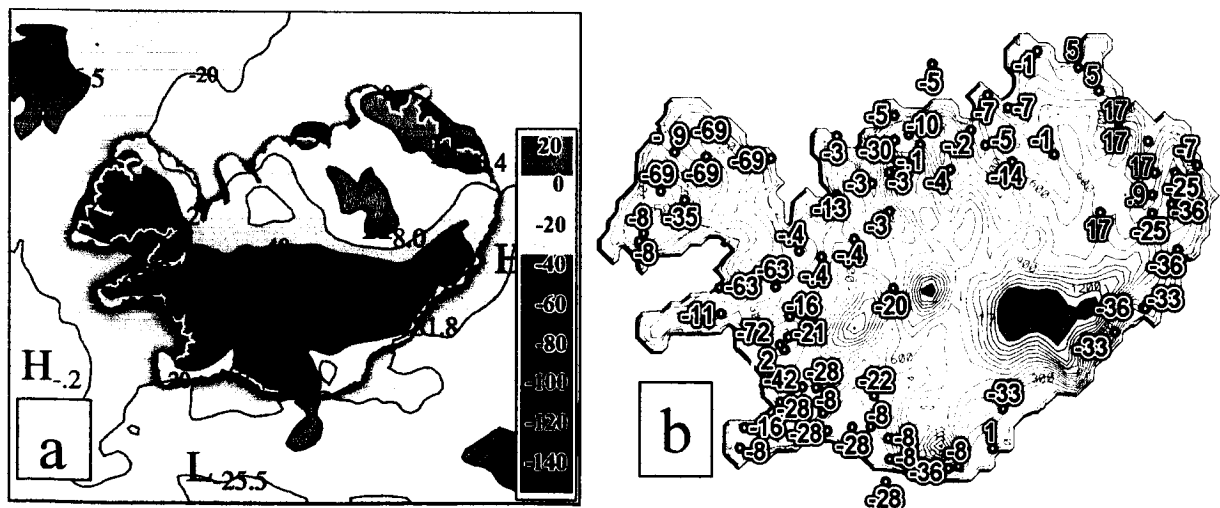
Figure 3.6. (a) Annual precipitation trend in Iceland simulated by Polar MM5 from 1991 to 2000 in mm/year, (b) Annual observed precipitation trend (mm/year) in Iceland for 1991-2000.

From central to southern Iceland, and over the sea to the east and west of Iceland, there is a major negative precipitation trend from 1991 to 2000. The large negative trend area is also

19

found in model domain 2, and from the ERA-40 and ECMWF TOGA precipitation (not shown); this demonstrates that the precipitation decrease is a large scale climate feature that should be investigated.

3.3.3 The relationship between circulation and precipitation

ERA-40 sea level pressure was used to investigate the relationship between large scale circulation and precipitation from 1991 to 2000. Figure 3.7 shows the monthly mean sea level pressure in winter half year (ONDJFM) during 1992-1994 and 1996-1998, and the simulated monthly mean 10m-wind field and precipitation anomaly. It is can be seen that the Icelandic low during 1992-1994 is stronger than during 1996-1998 and the center of the Icelandic low is located to the southwest of Iceland. The Greenland high and associated northerly winds are weaker during 1992-1994 and most of Iceland is controlled by southwesterly winds.
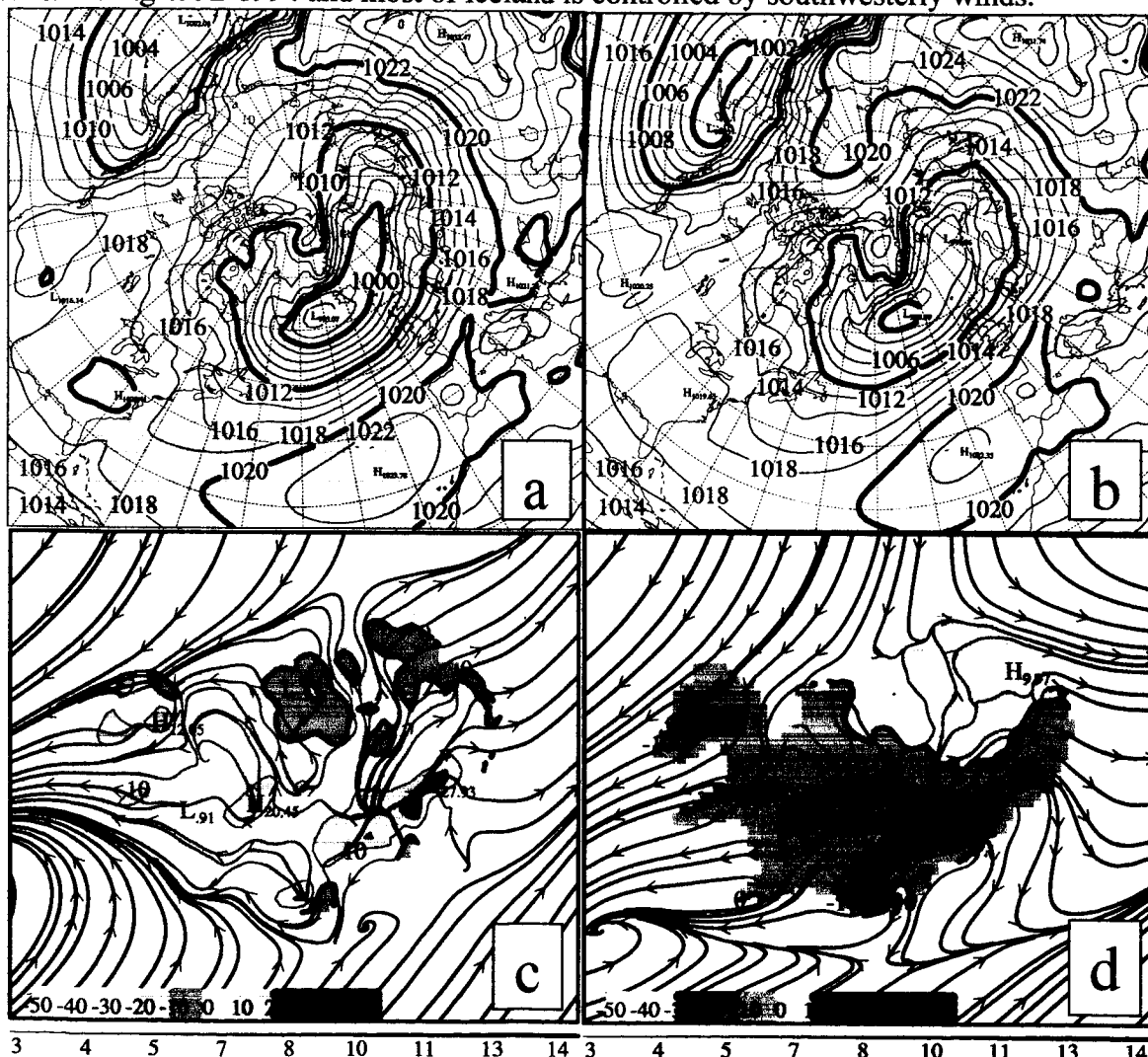
Figure 3.7. The monthly mean sea level pressure in winter half year (ONDJFM) (a) 1992-1994; (b) 1996-1998; contour interval is 2hPa and 1000, 1010 and 1020 isobars are bolded. The simulated monthly mean 10m-wind field and precipitation anomaly in winter half year (ONDJFM) (c) for 1992-1994 and (d) 1996-1998. Width of streamline is proportional to wind speed with the scale shown beneath each streamline plot. Contour interval is 10 mm for precipitation.

20

The southwest near-surface wind flows upslope over the southwest part of Iceland and results in the precipitation increase in this region. During 1996-1998, the Icelandic low was weaker and shifted 4-5° toward the east; the Greenland high became stronger. Iceland was controlled by northeast winds, and precipitation decreased over most of Iceland except for the northeast region where precipitation increased.

It can be summarized that the Icelandic low, Greenland high and their patterns determine the precipitation distribution and change over Iceland. During winter half year from 1991 to 2000, the Icelandic low intensity weakened and its center shifted toward the east (as also found by Rogers at al. 2004) and the Greenland high intensity became stronger. This pattern resulted in stronger north and east winds, and weaker southerly winds; as a consequence precipitation decreased in south and southwest Iceland, and increased in the east.

3.4 Summary

The verification indicates that Polar MM5 accurately simulated the mesoscale and large scale near-surface atmospheric circulations over Iceland on monthly time scales, thus the high-resolution regional climate in a limited area can be reasonably reconstructed using a limited area model with reasonable physical parameterizations, and high-resolution topography and land use.

The simulation results are used to analyze the near-surface wind, temperature, dew point and precipitation climate over Iceland from 1991 to 2000. The time-averaged mesoscale precipitation distribution over Iceland is reasonably simulated by Polar MM5. Consistent with the cyclonic forcing changes, the winter amounts are much larger than those during the summer. The spatial distribution is maintained in each season, reflecting the dominant control of orography. The precipitation is larger than average for the positive NAO phase especially over southeast Iceland, whereas for the negative NAO phase the precipitation is reduced, particularly in western and southern Iceland. The relationship applies throughout the year. By contrast, surface temperature and moisture are lower than normal during the winter half year for the NAO positive phase and higher than normal during the summer half year, a consequence of the seasonally varying atmospheric advection. Examination of ERA-40 fields reveals that these results for 1991-2000 are very similar to those for 1958-2001.

The precipitation decreases strongly over all of Iceland from 1991 to 2000 except for the eastern and northeastern parts where the precipitation slightly increases. During winter half year, the Icelandic low became weaker and its center shifted toward the east, and the Greenland high intensified. This shift reflects a modification of the NAO modulation of regional climate. This altered circulation resulted in stronger north and east winds, and weaker south winds; as a result precipitation decreased in south and southwest Iceland, and increased in the east.

The ten year simulation results indicate that Polar MM5 is a powerful tool for mesoscale regional climate studies in the data sparse high latitudes. The high resolution regional climate simulation can be improved by using three-dimensional variational assimilation in conjunction with Polar MM5 to assimilate observational data over steep topography and by using a land surface model over Iceland. The simulation results can also be improved by increasing the model resolution and model spin-up time.

4. Greenland ice sheet surface mass balance 1991–2000

4.1 Background

Ice sheet mass balance plays an important role in global sea level and thermohaline circulation changes. Greenland ice sheet mass balance changes appear to have contributed several meters to sea level fluctuations since the last climatic optimum, 125,000 years ago [Cuffey and Marshall, 2000], and are expected to contribute to sea level rise under projected future global warming throughout this century [Church et al., 2001]. However, Greenland ice sheet mass balance components are imprecisely known [van der Veen, 2002]. Therefore the importance of the Greenland ice sheet to global ocean dynamics has been associated with large uncertainty. Contributing to this uncertainty, surface mass balance estimates have been produced on the basis of a temporally nonuniform set of observations [e.g., Ohmura et al., 1999]. The interest in Greenland ice sheet mass balance is particularly relevant given the dramatic thinning rates observed in the 1990s at low elevations [Krabill et al., 2000]. The thinning is the combined result of ice flow changes and surface ablation. Apparently critical to this thinning is the interplay between water and ice dynamics, providing a mechanism for accelerated ice sheet response to climate warming [Zwally et al., 2002]. Data and models both suggest that abrupt climate change during the last glaciation originated through changes in the Atlantic thermohaline circulation in response to small changes in the hydrological cycle [Clark et al., 2002]. The other ice sheet, in Antarctica, is 9 times larger in volume, yet only Greenland exhibits substantial seasonal melting, with runoff representing approximately half the ablation total [Janssens and Huybrechts, 2000; Zwally and Giovinetto, 2000] and the remainder of ablation coming from surface water vapor fluxes [Box and Steffen, 2001; De'ry and Yau, 2002] as well as iceberg discharge and subglacial melting [Rignot et al., 1997; Reeh et al., 1999]. Surface water vapor mass fluxes are generally small in comparison with precipitation rates; however, the associated latent heat flux represents an important energy sink, without which surface melt rates would be significantly larger.

Ice sheet studies with regional climate models (RCMs) are increasingly common. Cassano et al. [2001] and Bromwich et al. [2001a] made a validation study of the Polar MM5 RCM over Greenland using automatic weather station (AWS) data. Fettweis et al. [2003] have tested a coupled RCM-snow model using a detailed set of observations from the ETH camp in western Greenland. Using the Mode`le Atmosphe'rique Re'gional (MAR) RCM, they produce a significantly better treatment of the near surface state variables than in the relatively coarse European Centre for Medium-RangeWeather Forecasts (ECMWF) 15-year reanalysis (ERA-15). Galle'e and Duynkerke [1997] employed an early version of MAR to investigate modeling surface energy and mass balance over a transect of observational stations for the Greenland Ice Margin Experiment (GIMEX) 1990–1991, citing limited success in simulating basic meteorological variables and surface melting and runoff. Lefebre et al. [2003] have validated and applied an evolving albedo model applicable by RCMs. Box and Rinke [2003] used the HIRHAM RCM to evaluate multiyear simulations of meteorological and mass balance components over Greenland.

Hanna et al. [2002] and Mote [2003] have made significant progress in incorporating RCM, in situ, and remotely sensed data to estimate Greenland ice sheet surface mass balance and runoff. In the latter study, for a 12-year period (1988–1999), there was some evidence that larger runoff is associated with lower accumulation. To derive surface mass balance and runoff, Mote [2003] employed a methodology depending on the following: a constant threshold in daily average passive microwave brightness temperature to indicate melting; constant degree day factors for ice or snow melt; precipitation distributed evenly throughout the year; constant spatial distribution of 1995–2000 average sublimation/evaporation rate after Box and Steffen [2001]; constant meltwater retention fraction; and liquid precipitation not added to the accumulation rate, but assumed as direct runoff. We pursue a similar methodology, however, with the following differences: calculation of meltwater production based on surface energy balance closure, variable meltwater retention fraction, variable water vapor fluxes from the surface and blowing snow, and liquid precipitation added to melt volume and accumulation.

4.2. Objectives

The first objective of this study is to reassess the accuracy of the Polar MM5 RCM, under a different model configuration, i.e., from that of Bromwich et al. [2001a] and Cassano et al. [2001], using in situ observations collected by a network of automatic weather stations (AWS) and supplemented by other glaciological observations. By analyzing multiple years of RCM output, the variability in surface mass balance components may be gauged. Further, by incorporating interannual surface mass balance results with iceberg discharge and basal melting estimates, we assess total ice sheet mass balance and provide estimates for the contribution of Greenland ice sheet mass balance to sea level.

Sections 4.3.1–4.3.6 describe the atmospheric model, techniques to apply the model data to questions of surface mass balance, the observational data, and methods used for model validation and correction. Maps of the mean surface mass balance components and related meteorological parameters are then presented and discussed in light of previous results and specific regional controls. Integrated total ice sheet surface mass fluxes, equilibrium line variability and sensitivity, and the sensitivity of surface mass balance to temperature and precipitation anomalies are presented in succession. The paper concludes with recommendations about the state of mass balance of the Greenland ice sheet and the challenge of reducing persistent uncertainties.

4.3. Methods

4.3.1. Surface Energy Balance and Meltwater Production

Changes in surface and subsurface temperatures are directly linked to imbalances in the surface energy budget. In the case of a snow/ice surface, when the melting point has been reached during a period of energy surplus, the excess energy goes into conversion of solid ice into liquid water. As such, meltwater production can be calculated from the residual (Q_M) of the surface energy budget:

$$Q_M = Q_N - (Q_H + Q_E + Q_G + Q_R) \tag{4.1}$$

where Q_N is the surface net radiative flux. Problematic for melt simulations, the albedo over the ice sheet in this realization of Polar MM5 was fixed at 0.8. To account for this, daily satellite-

derived albedos [Key et al., 2002] were applied in surface energy balance calculations of absorbed solar irradiance. Although the temperature-albedo feedback is not considered here, sensitivity studies using Polar MM5 indicate that albedo errors do not greatly affect near-surface air or ice temperatures [Cassano et al., 2001]. Year 2000 albedo values were unavailable; thus monthly climatological values compiled from the 1982–1999 data were used. Q_H and Q_E are the turbulent sensible and latent heat fluxes, respectively. Q_G is the firn/ice conductive heat flux, incorporating density-dependent effective thermal conductivity after Sturm et al. [1997]. A depth-density relationship based on Greenland snow pits is taken from Box [2001], and the conductivity estimates are applied off-line to the model output to estimate Q_G. Although we expect potentially large "soil" temperature errors owing to insufficient spin-up time and biases in climatological soil temperature initialization, we have verified that Q_G represents a small component in the modeled surface energy budget and is of tertiary importance to melting as compared to radiation and turbulent fluxes. Q_R is the sensible heat flux from rain. Q_R may be calculated using the rain Tr and surface temperature Ts

$$Q_R = \rho_w c_w R(Tr - Ts) \tag{4.2}$$

where ρ_w is the density of water, c_w is the specific heat of water (4.2 kJ kg^{-1} K^{-1}), and R is the rainfall rate (m s^{-1}). Tr is the rain temperature, and Ts is the surface skin temperature. The contribution of Q_R to the ablation rate is assessed here since parts of the ice sheet, particularly in the south, have a maritime character [Putnins, 1970]. Volumetric melt M in cubic meters or surface height variation (dz dt^{-1}) is related directly to Q_M when surface temperature is at or above the melting point, $Ts > 0\ ^0C$, as

$$M = Q_M t(L\rho)^{-1} \tag{4.3}$$

where t is time (s), ρ is ice density (917 kg m^{-3}), and L is the latent heat of fusion (384 kJ kg^{-1}).

4.3.2. Blowing-Snow Sublimation

It is important to note that sublimation/evaporation derived from bulk atmospheric profile methods, i.e., that based on Q_E, corresponds to surface water vapor flux only and does not include physics for sublimation from blowing and drifting snow Q_S, now recognized as important in the surface mass budget over snow and ice surfaces [Pomeroy and Essery, 1999; Bintanja, 2001; De'ry and Yau, 2002]. In the similar environment over Antarctica, wind-driven sublimation represents one of the major sources of uncertainty in surface mass balance closure [e.g., Turner et al., 2002]. Here, the blowing-snow sublimation component is estimated using a parameterization from De'ry and Yau [2001], equating Q_S with 10-m wind speed, 2-m air temperature, humidity, and pressure. We evaluate the magnitude of the blowing-snow transport horizontal divergence as De'ry and Yau [2002] and Guo et al. [2003] have done for Antarctica, but we explicitly account for snow availability. Potential blowing snow transport in the lowest 10 m (Q_{TP}) is estimated using the bulk formulation of Tabler [1991] based on Antarctic blowing-snow measurements [Budd et al., 1966]

$$Q_{TP} = \frac{u_{10}^{3.93}}{289,951} \tag{4.4}$$

where u_{10} is the 10-m wind speed given by the model and Q_{TP} has units of kg m^{-1} s^{-1} in the direction of the wind. Snow transport is taken to occur when the wind speed exceeds the temperature-dependent threshold [Li and Pomeroy, 1997]. A constant threshold of 7 m s^{-1} was used for temperatures below -27°C owing to unrealistic behavior of the quadratic function in that extreme. Actual snow transport Q_{TA} is estimated using a reduction of Q_{TP} accounting for

24

snow availability A', which is assumed to be unlimited when snow is freshly deposited and decays with time from snow events defined by the model.

$$A'=(1.038+0.03758t-0.00014349t^2 1+1.911315e^{-7}t^3)^{-1} \tag{4.5}$$

Time t is in hours after a snowfall event. After 12 days, A' decays to a value of 0.22 that is then held constant and is proportional to the force required to disaggregate bonds of snow particles of that age measured by Jellinek [1957]. Q_{TA} is estimated by multiplying values of Q_{TP} by A' Blowing snow divergence D is estimated by differencing snow transport at model grid points with the surrounding grid points and represents the combined effect of blowing-snow sublimation and snow redistribution; thus it cannot be used to distinguish blowing-snow sublimation alone.

4.3.3. Meltwater Retention and Runoff

To gauge runoff, we use the Pfeffer et al. [1991] model for meltwater retention, which includes both capillary tension and latent heating effects for a simple uniform wetting front. This method considers meltwater retention for single annual (snow accumulation season) layers only and thus does not consider the case of meltwater percolating into the previous accumulation layer. Consequently, in extremely warm years, runoff may be overestimated, as annual melt exceeding the accumulation rate is not retained. Janssens and Huybrechts [2000] evaluated this and simpler models for meltwater retention using climatological average accumulation and melt. Annual potential meltwater retention fraction pr, estimated using the annual mean temperature T, snow melt volume M, precipitation P, surface sublimation/evaporation E, blowing-snow sublimation Q_S, specific dry snow accumulation C calculated as P-E-Q_S-liquid precipitation, and the depth of melting d, here is taken as the water equivalent depth of the annual accumulation rate

$$p_r = [\frac{c}{L_f}T\frac{d}{P}+(\frac{C-M}{P})(\frac{\rho_e}{\rho_0}-1)] \tag{4.6}$$

where c is the specific heat of ice (2009 J kg^{-1} K^{-1}), ρ_e is the density of water-saturated snow ($\sim$960 kg m^{-3}), and ρ_o is the average density of dry firn from 0- to 2-m snow depth (353 kg m^{-3}) based on west Greenland snow pits [Box, 2001]. In equation (4.6), M represents the melt of seasonal snow only, i.e., not including glacier ice below the annual accumulation that is found in the net ablation zone. Hence, if melt derived from energy balance closure exceeds the accumulation rate for that year, M is set equal to the accumulation rate in equation (4.6), allowing the value of pr to always be positive, and as long as melt calculated by energy balance closure does not exceed the accumulation rate, there is some meltwater retention by percolation and refreeze, i.e., internal accumulation. In cases when M exceeds C, the excess is allowed to run off.

4.3.4. Interannual Variability

The ability to gauge the absolute and annual variability in ice sheet mass balance components is an attractive capability of regional climate models. Identifying the spatial pattern of year-to-year variability allows identification of regions where largest changes may be taking place. We gauge interannual variability using the 10-year range R of annual values. A 10-year sample is insufficient to define a more robust variability statistic such as the standard deviation. The reader is reminded that R increases with the sample size and therefore increasingly exceeds

σ with sample size. Variability as defined by R will be more indicative of the absolute variability, not the "standard" variability, i.e., as indicated by 1xσ, which represents only 2/3 of the sample variance. Finally, it is important to note that by analyzing the spatial patterns of year-to-year variability, absolute systematic bias effects are minimized.

4.3.5. In Situ Model Validation Data

a Automatic Weather Station Data

In situ observations from Greenland Climate Network (GC-Net) automatic weather stations (AWS) [Steffen and Box, 2001] data from 15 sites (ID numbers 01–15) were compared with 6-hourly Polar MM5 output over a period of relative data abundance (1998–2000). Figure 4.1 includes the GC-Net AWS distribution and the JAR2 and JAR3 sites 17 and 19. The latter two sites were used only for melt and surface mass balance validation, as they are too close to the ice margin for interpolation using surrounding grid cells. Given that Polar MM5 output represents instantaneous conditions, the comparisons are made with the highest available temporal resolution, i.e., hourly averages. Modeled precipitation is cumulative and therefore does not suffer from lower skill due to the inconsistent sampling between measured and modeled data. We evaluate the model ability to capture both hourly and interannual variability. Root-mean-square (RMS) error was calculated from annual distributions of up to 1464 six-hourly samples.
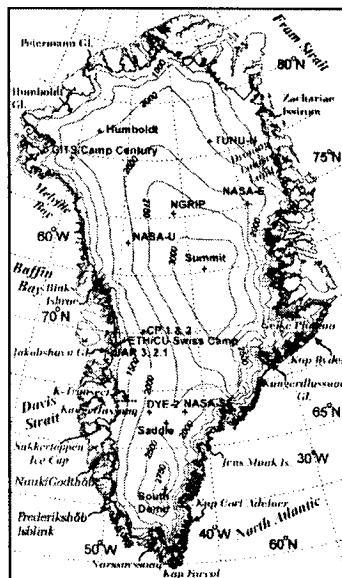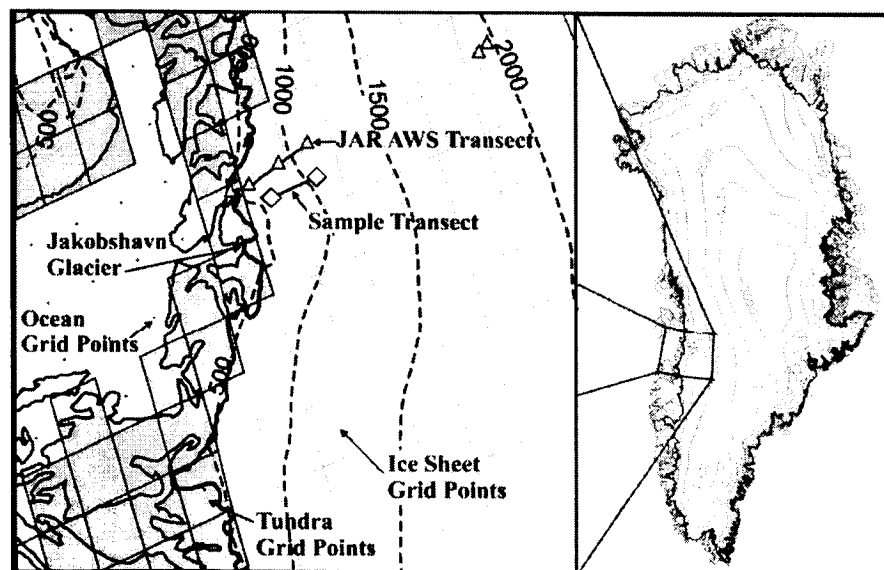
Fig 4.1   Fig4.2

Figure 4.1. Greenland map featuring inland ice region. Greenland Climate Network (GC-Net) automatic weather station sites are indicated by plus symbols. Locations referred to in the text are included.

Figure 4.2. Illustration of model domain over the Jakobshavn Ablation Region (JAR) featuring elevation contour lines and the sample elevation transect used for comparison of model results with AWS locations near the ice sheet margin. Model grid cells with land surface properties corresponding to permanent ice, tundra, and ocean are indicated. Greenland elevation contours are in units of meters above sea level.

Comparisons between gridded 24-km model data and point measurements at the majority of AWS locations are facilitated using bilinear interpolation from the four surrounding model

grid values. For AWS sites within 24 km of the ice margin this type of interpolation becomes invalid, given sharply contrasting values resulting from different land surface types in the model, i.e., between ice and tundra or ocean. Also near the ice margin, the spatial gradients are too large to make meaningful comparisons using the closest valid model grid point. To overcome these problems, we have used the nearest similar "sample elevation transect" in the model domain to make comparisons between modeled and observed surface mass balance given a strong elevation dependence. In the Jakobshavn Ablation Region (JAR), three AWS exist below equilibrium line altitude for comparison with Polar MM5 results. The chosen sample transect is nearly parallel and lies 5 km to the south of the AWS transect (Figure 4.2). Only two grid points were used, i.e., instead of 3 or 4, because the gradient is locally very large and the next model grid point to the west is not over ice.

b. Surface Mass Balance and Accumulation

Ten years of surface mass balance measurements along an elevation transect at 67°N in western Greenland, i.e., the K-transect [Greuell et al., 2001], are useful to evaluate simulated surface mass balance model bias. GC-Net AWS data provide surface mass balance estimates from acoustic height measurements and from snow pit observations made during AWS visits. A small adjustment has been applied to surface height data to account for firn compaction based on compaction measurements from central Greenland [Hamilton and Whillans, 2000]. Thus, with surface mass balance data from two independent locations, we may assess, correct, and cross-check modeled values. Ultimately, we compare our surface mass balance results with a parameterization for equilibrium line altitude for the Greenland ice sheet available on the basis of least squares regression of historical glaciological survey data [Zwally and Giovinetto, 2001].

c. Ten-Meter Wind Speed

Over seasonal timescales, GC-Net AWS instruments vary in height above the surface by as much as 3 m owing to accumulation and ablation. Wind speed instruments are placed at two levels on each AWS, separated by 1.2 m. Temperature and wind speed profile data in addition to surface height and pressure measurements are used as inputs into models for the atmospheric surface boundary layer necessary to estimate 10-m wind speeds for comparison with Polar MM5 10-m wind speed. A major uncertainty in the comparison of observed and modeled wind speeds is the effect of buoyant stability on the temperature and wind speed profiles. We rely on boundary layer theory to adjust the observed wind speed profile to estimate 10-m wind speeds from in situ AWS observations, as has been done for AWS data over the Eidgenossische Technische Hochschule/University of Colorado (ETH/CU) Swiss Camp [Lefebre et al., 2003]. A large uncertainty exists in both in situ derived and modeled 10-m wind speed owing to poorly defined stability corrections in the extremely stable surface boundary layer and coarse model resolution near the surface, respectively. However, as the wind speed increases, turbulent mixing minimizes buoyant stability effects, and estimates of 10-m wind speed using in situ profile measurements are likely to be reliable.

d. Two-Meter Air and Surface Temperature and Upward Longwave Radiation

Temperature at a constant height of 2 m is calculated using the observed temperature at two levels, instrument heights, and linear interpolation. Instrument heights are calculated using the initial instrument height upon installation and subsequent surface height change measured by acoustic height sensors. Instrument height error has been found during site revisits to be within

10 cm. The median heights of GC-Net temperature sensors were 1.4 and 2.6 m, respectively. Surface temperature is estimated using a linear extrapolation of the observed air temperature profile. Only cases when wind speed >4 m s^{-1} are considered to avoid the largest stability and solar overheating errors. Upward longwave radiation has been calculated using the surface temperature estimate and a constant thermal emissivity value of 0.98 and does not include multiple reflection terms.

e. Shortwave Radiation Data

The GC-Net sites employ a LI-COR 200SZ photoelectric diode to measure incoming and reflected solar radiation in the 400-1100-nm wavelength range. The peak response of this pyranometer occurs at 950 nm. LI-COR reflected shortwave radiation measurements over snow exhibit a positive bias of ~4% that has been corrected on the basis of clear-sky calibrations with Eppley Precision Spectral and Kipp Pyranometer observations. Hourly RMS errors are less than 10%, on the basis of comparisons at Swiss Camp and Summit.

f. Turbulent Heat Fluxes

Turbulent heat fluxes of sensible Q_H and latent heat Q_E are important components of the surface energy budget over melting snow surfaces [e.g., Henneken et al., 1997]. Q_H and Q_E from Polar MM5 output are available for comparison with that derived from aerodynamic profile calculations applied to the GC-Net AWS data. In situ Q_H calculations follow the procedure given by Steffen and DeMaria [1996]. Q_E derived from AWS data is based on Box and Steffen [2001] and shows good agreement with eddy correlation and snow lysimeters.

4.4. Results and Discussion

4.4.1. Model Comparison With In Situ Observations

a. Comparison With AWS Data

Model performance over Greenland for basic meteorological variables (pressure, temperature, humidity, wind speed and direction, solar and net radiation) has been assessed using in situ observations independent of the atmospheric analyses in two studies [Bromwich et al., 2001a; Cassano et al., 2001]. The results indicate a high degree of skill in modeled representation of the surface climate over Greenland. Antarctic validation results have been published [Guo et al., 2003] and reveal larger biases owing to weaker constraints from the observational analyses.

In this study, a longer series of surface data and more parameters are compared than in previous Polar MM5 validations. Consistent results were observed from year to year over the 3-year comparison (1998–2000) for all parameters, indicating that potential data homogeneity errors caused by an evolving ECMWF operational analysis product are not of primary importance. Therefore the tabulated results are based on averages over all 15 AWS sites for all 3 years, supplemented with minimum and maximum site-specific annual results to illustrate intersite variability (Table 4.1). The albedo results in Table 1 are between the AWS observations and the 25-km Extended Advanced Very High Resolution Radiometer (AVHRR) Polar Pathfinder (APP-x) product [Key et al., 2002] for a 2-year comparison, i.e., 1998 and 1999. Model validation statistics listed in this table are for both AWS observed and derived quantities.

Derived quantities include turbulent heat fluxes, surface temperature, and outward longwave radiation discussed above.

Table 4.1. Annual Summary 6-Hourly Comparison of Polar MM5 Surface Climate Parameters With AWS Data 1998–2000.

Parameter	Polar MM5	Mean Bias	Min., Max. Bias[a]	RMSE	Min., Max. RMSE	Mean Correlation r	Min., Max. Correlation r	Number of AWS-Years
2-m air temperature, K	252.3	1.0	-0.01, 2.49	3.6	2.36, 5.36	0.96	0.902, 0.982	41.1
Ground temperature, K	248.3	-2.9	-5.17, -0.87	5.5	3.33, 7.88	0.94	0.839, 0.970	42.2
10-m wind speed, m s^{-1}	8.5	2.6	0.61, 4.57	4.4	3.35, 6.12	0.48	0.232, 0.678	25.6
Sensible heat flux, W m^{-2}	-31.2	-14.1	-36.82, 12.74	32.8	21.64, 46.27	0.37	0.071, 0.654	33.5
Latent heat flux, W m^{-2}	0.3	-16.0	-67.98, -1.85	26.9	8.68, 84.01	0.36	0.011, 0.578	36.6
Outward longwave flux, W m^{-2}	186.2	-40.9	-66.88, -24.53	47.3	33.56, 71.72	0.87	0.724, 0.946	42.2
Downward shortwave flux, W m^{-2}	275.3	8.2	-20.85, 60.93	93.3	53.95, 287.64	0.91	0.377, 0.972	21.0
Albedo, dimensionless	0.85	0.03	-0.03, 0.11	0.10	0.05, 0.19	0.19	-0.093, 0.563	11.0
Specific humidity, g kg^{-1}	1.4	0.0	-0.25, 0.37	0.4	0.28, 0.73	0.92	0.704, 0.960	32.4
Surface pressure, hPa	738.9	2.3	-1.75, 6.71	3.8	1.28, 6.95	0.98	0.899, 0.996	21.1

[a]Min., minimum; Max., maximum.

Through the comparison of up to 42 station years of AWS observations, it became obvious that seemingly small systematic model biases have important consequences for surface energy balance errors. A 2-m air temperature warm bias combined with a cold bias in surface temperature indicates an overly strong surface temperature inversion (STI) in the model. The 2-m air temperature had little or no evolving bias with time into the simulation. However, the surface temperature cold bias increased into the simulation and caused a 40-W m^{-2} (20%) negative bias in upward longwave irradiance (LWU). Not accounting for a 2% reflection of downward longwave irradiance (LWD) in our LWU estimate can account for an LWU error of up to -6 W m^{-2}, which on average would represent an error of less than 10%. The model surface thermal emissivity employs a constant value equal to 0.95. Assuming 0.98 is a correct value [e.g., Warren, 1982], ~20% of this negative bias can be explained. We have compared, observed, and modeled LWU and LWD at Summit, on the basis of ventilated Kipp CG4 pyrgeometer data. The results suggested a large underestimate of LWD (-38 W m^{-2}) and have confirmed the underestimated LWU. A negative LWD bias for clear-sky conditions has also been identified in the CCM2 radiation code [Pinto et al., 1999]. Although the LWU bias contributes to the evolving surface temperature cold bias, we note a cancellation of longwave errors in terms of the net radiation. A 5-W m^{-2} to 10-W m^{-2} (2–5%) positive bias in downward solar irradiance, for Sun angles >10°, contributes to a positive net radiation bias. Modeled 10-m wind speeds exhibit a 2.7 m s^{-1} (32%) positive bias on average, likely due to the overestimated STI, as the wind speed bias also increased on average into each simulation. A 12~15-Wm^{-2} (40–50%) average overestimation of the atmosphere to surface sensible heat flux was caused by the overly strong STI, exacerbated by a feedback from overestimated wind speeds. The STI bias leads to a suppression of surface water vapor losses (sublimation), as indicated by a negative bias in surface latent heat flux. Uncorrected, the net surface water vapor mass flux would include a deposition bias. The warm bias in modeled near surfaced air temperatures is symptomatic of the persistent inability of atmospheric models to accurately resolve the extreme STI over ice sheets [e.g., van Lipzig et al., 1999; Box and Rinke, 2003], implying that either the near-surface vertical resolution and/or stable boundary layer parameterizations are inadequate. A small (~4%) humidity bias was evident from this comparison. Model wind direction errors were consistently within 15° of the observations. Surface pressure variations were extremely well reproduced by the model. AWS sites with accurate elevation measurements, from differential GPS [see Cassano et al., 2001], were used to construct the results for pressure in Table 1, which suggest a 2-hPa positive bias. The negative downward longwave bias persists at 30 hours into the

simulation, indicating that this bias is not due to insufficient spin-up time, but suggests insufficient cloud radiative effects. APP-x satellite-derived albedo in comparison with daily AWS observations reveals a small positive bias and RMS error of 0.1.RMS errors reported in Table 1 are based on an annual distribution of 6-hourly samples and are representative of generally larger hourly (not monthly or annual) model error.

Wind speed and humidity biases evident from this comparison are broadly consistent with earlier Polar MM5 comparisons with GC-Net AWS data [Bromwich et al., 2001a; Cassano et al., 2001]. Notable disparities include that Cassano et al. [2001] found a cold bias in 2-m air temperature, a negative downward shortwave bias, and a -2-hPa pressure bias. Results in contrast to the previous studies are attributable to less spin-up time in the present configuration and differences in planetary boundary layer model, model resolution, domain size, and domain location. The influence of the latter three differences is not investigated here.

Model skill in representing temporal variability was measured by the Pearson's correlation coefficient r. High model-explained variance r^2 is noted: 96% for surface pressure, 92% for 2-m air temperature, 88% for surface temperature, 85% for humidity, and 83% for downward solar radiation. Less explained variance was evident for wind speed and turbulent heat fluxes. These variables represent an extreme challenge for comparison with mesoscale models owing to highly localized effects in space and time in the observational data. Multiplication of observational errors in turbulent flux calculations further degrades the apparent model skill. Also noteworthy is that parameters that fluctuate around zero or have little trend (e.g., latent heat flux and albedo) typically yield low r values.

b. Sublimation

Polar MM5 surface water vapor flux values exhibit a systematic negative bias as compared to that derived by bulk (one-level) and profile (two-level) methods [Box and Steffen, 2001] applied to AWS data (Figure 4.3).
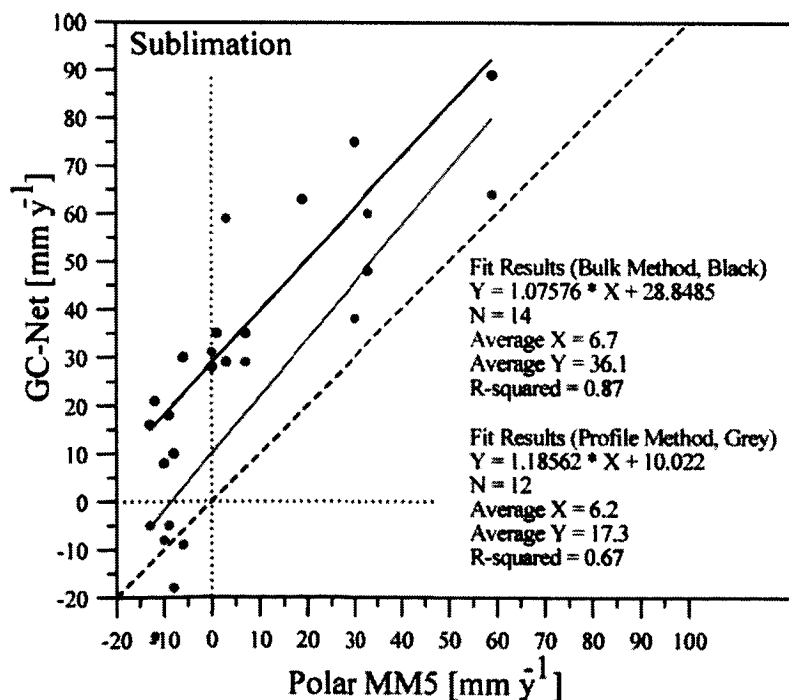

Figure 4.3. Comparison of annual average model sublimation (1996–1999) with values from 14 GC-Net AWS sites.

There are a different number of data points from one method to the next owing to differing data requirements and availability. There is an offset in Polar MM5 values for the bulk method. When Polar MM5 values are compared with the two-level profile method, there is again a negative bias for positive values (sublimation) but general agreement for negative values (deposition), implying an accurate representation of the water vapor deposition process by the countergradient method of Troen and Mahrt [1986]. We conclude that a negative (deposition) bias exists in Polar MM5 simulations, owing to an overly strong surface temperature inversion. We correct this bias in Polar MM5 data on the basis of the "profile" method regression results in Figure 4.3, since they better represent deposition. This correction produced an average ice sheet total surface water vapor flux in agreement with the climatology of Box and Steffen [2001], that of 12% precipitation loss. Without the correction the loss is implied to be 6%.

c. Blowing-Snow Sublimation

We have applied the parameterization from De'ry and Yau [2001] to the AWS data and Polar MM5 output. Our comparisons suggest that the positive biases in modeled air temperature and wind speed contribute to a 60% overestimation of blowing-snow sublimation. Linear regression results of the AWS- and Polar-MM5-derived blowing-snow sublimation (using the same parameterization) have sufficient explained variance ($r^2 = 0.71$) to justify correction of the Polar-MM5-derived blowing-snow sublimation by the inverse of the regression, rather than proceeding with a known bias in blowing-snow sublimation not due to errors in the parameterization.

d. Precipitation and Accumulation

Polar MM5 simulation of accumulation rate as measured by precipitation minus net surface water vapor flux minus blowing-snow sublimation is compared to accumulation rate derived from snow pit and AWS acoustic height data (Figure 4.4).
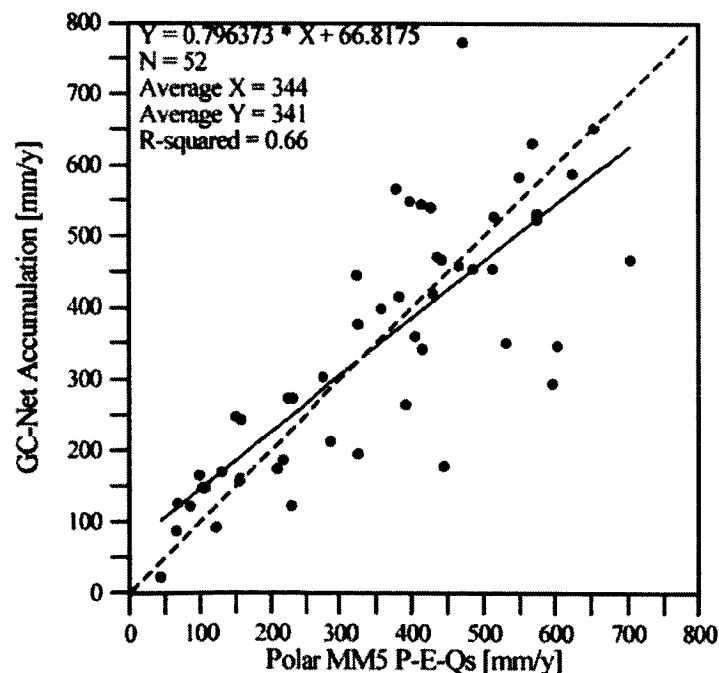

Figure 4.4. Comparison of annual accumulation rates at AWS sites above equilibrium line altitude (1998–2000) with Polar MM5 results.

The remaining positive bias is suggestive of a residual positive bias in precipitation rate, as we have corrected the bias in net surface water vapor flux and blowing-snow sublimation. In this comparison, however, the distribution of values is not statistically different, as measured by the analysis of variance (ANOVA) statistic. The heteroscedasticity in the scatter may be attributed to many things, including a scale problem when comparing point measurements with 24-km grid cells and the accumulation of both observational and model errors in this multicomponent derivative.

e. Ablation Zone Surface Mass Balance

Surface height measurements from three AWS in the Jakobshavn Ablation Region (JAR) (Figure 3) were used to assess the accuracy of surface mass balance calculations from Polar MM5. We reconstructed in situ accumulation rates from ablation zone AWS surface height measurements by noting the snow height value at the onset of melt relative to the height of the glacier ice at the end of the previous melt season. Snow water equivalent accumulation has been derived on the basis of snow pit density measurements at these sites. The total water equivalent surface mass balance value was derived given a density assumption for glacier ice with some small air content (i.e., 900 kg m^{-3}). In situ data overlaps with Polar MM5 output are limited to 1996–2000 for JAR1, 1999–2000 for JAR2, and 2000 for JAR3. JAR3 surface mass balance for the year 2000 was estimated using the year 2001 snow accumulation value (0.1-m water equivalence). The average annual surface mass balance estimates from the AWS were -1.4 m, -2.3 m, and -2.8 m, respectively. The Polar MM5 values modeled with the sample transect corresponded to -2.7 m, -3.4 m, and -4.1 m, respectively. Thus the Polar MM5 bias along the JAR transect was -1.3 m, -1.1 m, and -1.3 m, respectively. We attribute this bias to the combined effect of the following: overestimated net radiation and sensible heat flux and the negative bias in latent heat flux caused primarily by too strong surface temperature inversion in this model configuration. For the lowest sites, JAR2 and JAR3, AWS measurements do not indicate the contribution of rain to the surface mass balance, which would somewhat reduce this bias. For the purposes of this comparison we do not try to correct for rain. Rather, we compare Polar MM5 surface mass balance results with the glacier survey results near the K-transect [Greuell et al., 2001] some 280 km to the south. With the K-transect results, we evaluate the Polar MM5 surface mass balance biases for the 1991–2000 average and experimentally adjust the Polar MM5 melt energy magnitude via a simple multiplier of 0.55 to produce a match with the average K-transect equilibrium line altitude over the identical decadal average. The resulting elevation profile of corrected surface mass balance closely resembles the K-transect results, both at equilibrium line altitude (ELA) near 1500 m and the values at the extreme high (1850 m) and low (400-m) elevation limits.We then cross-checked this "global" correction again using the JAR transect surface mass balance observational data. After the K-transect correction the resulting biases correspond to -0.07 m for JAR1, 0.15 m for JAR2, and 0.22 m for JAR3, or within 10% of the surface mass balance magnitude. We proceed using this simple correction to solve the annual surface mass balance for the entire ice sheet.

4.4.2. Spatial Distribution of Surface Mass Balance Components

a. Precipitation

Modeled annual precipitation distributions include widely recognized mesoscale features including maxima found along the southeastern slope, near 72°N along the western slope, and

above Melville Bay [e.g., Ohmura and Reeh, 1991; Ohmura et al., 1999] (Figure 4.5a). Regional patterns are also consistent with more recent modeling studies [e.g., Chen et al., 1997; Bromwich et al., 2001b; Cassano et al., 2001; Hanna et al., 2002; Box and Rinke, 2003]. Maximum values (>2500 mm yr^{-1}) are simulated over ocean grid cells adjacent to maxima over the ice sheet. Indeed, enhancement of precipitation values is simulated over the seas surrounding much of the ice sheet, indicative of topographic blocking. Greatest differences over the ice sheet among the different estimates are found near the precipitation minimum in the northeast and along the southeast coastal zone. For example, Cassano et al. [2001] obtained maximum values exceeding 4000 mm yr^{-1}, probably too large because of imprecision in the calculation of the horizontal pressure gradient force over steep slopes. The maxima found at intermediate elevations around the ice sheet are caused by precipitation enhancement by topographic lifting, i.e., orographic precipitation. Notably, a relative maximum is observed over and to the southeast of the Sukkertoppen Ice Cap, and to the north, there is a precipitation shadow. The model reproduces the regional minimum in precipitation surrounding the airport at Kangerlussuaq, formerly Sondrestrøm Air Force Base and otherwise known as "Greenland's Riviera." In northern Greenland, regional maxima in precipitation are indicative of northerly tracking storms, with greater precipitation rates also concentrated on up-slope paths. Precipitation shadows appear along lee slopes of topographic features, for example, along the western slope of the southern tip of the ice sheet or in the lee of the topographic divide north of Camp Century toward the Humboldt Glacier. Large variability in regional topography of the ice sheet northeast of the Rinks Isbrae is observed in western Greenland at 72°N to coincide with a regional maximum in precipitation. This feature also seems to be linked to the persistent mesoscale low-pressure trough along the west coast.

Table 4.2. Ten-Year Average Magnitude and Location of Extremes in Surface-Mass-Balance-Related Parameters Based on Polar MM5 Simulations 1991–2000[a].

Parameter	Value	Latitude, °N	Longitude, °W	Elevation, m
Total precipitation (min.)	63	76.95	39.66	2626
Total precipitation (max.)	2385	64.79	40.67	390
Solid precipitation (min.)	63	76.95	39.66	2626
Solid precipitation (max.)	2224	64.79	40.67	390
Liquid precipitation (min.)	0	–	–	–
Liquid precipitation (max.)	676	61.05	46.12	632
Liquid precipitation fraction (min.), %	0	–	–	–
Liquid precipitation fraction (max.), %	73	61.28	47.67	821
Wind speed (min.), m s^{-1}	3.5	80.47	59.78	98
Wind speed (max.), m s^{-1}	14.9	76.62	24.57	1144
Surface water vapor flux (min.)	−15	68.17	49.89	533
Surface water vapor flux (max.)	674	61.01	44.71	550
Blowing-snow sublimation (min.)	1	70.71	50.52	321
Blowing-snow sublimation (max.)	400	69.35	24.59	552
Snow transport (min.), kg m^{-1} yr^{-1}	3470	66.97	49.99	369
Snow transport (max.), kg m^{-1} yr^{-1}	5,001,564	61.33	43.95	2047
Divergence (min.)	−249	69.16	25.91	1531
Divergence (max.)	345	61.22	44.82	741
Accumulation (min.)	−422	72.51	53.59	637
Accumulation (max.)	1826	64.79	40.67	390
Meltwater production (min.)	0	–	–	–
Meltwater production (max.)	6079	61.79	41.82	413
Runoff (min.)	0	–	–	–
Runoff (max.)	6315	61.79	41.82	413
Surface mass balance (min.)	−6393	61.79	41.82	413
Surface mass balance (max.)	1849	66.06	38.49	1479
2-m air temperature (min.), °C	−30	74.78	35.64	2852
2-m air temperature (max.), °C	−1	65.63	38.33	804
Melt days (min.), days	0	–	–	–
Melt days (max.), days	109	61.28	47.67	821

[a]Surface-mass-balance-related parameters are given in mm yr^{-1}, or are otherwise noted.

Extremes values in surface-mass-balance-related parameters over the ice sheet and their geographic coordinates are listed in Table 4.2. The absolute magnitude of the values and precise locations may still contain biases. Nevertheless, the location (including elevation) of these extremes is of critical interest in glacier climatology and should be more precisely located than is possible even with more dense observational networks.
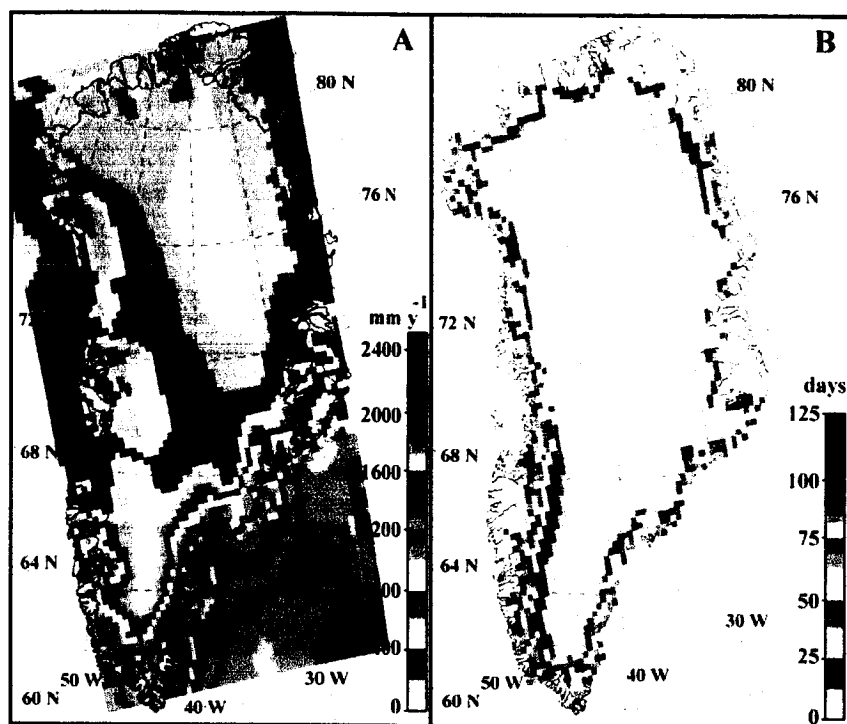

Figure 4.5. (a) The 1991–2000 average annual total (solid + liquid) precipitation. Non-ice-sheet areas are included for discussion. (b) Annual liquid precipitation days.

It is noteworthy that certain parameters, e.g., precipitation, exhibit more than one regional maximum. However, we list only the singular absolute maxima. A maximum in total precipitation and solid precipitation is simulated to occur up glacier from Jens Munk Island in southeast Greenland (Table 4.2). Minimum precipitation rates of 62 mm yr^{-1} may be underestimated, as compared to results from ice cores, which imply values exceeding 100 mm yr^{-1}, i.e., at Tunu-N [Mosley-Thompson et al., 2001].

According to our simulation, rain constitutes as much as 70% of the annual precipitation rate in coastal regions of southwestern ice sheet (Figure 4.5b). This fraction can be large in areas where precipitation rates are low, such as near Kangerlussuaq. Values of 10–15% are typical for the southern coastal zone. The contribution of QR to the ablation rate is very small for the melting part of the ice sheet as a whole, less than 1% of the total melt energy. We assumed a mixture of liquid and solid precipitation that varied with temperature from 100% liquid precipitation for 2-m air temperatures >4°C to 0% liquid at 0°C. A maximum liquid precipitation value of 676 mm yr^{-1} is simulated over the southern tip of the ice sheet (Table 4.2).

b. Surface Water Vapor Flux

The annual sublimation/evaporation maps exhibit the spatial structure that emerges based on spatially interpolated AWS-derived values [Box and Steffen, 2001], i.e., an overall water vapor loss for the ice sheet with decreasing loss with increasing elevation, switching to

gain on the higher parts of the ice sheet (Figure 4.6a). This result is consistent with the HIRHAM (using European Center/Hamburg 4 (ECHAM-4) physical parameterizations) model results over Greenland [Box and Rinke, 2003]. The 10-year average modeled sublimation/evaporation map includes the region of slight net water vapor deposition of up to +15 mm yr^{-1} centered in the northeast, consistent with AWS-derived sublimation. In the relatively warm year of 1998 the deposition zone was nonexistent, consistent with the correlation of temperature and bulk method surface water vapor flux. A maximum water vapor loss in the northeast near 77°N may be associated with the relatively large wind speeds simulated to occur there. Maximum water vapor mass losses are simulated over the broad ablation zone south of the Jakobshavn glacier (Table 4.2), where katabatic winds remain strong and humidity is relatively low. Extreme maximum values of surface water vapor loss at southern ice margin grid cells, i.e., >500 mm yr^{-1}, are dominated by evaporation during the six-month melt season in which sublimation is shut off. Not far away, an area of net annual water vapor deposition is simulated along the western slope near the southern tip of the ice sheet near Narssarssuaq (Table 4.2). Therefore a complex local-scale pattern is evident in the model for this part of Greenland characterized by large orographic variability. Some limited areas of net deposition are also found near the coast in western Greenland, implying a dominance of deposition/condensation in a few special locations, also associated with a complex orographic setting.

c. Blowing-Snow Sublimation

Blowing-snow sublimation rates, according to the parameterization of De'ry and Yau [2001], have maximum annual values of 160 mm yr^{-1} and often did not exceed the net surface water vapor flux (Figure 4.6b).
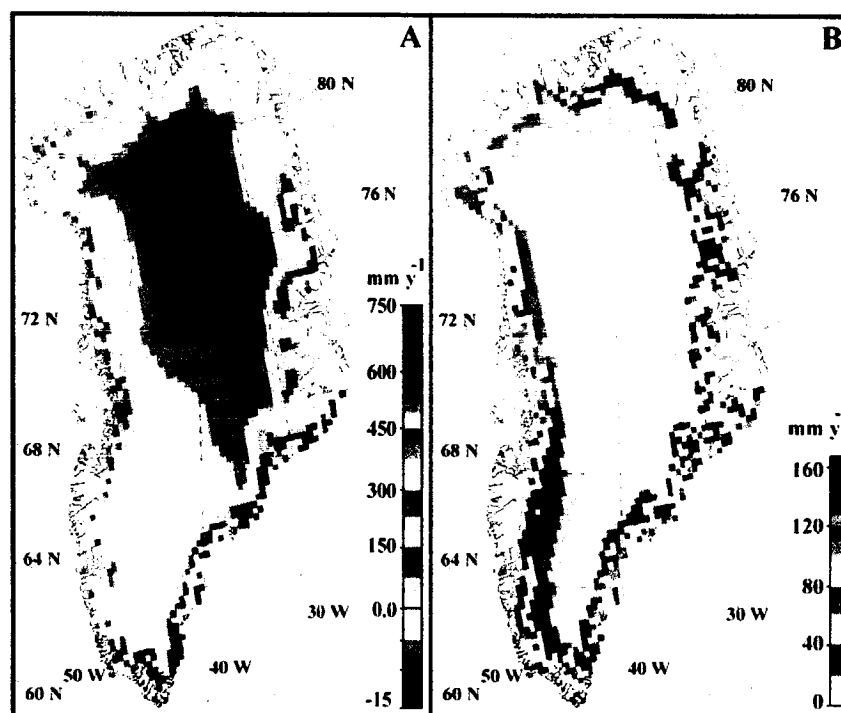

Figure 4.6. (a) The 1991–2000 average annual net surface water vapor flux. (b) Average annual blowingsnow sublimation rate based on the parameterization of De'ry and Yau [2001].

35

This result is consistent with that of De'ry and Yau [2002], in which summer surface water vapor flux dominates the annual net water vapor mass balance. Simulated blowing-snow sublimation maxima are found in the southeast, where apparently temperature effects dominate, despite relatively high humidity. Relatively large water vapor mass losses are found in the northeast and west, where the air is less humid and winds are relatively strong.

d. Katabatic Winds

The ice sheet has a gently sloping surface over large scales with slope angles generally increasing toward the coast. In the presence of a surface temperature inversion, katabatic winds develop along this sloping surface. The katabatic wind predominates on the annual mean basis owing to the net negative surface radiation balance and dominates the near-surface climate of the ice sheet as evidenced by strong annual wind speeds (4 ~ 9 m s^{-1}) and winter wind speed maxima consistent with net radiation variations [Steffen and Box, 2001]. Over the ice sheet, near-surface (10-m) wind streamlines are indicative of this close correspondence between wind direction and topography modified by the Coriolis effect (Figure 4.7a).
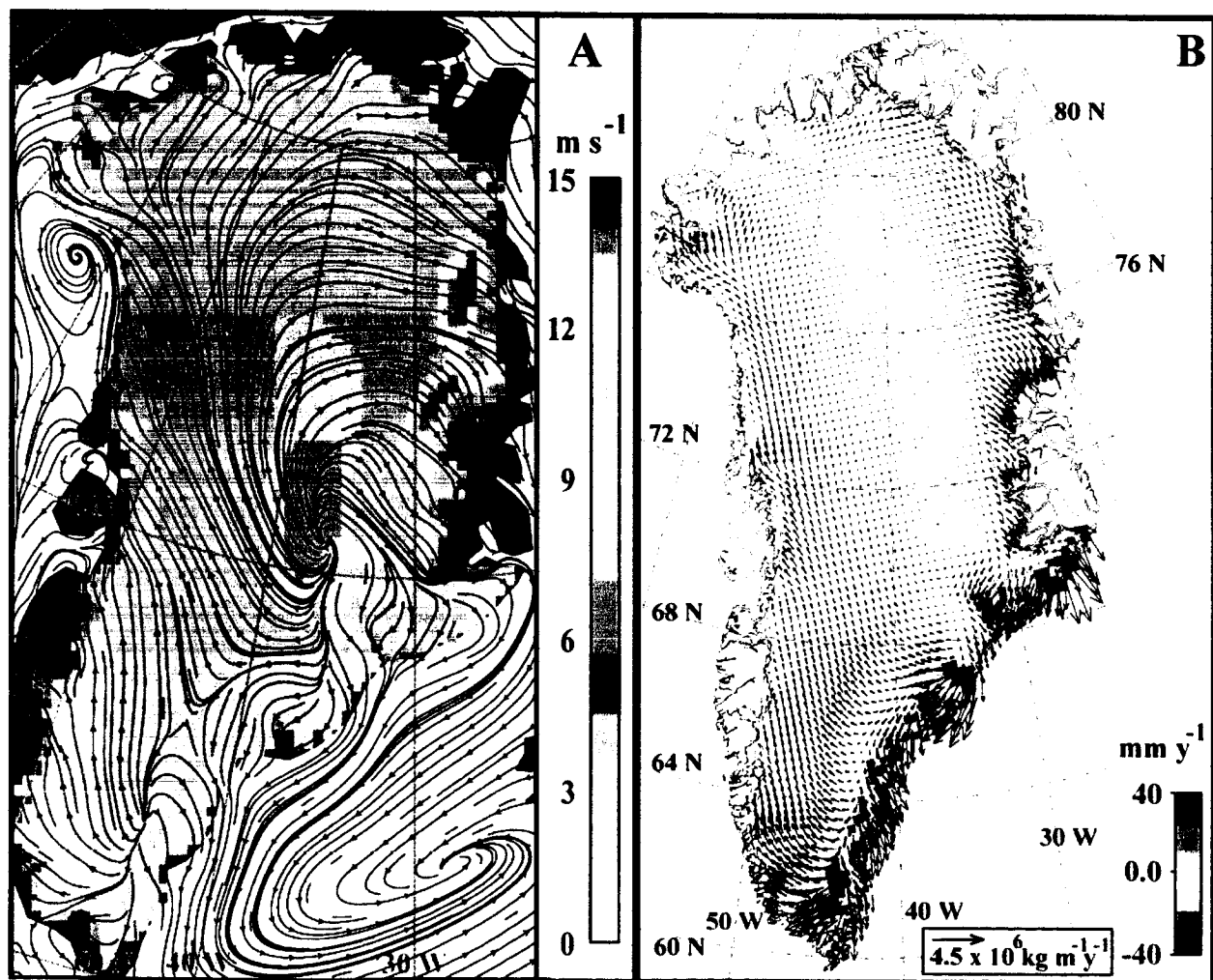

Figure 4.7. (a) Scalar mean wind speed with vector mean wind direction streamlines for the 1991–2000 period. Ice-free tundra is colored brown. Wind speed magnitudes are shown for the ice sheet only. (b) Blowing-snow transport vectors and spatial divergence patterns.

Simulated wind directions correspond well with AWS observations, including net easterly flow in the vicinity of South Dome, southeasterly flow at North Greenland Ice Core Project (NGRIP), and westerly flow at the Tunu-N AWS. Numerous interesting circulation features are evident, some where AWS do not exist, including channelized flow within glacier topographic basins, e.g., the Kangerdlussuaq glacier. This simulated pattern is similar to the results of Bromwich et al. [1996] for wintertime winds, though based on a 10-year average and a much more sophisticated atmospheric model. Streamlines over the adjacent seas are indicative of the persistent low pressure systems between Iceland and Greenland in the Denmark Strait and in northeast Baffin Bay. These cyclonic patterns explain regional maxima in precipitation in which adjacent coastal regions have net onshore flow. A low pressure trough along the west Greenland coast manifests in a subsynoptic cyclonic signature in wind streamlines.

The wind speed magnitudes are now described. Curiously, distinct regional annual wind speed maxima (15 m s^{-1}) are simulated to occur over Droning Louise Land and another nunatak region to the south in northeast Greenland (Figure 4.7a). In the model, these nunatak regions are treated as ice-only owing to inaccurate land surface classification. Thus we speculate the existence of an over amplified katabatic wind. However, we also note a convergence of wind streamlines. Other than this anomalous region, a strong katabatic wind region (up to 13 m s^{-1}) is simulated at intermediate elevations (~1000–2000 m) surrounding the ice sheet. The summit region also has minimal wind speeds (5 m s^{-1}) owing to less katabatic influence, despite occasionally very strong winds associated with synoptic disturbances. A narrow region along the northern and western ice margin includes the minimum wind speeds for the entire ice sheet. This near-coastal wind lull was not obvious in the earlier relatively coarse (40-km) Polar MM5 simulations [Cassano et al., 2001]. This wind speed reduction has become a well-documented feature for ice sheets, on the basis of AWS observations [e.g., Wendler et al., 1997; Bintanja, 1998; Steffen and Box, 2001], and has been linked to cold air pooling and a weakening of the katabatic tendency along the ice sheet margin [Galle'e and Pettre', 1998]. Absolute minimum winds are simulated near the Petermann glacier along the northwestern slope.

e. Snow Transport and Divergence

Owing to much more abundant snowfall in the southeast as compared to west Greenland, a region of maximum blowing-snow transport and divergence is found over the southeastern slope (Figure 4.7b). Regions of divergence (negative values) are associated with acceleration of the katabatic wind, pronounced along the relatively steep southeastern slope. Convergence zones are evident where katabatic winds decelerate along with blowing-snow transport and in large-scale basins, such as the Kangerdlussuaq glacier, where maximum drift snow convergence of approximately 35 mm yr^{-1} is simulated. Maximum drift snow divergence is simulated in the east over the Geike Plateau north of the Kangerdlussuaq glacier (Table 4.2). Patterns of drift snow convergence are resolved near the ice margin, owing to decreases in snow transport due to increasing snow entrainment thresholds and deceleration of the katabatic wind. Absolute maximum drift snow convergence is located near Narssarssuaq and near the confluence of the Kangerdlussuaq glacier. The divergence patterns in Figure 4.7b are a large-scale approximation of the combined effects of spatial changes in snow transport and blowing snow sublimation. The calculated divergence patterns imply an assumed steady state equilibrium of snow transport and blowing-snow sublimation across the 24-km model grid given that redistribution of individual particles likely cannot exceed even a few kilometers owing to the relatively short ice particle lifetimes in turbulent suspension [e.g., Schmidt, 1982]. By assumption of a steady state

equilibrium between particle loss by sublimation and the introduction of new particles from saltation impacts, one may infer residual redistribution. However, this may be an invalid assumption for the following reasons: Over the relatively large 24-km length scale, there are nonlinear spatial gradients in wind speed, temperature, and snow availability. Perhaps more importantly, the water vapor flux divergence from the combined effects of spatial divergence of blowing-snow transport and surface snow and blowing-snow sublimation is not explicitly balanced by the parameterizations incorporated here. Therefore we do not attempt to quantify redistribution, i.e., as a residual of the divergence field and QS. However, we have attempted experimentally to incorporate the spatial divergence term into the surface mass balance field. The result implied too liberal snow availability in southeast Greenland owing to the fact that precipitation is so often detected there that snow removal can exceed the annual precipitation rate. We must therefore refine the model for snow availability to depend on more than simply time since last snowfall. Elsewhere, the effect of incorporating snow transport divergence had little effect on the surface mass balance distribution. We do not incorporate divergence into our surface mass balance estimates.

f. Accumulation Rate

The accumulation rate, represented by precipitation minus surface snow and blowing-snow sublimation, is shown in Figure 4.8 on the same scale as the total precipitation.
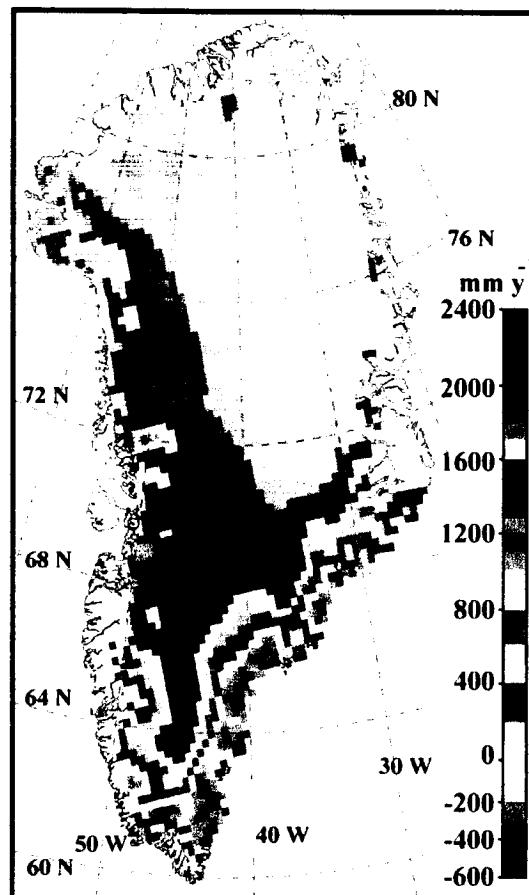

Figure 4.8. Accumulation 1991–2000, equal to precipitation minus surface snow and blowing-snow sublimation.

The spatial distribution closely resembles that of climatologies based on ice cores and snow pits [e.g., Ohmura et al., 1999], again with the dominant orographic maxima cited in the discussion of precipitation results. This presentation of the accumulation distribution contains more detail than in the former climatologies, including regions where net surface water vapor flux apparently exceeds precipitation over Droning Louise Land, resulting in a negative specific accumulation rate, i.e., A$\approx$100 mm yr^{-1}. Negative accumulation rate implies the presence of blue ice zones, observed from an aerial vantage point and not always in the lee of nunataks. Furthermore, there is evidence of blue ice zones at these locations in NASA Moderate-Resolution Imaging Spectroradiometer (MODIS) satellite observations, but apparently not on such a large scale as implied here. Elsewhere, the accumulation patterns are suggestive of an extremely complex spatial pattern and very large mass fluxes in the southern part of the ice sheet, dominated by precipitation.

g. Melt

Comparing the total energy for each component of the surface energy balance for the ice sheet as a whole suggests that radiation fluxes provide 99% of the melt energy. This predominance results from the net canceling of turbulent sensible and latent heat fluxes and the fact that the ground heat flux and heat flux from rain collectively represent a very small fraction (less than 0.3%) of the total melt energy.
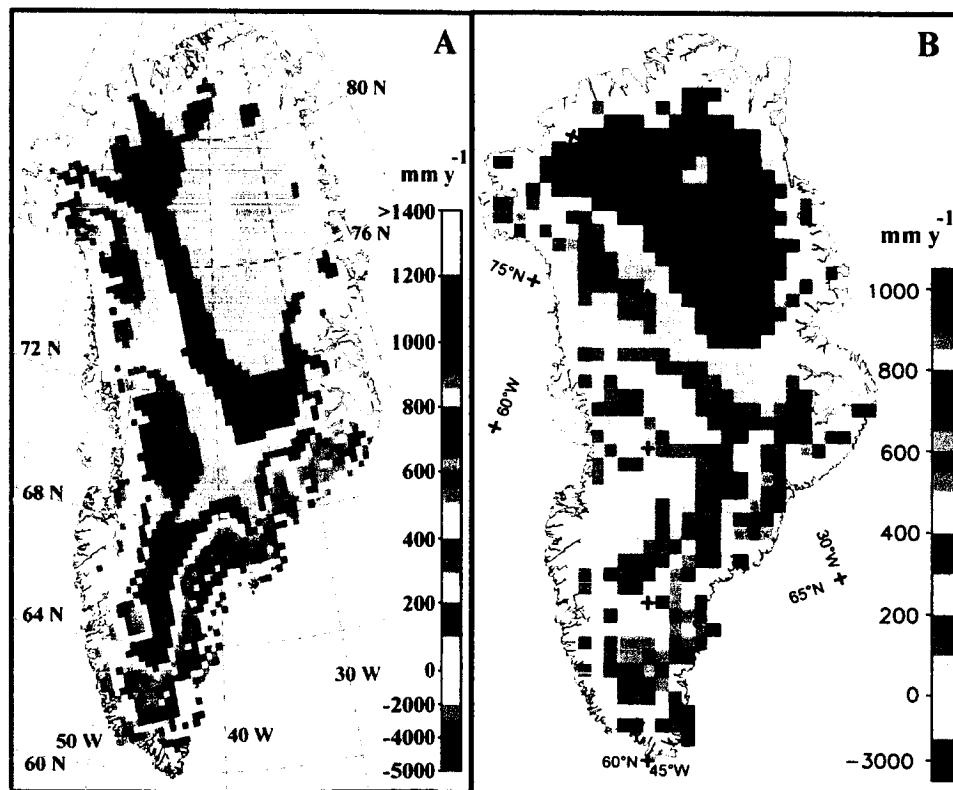
Figure 4.9. Surface mass balance 1991–2000 (a) based on Polar MM5 simulations and (b) courtesy of Zwally and Giovinetto [2001]. Equilibrium line is at the interface of gray and colored grid cells. One minor difference in color tables is that we exchange light yellow with light orange in Figure 4.10a for values between 400 mm yr^{-1} and 450 mm yr^{-1} to reserve yellows for extremely large surface mass balance in the southeast. The negative scale in Figure 4.10a spans a larger range than in Figure 4.10b.

The spatial distribution of melt days (Figure 4.9a) indicates maximum melt duration along the southwestern slope, with maximum values near Frederiksha°b Isblink. Greater melt frequency in the west versus the east is likely related to less sea ice extent in that region owing to the warm west Greenland current [Cappelen et al., 2001]. Given an apparent 3-K cold bias in surface temperature, the number of melt days must be significantly larger than 109. Maximum meltwater production is simulated near the extreme southeastern slope near Kap Cort Adelaer (Table 4.2). Other regional melt maxima exist, notably, from Kap Farvel along the southeast slope north to Kap Ryder; along the southwest slope; and in the northeast, near Zachariae Isstrøm.

h. Runoff

Runoff source regions are concentrated along a narrow strip of the ice sheet near the coast. Concentrated areas of maximum runoff are simulated in the west, on extensive low-lying low-albedo areas, namely, south of the Jakobshavn glacier and on the Frederiksha°b Isblink. Spatially discontinuous runoff maxima are evident along the southeast margin and west of Narssarssuaq (Figure 4.9b and Table 4.2). Runoff maxima are simulated in southeast Greenland, despite extremely large accumulation rates. Assuming no lateral flow resistance, runoff is simulated to originate as far as 250 km from the coast. The extreme interior values are, however, very small and hardly contribute to the total runoff value.

i. Surface Mass Balance

The 10-year mean surface mass balance distribution derived by combining simulations of precipitation, surface evaporation/sublimation, blowing-snow sublimation, and runoff is shown in Figure 4.10a. The spatial structure is indicative of a highly complex pattern in the surface mass balance, with extremely large spatial gradients, e.g., in southeast Greenland, where surface slope and both accumulation and ablation mass fluxes are largest. Regional maxima in positive surface mass balance distinctly emerge in three regions along the western slope, i.e., above the cyclonic feature over northeast Baffin Bay (Figures 4.5a and 4.7a), north of Rinks Isbrae at 72°N, and southeast of Nuuk/Godtha°b near 63°N. These regional maxima are associated with the topographic enhancement of precipitation rates. The regions of most intense negative surface mass balance occur along the southeast near sea level, and a broad (144 km), more intense melt region exists along the central western slope south of the Jakobshavn glacier. Ablation is simulated to dominate the surface mass balance in broad parts of the north and northeast slope apparently owing to low precipitation rates and low surface slope angles.

We have plotted our result on an equivalent color scale as the independent surface mass balance estimate given by Zwally and Giovinetto [2001], hereinafter referred to as ZG2001 (Figure 4.10b). Both maps exhibit an equivalent macroscale pattern. Largest differences in the spatial structure are notably where there are gaps in the input data for the climatological accumulation distribution used by ZG2001, i.e., along the southeast slope and regarding the precise location of the orographic maximum implied by earlier glacier survey data [i.e., Ohmura and Reeh, 1991; Ohmura et al., 1999]. The ZG2001 map does not include as broad of an ablation zone along the northern slope and may be explained by the fact that the ZG2001 result represents
an earlier and relatively cold period [Box, 2002]. The Polar MM5 result is supported by the observation of 1.4-m net annual surface ablation on the Petermann glacier [Huff et al., 2002]. Another major difference is that the extremes are significantly larger in the Polar MM5

simulations, -6 m to +2 m as compared to -3 m to +1.5 m given by ZG2001, likely because the higher (24-km) Polar MM5 spatial resolution can resolve finer spatial variability compared to the ZG2001 50-km grid.

4.4.3. Annual Total Ice Sheet Mass Fluxes

Table 4.3 lists annual total ice sheet mass balance components over the 10-year simulation. Precipitation is the largest single component, which is mostly balanced by surface snow and blowing-snow sublimation, runoff, and iceberg discharge. The magnitude of annual surface snow and blowing-snow water vapor fluxes are nearly equivalent in this simulation, consistent with De′ry and Yau [2001]. Polar MM5 annual precipitation and water vapor mass fluxes are significantly larger than in the HIRHAM model [Box and Rinke, 2003]. Other than the magnitude of these fluxes, the year-to-year variability, as measured by the range in values, is indicative of the background noise, by which a single annual sample could be a poor representative of the normal state of the ice sheet climate. The range of values in integrated mass balance components, such as surface mass balance and runoff, is as large as the 10-year average magnitude. The effects of an evolving ECMWF operational analysis product will probably contribute to a larger interannual variability in the model results. However, data inhomogeneities are of secondary importance, as determined from Polar MM5 comparisons with AWS data and as temperature and precipitation variability lead to coherent surface mass balance response, as shown in section 4.5. The results in Table 4.3 are sorted by decreasing surface mass balance. The years 1998 and 1995 stand out as years of relatively small or negative surface mass balance (and maximum runoff) while 1992 and 1996 emerge as maximum positive years with minimum runoff. This pattern is consistent with coastal temperature anomalies and passive microwave- derived melt extent [Abdalati and Steffen, 2001]. Although we find no obvious relationship between accumulation and runoff, as suggested by Mote [2003], this hypothesis is consistent with potential retention results; that is, there is less meltwater retention in warm years owing to larger melt relative to accumulation. The average retention fraction pr for grid cells with less than 100% retention is given and indicates that approximately 23% of accumulated snow is retained as internal accumulation, as compared to 29% used by Mote [2003]. Maximum melt extent in our simulations was measured as the count of grid cells where the surface temperature reached the melting point at least in one 6-hourly case. The results from this have proven difficult to compare with measurements of melt extent [e.g., Abdalati and Steffen, 2001], given that both techniques employ thresholds and that Polar MM5 can resolve minute amounts of melt that may not be visible in passive microwave data. However, the 30% interannual variations between the two estimates are in agreement.

Using the iceberg discharge (239 km^3 yr^{-1}) and basal melting (32 km^3 yr^{-1}) estimates from Reeh et al. [1999], we compute a net negative ice sheet total mass balance for the 1991–2000 decade of -78 km^3 yr^{-1}. Zwally and Giovinetto [2000] derived a value of -55 km^3 yr^{-1} representative of a recent climatological value. On the basis of a series of aircraft laser altimeter surveys spanning 1993 to 1999, Krabill et al. [2000] derived the total ice sheet balance to be -46 km^3 yr^{-1}. A more negative mass balance assessment is mainly attributable to the inclusion of mass loss by blowing-snow sublimation and statistically significant (4-K) springtime warming in the 1990s along western Greenland [Box, 2002]. The year-to-year range in the surface mass balance is large, ±145 km^3 yr^{-1}. Our mass balance estimate corresponds to a eustatic sea level contribution from Greenland of 2.2 mm (assuming 0.002826mm km^{-3}) over the 1991–2000

41

decade, or approximately 15% of the current estimated ~1.5 mm yr^{-1} [Church et al., 2001] sea level rise.

Table 4.3. Greenland Ice Sheet Mass Balance Components Based on the Polar MM5 Atmospheric Model[a].

Year	Precip.	Surface Sublim./Evap.	Blowing-Snow Sublim.	Melt	Max. Melt Extent[b]	Accum. Area, %	Runoff	p_n[b] %	SMB[b]	IMB[b]
1992	585	64	41	175	0.96	90.2	127	26.7	353	82
1996	673	58	46	325	0.99	84.9	250	24.6	319	48
1991	629	63	38	402	1.19	82.4	305	23.9	223	48
2000	624	62	40	401	1.17	82.4	303	22.4	219	52
1999	595	62	37	370	1.31	83.4	284	22	212	59
1997	642	67	41	427	1.19	82.9	336	22.4	198	73
1993	580	56	37	378	1.05	81.0	297	21.9	190	81
1994	508	60	41	317	1.03	83.5	247	23.7	160	111
1995	516	63	42	429	1.27	77.9	353	20.7	58	213
1998	555	71	41	539	1.37	76.6	449	19.3	6	277
Mean	591	63	40	376	1.15	82.5	295	22.8	193	78
Range	165	15	9	364	0.41	13.6	322	7.4	359	359

[a]Components are given in km^3 yr^{-1}. Precip., precipitation; sublim., sublimation; evap., evaporation; accum., accumulation.
[b]Max. melt extent × 10^6 km^2; p_n is the fraction of retained meltwater; SMB refers to surface mass balance, and IMB refers to total ice sheet mass balance.

4.4.4. Equilibrium Line Variations

At elevations where accumulation and ablation balance, i.e., surface mass balance equals zero, an equilibrium line is said to exist. The general pattern in our simulations is of equilibrium line altitude (ELA) decrease along the western slope of the ice sheet with increasing latitude (Figure 4.10), consistent with observations summarized by an ELA parameterization available from ZG2001.
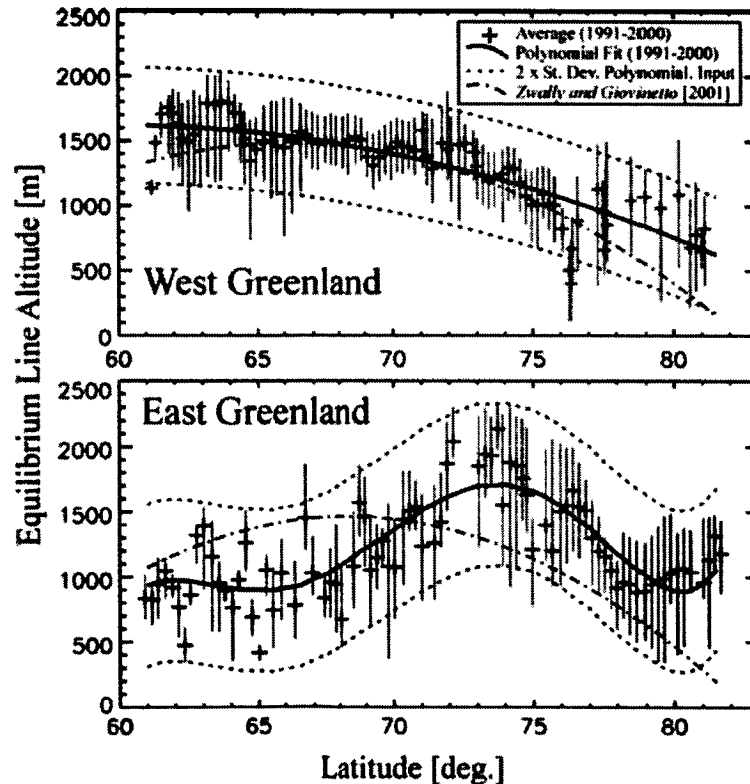

Figure 4.10. Average, minimum, and maximum equilibrium line altitude variations in Polar MM5 simulations (1991– 2000) including parameterizations.

Polynomial fits to our results are given in Table 4.4. On a regional scale, inflections in the ELA versus latitude pattern result from regional changes in topography (including precipitation shadow effects) and the proximity of dominant cyclonic systems. The curves also reflect the relative importance of ablation, e.g., a tendency for less melt at lower elevations toward the north. The increase in ELA in west Greenland north of 77°N is caused by the precipitation shadow north of the northwest branch of the ice sheet. In this case, owing to nearly constant regional ablation patterns, ELA increases. The pattern in east Greenland is indicative of a general ELA increase from 60°N to 74°N, followed by a decrease. East Greenland ELA variability exceeds that of west Greenland with 2 standard deviations of the 10-year latitude-varying sample corresponding to 636 m and 447 m, respectively. However, ELA variability varies with latitude and increases in precipitation shadow regions. There is little difference between our results and those of ZG2001 for western Greenland between 65°N and 72°N. Elsewhere in the west, our fit implies either a recent shift in Greenland ice sheet surface mass balance toward increased ablation, an overly negative surface mass balance in our simulation, and/or little constraint of the ZG2001 fit from insufficient observational data. To corroborate an increased ablation rate, the ZG2001 ELA parameterization reflects observations from a generally earlier time period (1960s to 1990s) characterized by cooling [Box, 2002]. In east Greenland, little agreement between our results and those of ZG2001 is evident. Our simulations indicate a much more complex east Greenland ELA pattern. Important to note is that apparently nowhere over the ice sheet is ELA at or below sea level.

Table 4.4. Polynomial Coefficients of Parameterized Equilibrium Line Altitude Variations With Latitude Over the East and West
Greenland Ice Sheet Slopes.

	Coefficient					
	α_0	α_1	α_2	α_3	α_4	α_5
West	−5.9311E + 03	2.5268E + 02	−2.1132E + 00			
East	−3.202998E + 07	2.311199E + 06	−6.648512E + 04	9.530192E + 02	−6.806712	1.937770E-02

4.4.5. Surface Mass Balance Sensitivity

Simulated temperature and precipitation anomalies for annual melt seasons (1 April to 30 September) exhibit meaningful correlations with simulated surface mass balance anomalies. Interannual accumulation and ablation variability causes equilibrium line altitude (ELA) fluctuations. Therefore ELA provides a useful indicator of the combined influence of thermal and precipitation forcing on surface mass balance. West Greenland ELA thermal variability is characterized by average sensitivity of +98 ± 40 m K^{-1}, while east Greenland sensitivity is +109 ± 68 m K^{-1}, larger apparently from larger surface slope. Ambach [1989] estimated perturbations in ELA under different climate scenarios, including a general 79-m positive shift in ELA given a 1-K warming and 10% precipitation rate increase with a negligible influence of cloud amount anomalies. The results of our simulations indicate that the sensitivity of ELA to temperature and precipitation anomalies, however, varies significantly with latitude, dominated by regional accumulation and to a lesser extent ablation variability. ELA sensitivity to precipitation generally decreases with latitude from -200 m (mm yr^{-1})$^{-1}$ at 61°N to -1500 m (mm yr^{-1})$^{-1}$ at 72°N along the west and east slopes. This trend is interrupted along the eastern slope by the complex of mountains, while along the western slope, the ELA sensitivity decreases to roughly 60 m (mm yr^{-1})$^{-1}$ at 70°N followed by an increase to the northern limit approaching an extreme in sensitivity of 2500 m (mm yr^{-1})$^{-1}$. The general pattern of ELA sensitivity to temperature and

precipitation anomalies suggests a dominance of thermal factors on surface mass balance in the southern part of Greenland, with a relative increase in the importance of precipitation anomalies as the thermal sensitivity decreases with increasing latitude.

Zuo and Oerlemans [1997] deduced values of surface mass balance sensitivity ranging from -30 to -97 mm yr^{-1} K^{-1} for specific regions over the Greenland ice sheet using an empirical model for summer temperature anomalies based on terrestrial station data. In the following, we evaluate surface mass balance sensitivities based on annual and seasonal anomalies. First, we found no correlation of annual mean temperature anomalies with surface mass balance anomalies for the entire elevation range of the ice sheet. If only the area below ELA defined using the polynomials in Table 4.4 is considered, a sensitivity of -90 mm yr^{-1} K^{-1} (r = -0.50) to annual temperature variability is evident. When considering only the summer (JJA) temperature anomalies, the sensitivity for the whole ice sheet is -13 mm yr^{-1}K^{-1} (r =-0.82), and for the area below ELA the sensitivity is -64 mm yr^{-1} K^{-1} (r = -0.95), keeping in mind, however, that some runoff originates from above ELA. It is noteworthy that both 1992 occupies the largest positive surface mass balance anomaly and the most negative temperature anomaly and 1998 exhibits the opposite pattern. The years 1991, 1996, and 2000 defy this pattern and suggest other dominant factors, namely, precipitation. Therefore a more meaningful sensitivity is based on the multiple regression of surface mass balance anomalies with temperature and precipitation anomalies. The regression equation for surface mass balance dependence (mm yr^{-1}) on annual anomalies for the entire ice sheet is

$$\Delta SMB = -49.5\Delta T + 1.41\Delta P \tag{4.7}$$

where ΔT is the annual temperature anomaly in K yr^{-1} and ΔP is the annual precipitation anomaly in mm yr^{-1} (r = 0.87). When the temperature variability from summer only is considered, with annual precipitation, the result is

$$\Delta SMB = -12.3\Delta T + 0.67\Delta P \tag{4.8}$$

and is characterized by a high correlation (r = 0.96) and smaller sensitivities because seasonal temperature anomalies are relatively large. If only the area below ELA and summer anomalies are considered, the correlation coefficient remains high (r = 0.96), and the sensitivity is

$$\Delta SMB = -65.1\Delta T + 0.33\Delta P \tag{4.9}$$

However, equation (4.9) is heavily biased in terms of ΔP by 1992, which is in contrast to the general pattern, with both the largest negative precipitation anomaly and the largest positive surface mass balance anomaly. The year 1992, therefore, defies a typical climate sensitivity and has been linked with cooling associated with the Mount Pinatubo volcanic eruption [Abdalati and Steffen, 1997]. For general climate sensitivity simulations we recommend equation (4.8).

Wild et al. [2003] project that in a future climate warming scenario, precipitation rates over Greenland may increase and even dominate surface mass balance change. With our limited 10-year sample, we find a small yet statistically insignificant positive correlation (r = 0.31) between annual temperature and precipitation anomalies. In the extreme warmest (1998) and coldest (1992) years of our sample, for example, there is no apparent correlation between temperature and precipitation anomalies, despite a robust correlation with surface mass balance. Therefore it seems that thermal factors dominate Greenland surface mass balance sensitivity rather than precipitation variations.

4.5. Summary

The Polar MM5 regional climate model, run over Greenland for 10 years (1991–2000), has provided new insight into spatial and temporal patterns of ice sheet surface mass balance variability. Unprecedented spatial details of glaciometeorological patterns over the Greenland ice sheet have been resolved with the relatively high 24-km model horizontal resolution, as compared with previous global climate model (GCM) studies. A major advantage of a regional climate model approach over statistical climatologies is to evaluate interannual variability, which indicates meaningful links between temperature and precipitation anomalies and surface mass balance.

We have evaluated the relative importance of numerous terms in the surface mass balance and conclude that melting is a dominant process in Greenland surface ice sheet mass balance, as compared to precipitation. The range in mass balance parameters over the 10 annual simulations (1991–2000) is suggestive of extremely large year-to-year variability. For example, the 10-year range in ice sheet surface mass balance values is equivalent to the magnitude of this flux. However, some of this variability may be attributable to changes in the archived ECMWF operational analyses over the 10-year period. Runoff variability, simulated given meltwater production estimates and a simple annual meltwater retention model, is characterized by 50% interannual variability. Other parameters exhibit large interannual variability. However, it is this variability that is of primary interest in understanding ice sheet response to climate changes. Using an estimate for iceberg discharge, we conclude that Greenland ice sheet mass balance, as a whole, is negative and has contributed -1.5 mm to eustatic sea level change over the 1991–2000 decade. In comparison with earlier estimates, Greenland ice sheet mass balance appears to have become more negative, consistent with coastal temperature increases observed during this decade. The general pattern of equilibrium line altitude sensitivity to temperature and precipitation anomalies suggests a dominance of thermal factors on surface mass balance in the southern part of Greenland, with a relative increase in the importance of precipitation anomalies as the thermal sensitivity decreases with increasing latitude.

A number of meaningful conclusions about specific processes relevant to ice sheet mass balance are now made. Because of the general net canceling of turbulent sensible and latent heat fluxes in the windy part of the ablation zone, the predominant source of melt energy is net radiation. Although liquid precipitation appears to contribute as much as 70% of the annual total precipitation for near-coastal glaciers in the extreme maritime south, the direct contribution of rain to melt rates over the ablation zone as a whole appears to be extremely small. Although albedo reductions owing to rain on snow events are certainly influential for melt onset, these were not investigated here. Regional maxima and minima in precipitation are linked with topographic variations in the context of dominant storm tracks. The surface net water vapor flux distribution includes the region of net water vapor deposition of up to $+15$ mm yr^{-1} and covering much of the area above -2700-m elevation, a result consistent with net surface water vapor flux derived from automatic weather station observations. However, also including blowing snow sublimation may render the net surface water vapor flux negative over the entire ice sheet. A regional maximum in precipitation in western Greenland at 72°N coincides with relatively high variability in regional topography. Finally, minimum snow accumulation is negative given an apparent dominance of ablation, particularly in the form of modeled blowing-snow sublimation, at a location where precipitation rates are low and simulated strong winds contribute to large water vapor losses.

In situ observations from automatic weather station (AWS) networks supplemented by glaciological surveys are critical for assessing atmospheric model accuracy and for gaining insight into the causes of model biases. On the basis of model comparisons with AWS data, it became clear that temporal variability was well captured by the model; however, systematic (absolute) model biases, some seemingly small, were shown to have important consequences for surface energy balance, particularly when energy balance closure is exploited to derive meltwater volume. Model results depend strongly on model configuration, including spin-up time and land surface modeling (including surface albedo and meltwater retention). We conclude that each model configuration requires some accuracy assessment, even for seemingly small configuration changes, e.g., spatial resolution. This assessment is required not only for the state variables, i.e., temperature, humidity, pressure, and wind speed, but also for derivatives of the state variables, i.e., turbulent energy fluxes. Further, glaciohydrologic data from snow pits, ice cores, and ablation stakes are vital to assess modeled surface mass fluxes, i.e., accumulation rates and meltwater runoff. Given a sufficintly large sample of in situ observations from AWS networks and glaciological surveys, it was possible to construct statistical corrections to modeled melt energy biases to produce more realistic estimates for surface mass balance components including melt energy and blowing-snow sublimation rate. Comparisons with in situ observations thus have provided the basis for clear recommendations for future model development. These include an emphasis on a more detailed land surface (firn) model with more appropriate spin-up time to allow attainment of full cloud and precipitation development. With such refinements, regional climate model simulations will become an important bridge between AWS networks and large-scale climate studies based on remote-sensing techniques for the purpose of better understanding the ice sheet response to climate change.

Given the large uncertainties in the several mass balance components involved, our estimates lack an absolute uncertainty estimate. Further, the natural variability in ice sheet mass balance appears to be too large to provide an indisputable assessment of positive or negative mass balance. However, it is clear that warming would produce a negative mass balance trend. Future work must attempt to construct uncertainty estimates. This is a challenging task, given that there are currently insufficient observational data to firmly constrain ice sheet mass balance as a whole. Future work should be concerned with developing a model configuration that does not require empirical adjustment.

5. Modeled Antarctic precipitation and mass balance

Based on Bromwich, D.H., Z. Guo, L. Bai, and Q-S. Chen, 2004: Modeled Antarctic precipitation. Part I: spatial and temporal variability. *J. Climate*, **17**, 427-447. Partially supported by this project.

5.1 Introduction

Surface snow accumulation is the primary mass input to the Antarctic ice sheets, and it has long been recognized as a potentially important contributor to global sea level change. Precipitation is the dominant term among various components of surface snow accumulation (precipitation, sublimation/vapor deposition, and snow drift) (Bromwich 1988) and its spatial and temporal variability are necessary information to assess the surface mass balance. In the last three decades, three measurement methods have been used to estimate the precipitation and accumulation over the Antarctic ice sheets: direct measurements, remote sensing techniques, and glaciological approaches.

The surface measurements derived from these methods are not the only source of information, and atmospheric techniques can be used for direct simulation or indirect determination of precipitation and/or accumulation with better temporal and spatial resolution. Three atmospheric methods are available to estimate net accumulation: moisture flux budget calculations, numerical modeling and dynamic retrieval. The method of moisture flux budgets uses atmospheric moisture transport toward the continent to calculate the area-integrated surface mass balance (Bromwich 1988, 1990). The spatial resolution of this approach is limited because the precipitation minus sublimation (P-E) residual is the small net result of large moisture fluxes into and out of the region of interest. Cullather et al. (1998) used moisture flux calculations to evaluate spatial and temporal variability of Antarctic precipitation from European Centre for Medium-Range Weather Forecasts (ECMWF) operational analyses for 1985-1994.

In this study, the precipitation for Antarctica from 1979-99 has been retrieved by the "dynamic retrieval method (DRM)" using ECMWF/TOGA analyses (ECT) and ERA-15. Additionally, a regional atmospheric model, Polar MM5 has been run over Antarctica for July 1996 - June 1999, and the simulated precipitation is compared with the DRM precipitation. Also, to examine the spatial and temporal variability of modern precipitation over Antarctica, DRM-derived precipitation data are contrasted with simulated precipitation from ERA-15, ECT, and National Centers for Environmental Prediction (NCEP) / Department of Energy, Atmospheric Model Intercomparison Project -2 reanalysis (hereafter NCEP2). This study is intended to demonstrate the reliability of the dynamic retrieval method, and evaluate its ability in representing the spatial and temporal variability of Antarctic precipitation in comparison with Polar MM5 simulations and global analyses products.

5.2. Data

Short-term precipitation forecasts from three numerical analysis and reanalysis data archives are used to depict spatial and temporal variability of Antarctic precipitation in this study. Two of the archives consist of ECMWF (ERA-15) and NCEP2 reanalyses, which span 1979-93 and 1979-99, respectively, and are available at 6-h intervals on a 2.5° x 2.5° grid. The third dataset is the ECMWF operational analysis, for which daily forecast precipitation is only

available after 1991 on a roughly 1.25° x 1.25° grid. Due to the data absence before 1991, ECMWF forecast precipitation is obtained from a combination of the ERA-15 reanalysis (1979-1990) and ECMWF operational analysis (1991-1999). It is noted that there are some concerns with the ERA-15 (Bromwich et al. 2000) and NCEP2 (Hines et al. 2000) reanalyses.

5.3. The spatial distribution of Antarctic precipitation

The most reliable source for identifying the spatial distribution of Antarctic precipitation comes from the long-term annual accumulation depiction synthesized from glaciological data. Figure 5.1 shows the most recent accumulation compilation over the Antarctic ice sheets from Vaughan et al. (1999). The surface snow accumulation is the net result of snowfall, sublimation/deposition, drift snow effects, and runoff, and its primary components are precipitation and sublimation. With the surface wind fields from the model output, the impact of drift snow redistribution on snow accumulation is also assessed.

Figure 5.2 shows the annual precipitation minus sublimation simulated by the Polar MM5. Sublimation is derived from the simulated latent heat flux. Compared to the accumulation analysis of Vaughan et al. (1999) all major features are reproduced by the Polar MM5. Both maps show large values along the coast of East and West Antarctica, and over the Antarctic Peninsula, and small amounts over the plateau of East Antarctica and around the Ross and Filchner/Ronne ice shelves, and Lambert Glacier. The spatial distribution of the model predicted P-E distribution is in good qualitative agreement with the accumulation analysis of Vaughan et al. (1999). Additionally, minimum values around Dronning Maud Land, Victoria Land, and Marie Byrd Land, and maximum values over the Antarctic Peninsula, southern part of the Ross Ice Shelf, and in the coastal region of the southeastern corner of the Bellingshausen Sea match that of Vaughan's analysis (see Fig. 1.2 for locations). Comparing these two maps, several differences also exist. First, areas enclosed by the 20 and 50 mm yr^{-1} contour lines in the simulated field are larger than those shown by Vaughan et al. (1999) and the simulated P-E values in the enclosed areas are smaller than the climatologically depicted annual accumulation from Vaughan et al. (1999). Second, the area with small simulated P-E values around the southern part of the Lambert Glacier is much smaller than that from Vaughan et al. (1999) As discussed below, the divergence of drift snow transport due to the strong katabatic winds in this area partially contributes to the difference between the simulated P-E and observed accumulation. Third, although the accumulation peaks along the Antarctic Peninsula in the Polar MM5 output and Vaughan's analysis with a maximum around 2000 mm, the accumulation distributions differ in this area. It is believed that the coarse spatial resolution of the Polar MM5 accounts for this difference. The largest errors are associated with the coastal regions, and accumulation is underestimated in the central interior while it is generally overestimated in the coastal areas by Polar MM5.

Cassano et al. (2001) found that Polar MM5 also overestimates the precipitation amounts along the steep slopes of the Greenland Ice Sheet. It is hypothesized that the deficiencies in the interior precipitation simulations reflect the limited ability of Polar MM5 in representing clear sky precipitation. Studies show that clear sky precipitation is continuously formed in the interior of Antarctica without any organized synoptic-scale process, and comprises a large fraction of the total precipitation (Bromwich 1988). Figure 5.3 shows the annual cycle of accumulation derived from Polar MM5 simulations and moisture flux budget calculations using ECMWF analysis for the Antarctic continent (Cullather et al. 1998, for 1985-1994) above various

elevation intervals. A broad peak of accumulation is found during March-October for the three elevation bands examined in moisture flux budget calculations. This peak in the interior of Antarctica is believed to result from the increased clear sky precipitation during the polar night when moisture saturation is enhanced by the strong radiative cooling (Bromwich 1988), and it does not appear in the Polar MM5 simulations for accumulation above 2500m.
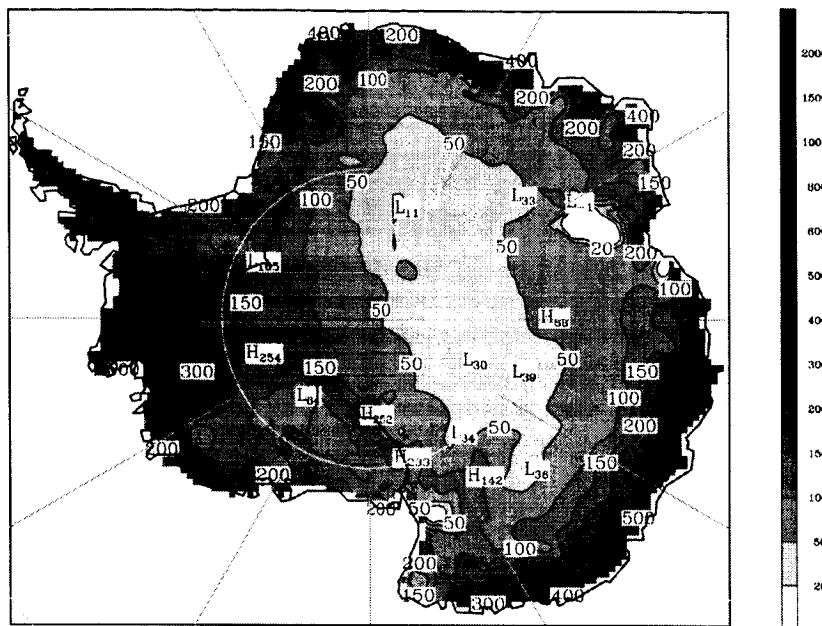

Figure 5.1 Vaughan et al. (1999) long-term accumulation distribution (mm yr-1 water equivalent).
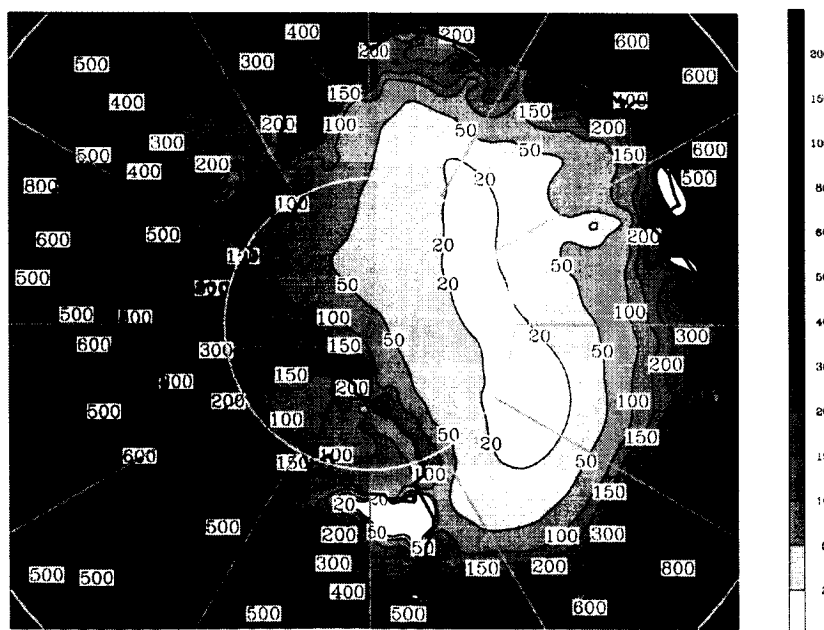
Figure 5.2 Annual precipitation minus sublimation for Jul 1996–Jun 1999 simulated by Polar MM5 (mm yr^{-1} water equivalent).

Figure 5.3 Annual cycle of accumulation derived from Polar MM5 (PMM5) simulations and moisture flux budget calculations using ECMWF analyses for Antarctic continent above various elevation intervals (mm yr^{-1} water equivalent).

Figure 5.4 Polar MM5 modeled fraction of the annual precipitation (PR) that is removed from the surface by sublimation (SU).

Fig. 5.4 shows the annual fraction sublimation/precipitation (SU/PR) from the Polar MM5 output. The mean annual sublimation field from Polar M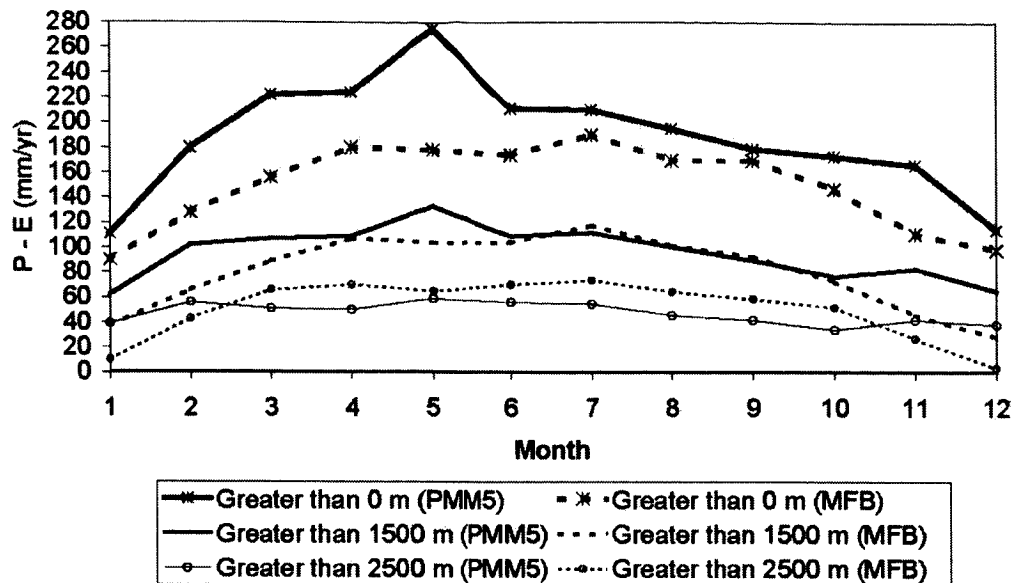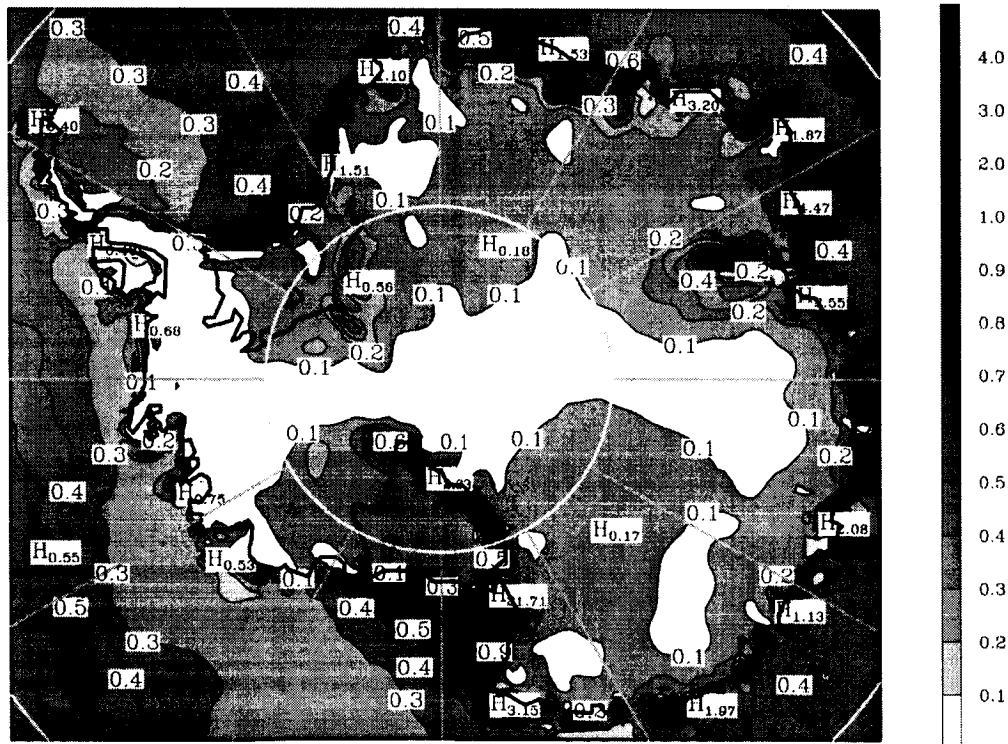M5 simulations is very close to that estimated by van den Broeke (1997). Similar to van den Broeke (1997), four areas clearly stand out where sublimation on an annual basis removes more than 70% of the precipitation: east Dronning Maud Land, the Lambert Glacier basin, Victoria Land, and the southern part of the Ross Ice Shelf. Averaged over the continent, the model predicts that 13.5% of the annual precipitation over Antarctica is removed by sublimation. Over most areas in the interior of the Antarctic ice sheets, SU/PR is less than 20%. Similiar to Genthon and Krinner's (2001) findings, deposition (or inverse sublimation) also contributes to the surface accumulation, and the contribution is not negligible. In addition, areas with a large contribution of sublimation removal are not associated with systematic underestimation of surface accumulation, and areas with small contribution of sublimation removal are not associated with systematic overestimation of surface accumulation. Therefore, the deficiencies found in simulated accumulation are more likely attributed to deficiencies in precipitation rather than sublimation.

Katabatic winds are prominent climatological features of the Antarctic boundary layer. The associated drift snow effects are of importance for the redistribution of the snowfall, and for modification of the local net accumulation by direct removal of snow across the coastline and by enhancing evaporative loss from the surface. The Byrd snow drift project (Budd et al. 1966) executed during 1962-1963 found that the observed drift snow transport in the layer from 1 mm to 300 meters above the snow surface, $Q_{10^{-3}}^{-300}$ (units: $g\,m^{-1}s^{-1}$), can be represented by the relation

$$\log \left| Q_{10^{-3}}^{-300} \right| = 1.1812 + 0.0887 |V_{10}| \tag{5.1}$$

where V_{10} is the wind speed at 10 m above the snow surface. The snow transport follows the wind direction. Thus, the drift snow effects can be expressed as the divergence or convergence of the snow transport vectors.

$$D = \nabla \bullet \left(\frac{|Q_{10^{-3}}^{-300}|}{|V_{10}|} V_{10} \right) \tag{5.2}$$

Using the above equation with wind field output from Polar MM5 simulations at 3-h intervals, drift snow effects can be estimated. Figure 5.5 shows annual mean divergence of drift snow transport estimated from the surface wind fields simulated by Polar MM5 for July 1996 - June 1999. The dashed lines are elevation contours. The results show that there are complex divergence and convergence patterns of drift snow transport over Antarctica, especially along the coast. From this figure several features can be observed. First, areas with large drift snow transport convergence and divergence are located around escarpment areas where there is large katabatic wind acceleration. Second, drift snow transport generally diverges over most areas of East and West Antarctica with relatively small amounts. Third, areas with large snow transport divergence are generally accompanied by areas with large snow transport convergence nearby, and this indicates that the drift snow transport is of local importance for redistribution of the snowfall. Finally, the southern part of the Lambert Glacier is one of the areas with the largest divergence of drift snow transport.
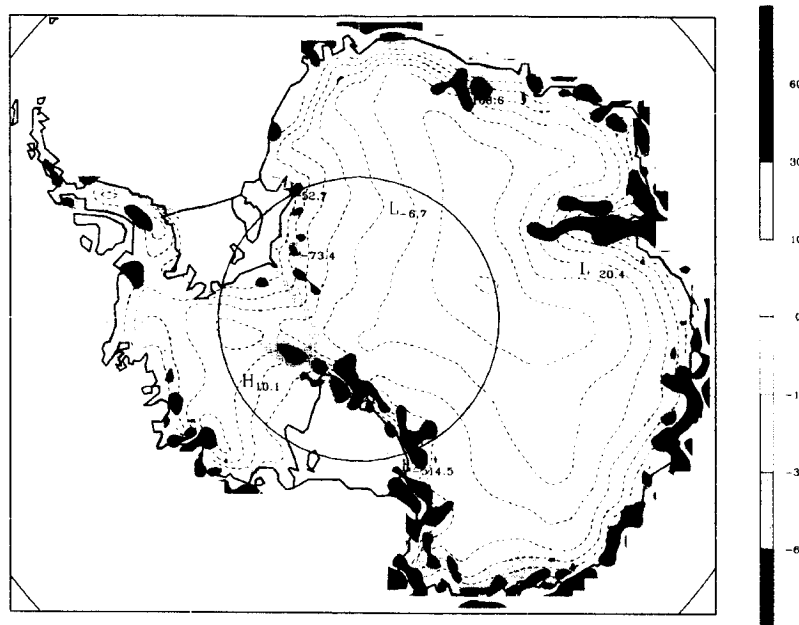
Figure 5.5 Mean annual divergence of drift snow transport over Antarctica (mm yr^{-1} water equivalent). The drift snow transport is estimated by the Budd et al. (1966) equation from wind fields at 10 m above the surface. The wind fields are derived from the Polar MM5 simulations.
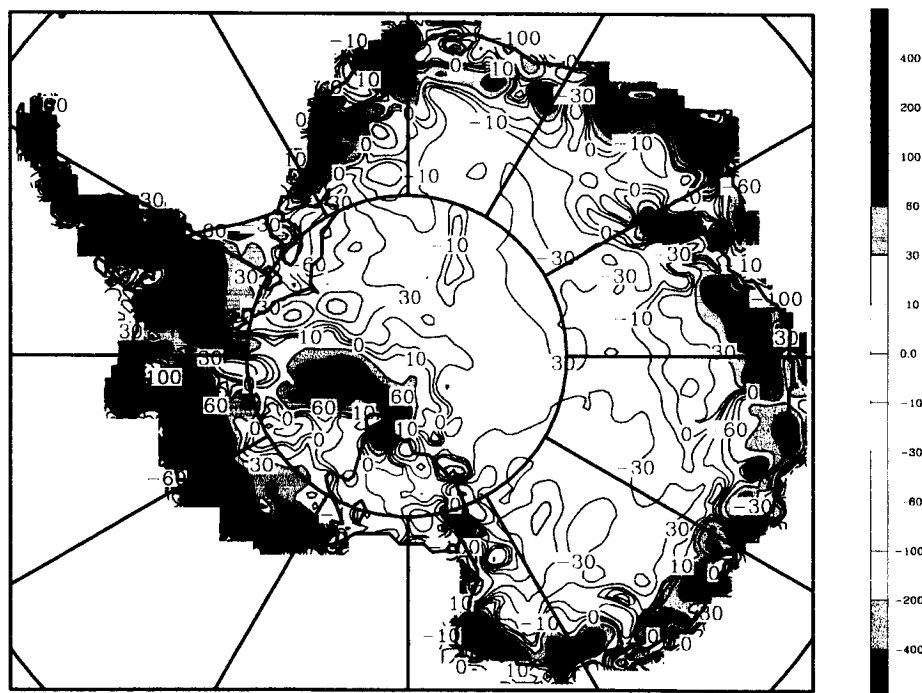
Figure 5.6 Annual accumulation (precipitation minus sublimation and divergence of drift snow transport) estimated from Polar MM5 simulations minus Vaughan et al. (1999) compiled accumulation (mm yr^{-1} water equivalent).
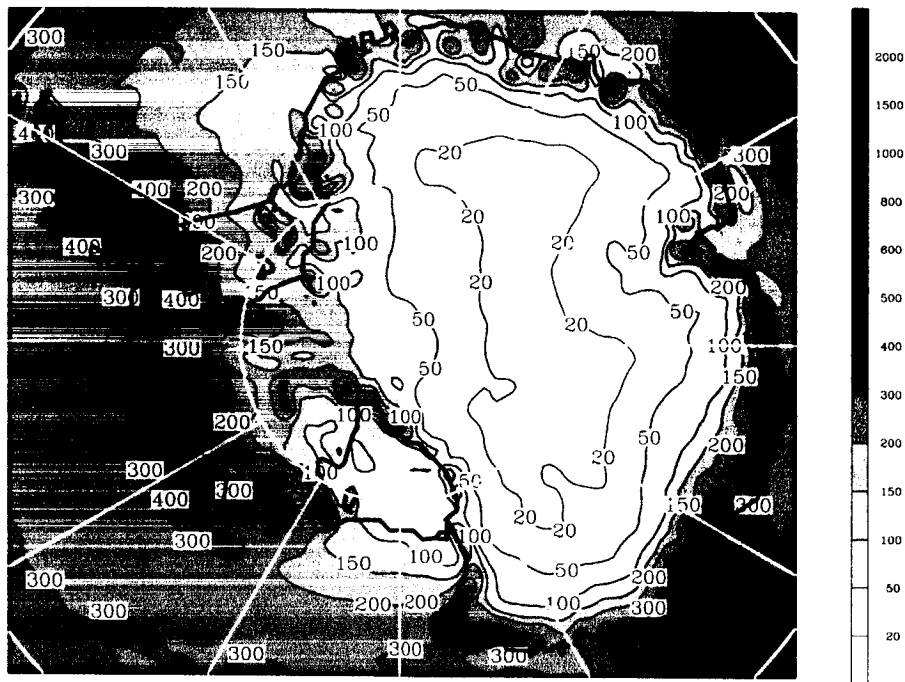
Figure 5.7 Mean annual precipitation for 1985–99 derived from the dynamic retrieval method (mm yr^{-1} water equivalent
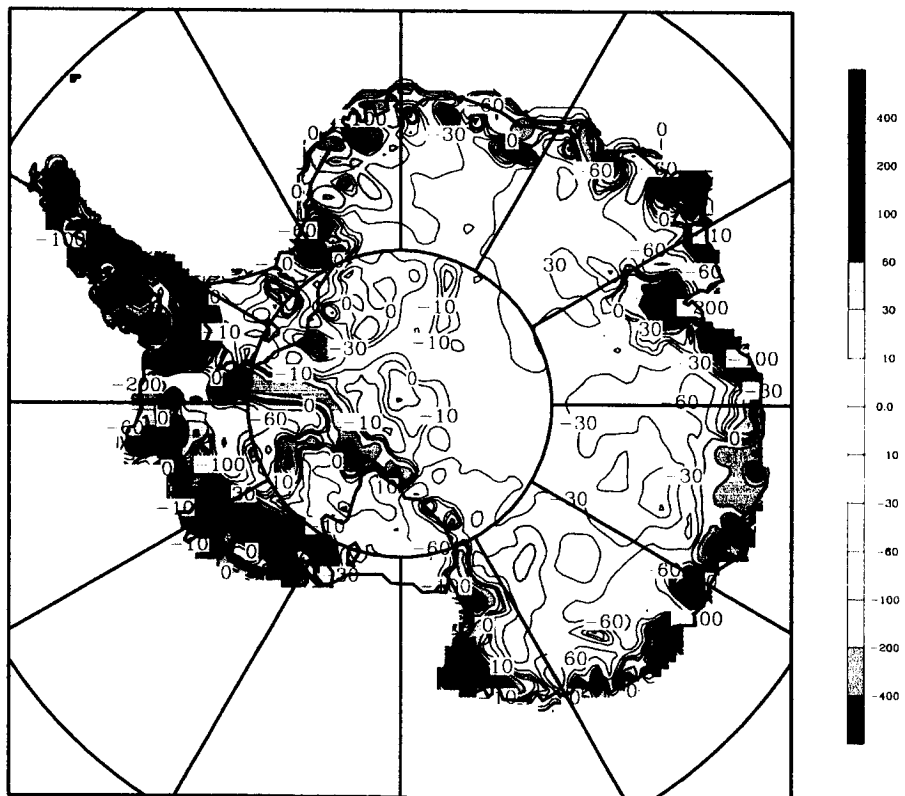
Figure 5.8 Annual precipitation for 1985–99 derived from the dynamic retrieval method minus Vaughan et al. (1999) compiled accumulation (mm yr^{-1} water equivalent).
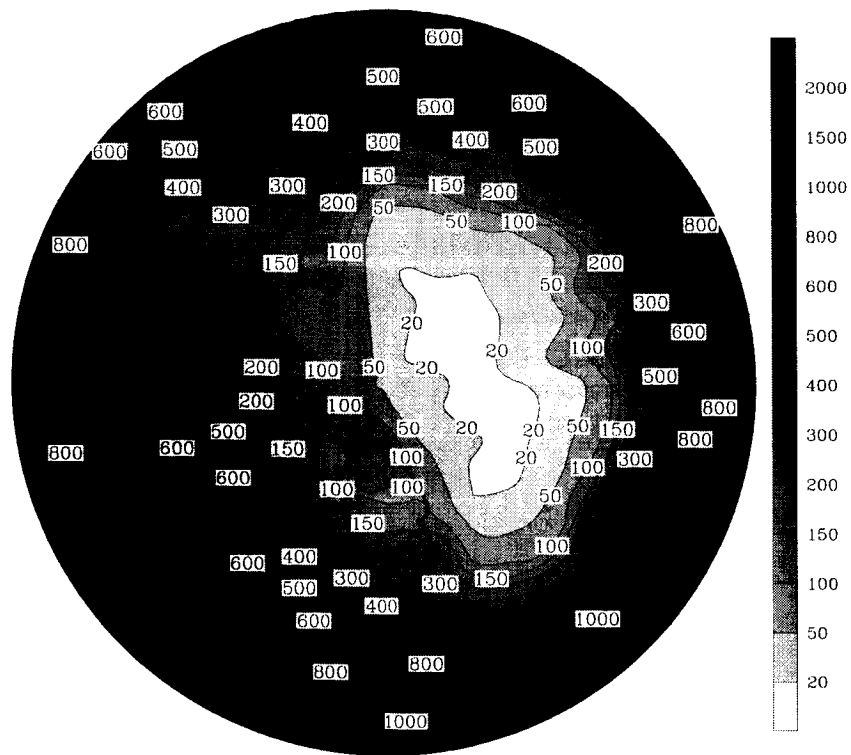
Figure 5.9 Mean annual precipitation produced by NCEP2 for the years 1979–99 (mm yr^{-1} water equivalent).

Figure 5.10 The mean annual precipitation produced by ECT for the years 1991–99 (mm yr^{-1} water equivalent).

The divergence of drift snow transport under strong katabatic winds partially contributes to the difference between the simulated P-E and observed accumulation over this area. It is noted that this method neglects the enhancement of sublimation of snow when it is airborne (Gallee, 1998, Bintanja and Reijmer 2001) and does not consider variations in the quantity of snow available for transport.
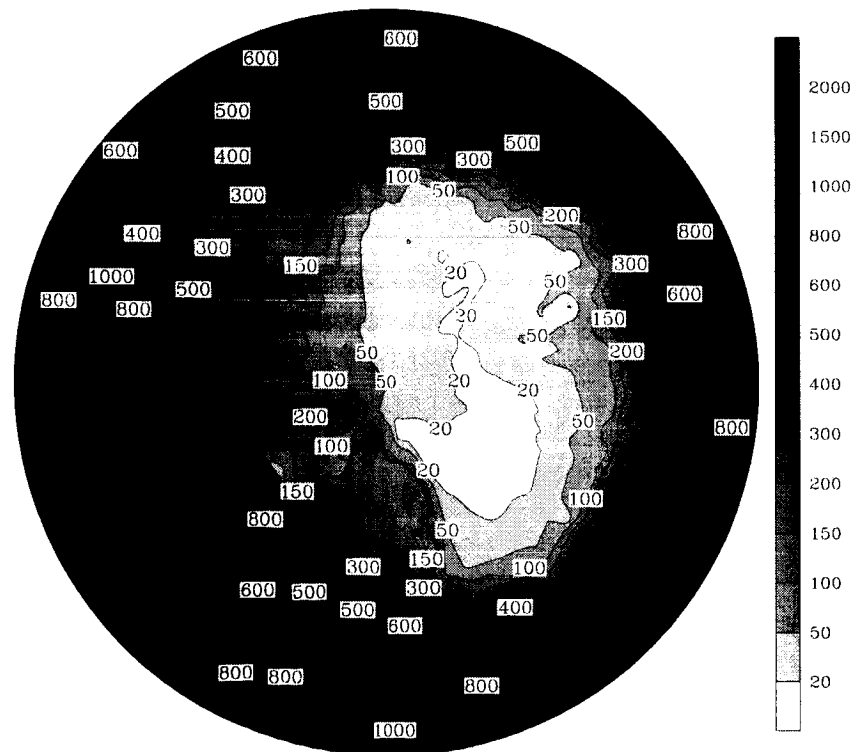
In Fig. 5.6, the Vaughan et al. (1999) accumulation compilation (Fig. 5.2) is subtracted from the averaged P-E-D field derived from the Polar MM5 simulations (Fig. 5.5). When compared to Fig. 5.4 (Polar MM5 P-E minus Vaughan et al. (1999)), this plot demonstrates that accounting for the drift transport with this method generally improves the accumulation estimates. Not surprisingly, the largest errors in accumulation are associated with the coastal regions. As before, it is also observed that accumulation is underestimated in the central interior while it is generally overestimated in the coastal areas by Polar MM5.

Figure 5.7 shows the annual mean precipitation determined from the DRM using ECMWF analysis (DRM_ECT, 1985-1999). All major features in the spatial distribution of Antarctic precipitation from the Polar MM5 simulations mentioned above are well captured by the DRM. These features include the maximum values over the Antarctic Peninsula and a large amount of precipitation on the southern coast of the Bellingshausen Sea. Over Marie Byrd Land, the greatest precipitation occurs in the immediate coastal region and rapidly decreases inland. The primary difference is the deficient precipitation over the ocean derived from the DRM compared to that simulated by Polar MM5. Studies show that the dependence of effective precipitation on the relative humidity is spatially complex (Sinclair 1994). The fixed value of c_r is optimized for use over the Antarctic continent, and is set too high for use over the ocean (contributing to the underestimation of precipitation here). Also, only large scale condensation is considered by the DRM in computing precipitation; the omission of mesoscale convection and associated precipitation over the ocean contributes to the difference. The Vaughan et al. (1999) accumulation compilation (Fig. 5.2) is subtracted from the averaged P-E field derived from the DRM (Fig. 5.7) in Fig. 5.8. As with Polar MM5, a similar but less obvious problem in reproducing clear sky precipitation exists in the DRM, and a new scheme is currently being developed to represent clear sky precipitation events.

Figures 5.9 and 5.10 show the annual mean forecast precipitation from NCEP2 (1979-1999) and ECT (1991-1999), respectively. All modeled values from Polar MM5, DRM, ECT, and NCEP2 agree with each other in representing the general spatial features of the modern Antarctic precipitation. Because Polar MM5 and DRM use resolutions of 60km and 40km, respectively, they resolve more mesoscale precipitation features. In particular, NCEP2 shows a smoothed version of the annual mean precipitation distribution around the coast of the Bellingshausen Sea and Marie Byrd Land. While all datasets show a reasonable spatial distribution of Antarctic precipitation, it is also noted that they tend to underestimate the precipitation in the interior of Antarctic. Table 1 (following Reijmer et al. 2002) presents the annual mean precipitation from ice core measurements and model outputs at six locations with high elevation (Fig. 1.2). It shows that most modeled precipitation values are much less than their measured counterparts (around 30%-50% if sublimation is taken account). This suggests that simulation of the moist physical processes involved in Antarctic precipitation needs further improvement.

Table 5.2 compares the average annual precipitation and accumulation for all of Antarctica (Antarctic continent, Antarctic Peninsula, and floating shelves) from modeled values with the results reported by other investigators. The mean annual precipitation for the whole of

Antarctica, as computed from the DRM with ERA-15 and ECT data, is 179 and 195 mm yr-1, respectively. They are close to the forecast precipitation from ERA-15, ECT, and NCEP2. Considering annual sublimation of 29 mm yr^{-1} from Polar MM5 simulations, the mean annual mean net accumulation (P – E) is close to previously reported values (Cullather et al. 1998; Vaughan et al. 1999). However, mean annual precipitation and accumulation derived from the DRM and forecast precipitation from ERA-15, ECT and NCEP2 is much less than that simulated by the high resolution mesoscale model (Polar MM5) and a general circulation model (Ohmura et al. 1996). The mean annual precipitation for the whole of Antarctica estimated by the Polar MM5 is 215 mm yr-1. The sublimation on an annual basis removes about 13.5% of the precipitation, and the drift snow transport removes about 2.3% of the precipitation.

Table 5.1. The annual mean values of the observed accumulation [after Reijmer et al. (2002) except for the South Pole] and various modeled precipitation for six sites in the interior of Antarctica. Values preceded by ± indicate the standard deviation (P= precipitation, E=sublimation, PMM5=Polar MM5). References for accumulation values at each site, left to right respectively, are as follows: Herron (1982); Petit et al. (1982); Aoki and Coauthors (1998); Oerter et al. (2000); Legrand and Delmas (1987); E.-F. Mosley-Thompson (2002, personal communication).

	Byrd	Dome C	Dome F	DML05	Vostok	South Pole	Data source
Lat	80.00°S	74.50°S	77.32°S	75.00°S	78.50°S	90.0°S	
Lon	119.4°W	123.0°E	39.70°E	0.0°	106.9°E		
Elevation (m)	1530	3280	3810	2892	3488	2835	
Accumulation (mm yr⁻¹)	160	36 ± 5	30	62 ± 21	22.5	79 ± 7	Ice core (Byrd–Vostok), snow stakes (South Pole)
P (mm yr⁻¹)	146 ± 41	40 ± 14	22 ± 9	55 ± 19	14 ± 6	40 ± 10	NR2_P 1979–99
P (mm yr⁻¹)	168 ± 61	21 ± 6	7 ± 3	27 ± 7	5 ± 1	51 ± 6	ERA_P 1979–93
P (mm yr⁻¹)	126 ± 28	28 ± 6	20 ± 4	42 ± 13	15 ± 5	50 ± 10	ECT_P 1991–99
P (mm yr⁻¹)	154 ± 26	25 ± 9	15 ± 3	43 ± 8	20 ± 3	72 ± 12	DRM with ERA 1979–93
P (mm yr⁻¹)	165 ± 21	26 ± 12	14 ± 2	44 ± 14	23 ± 8	71 ± 14	DRM with ECT 1985–99
P (mm yr⁻¹)	144 ± 49	25 ± 6	26 ± 5	105 ± 4	18 ± 9	66 ± 7	PMM5 1996.7/1999.6
$P – E$ (mm yr⁻¹)	126 ± 46	22 ± 5	22 ± 5	96 ± 4	15 ± 8	64 ± 6	PMM5 1996.7/1999.6
E/P (%)	12.8	10.6	12.2	8.4	11.7	4.0	PMM5 1996.7/1999.6

Table 5.2. Comparison of recent estimates of Antarctic accumulation and precipitation. Values preceded by ± indicate the standard deviation.

Study	Estimate	Method	Value (mm yr⁻¹)
Giovinetto and Bentley (1985)	Accumulation	Glaciological data synthesis	143 ± 14
Vaughan et al. (1999)	Accumulation	Glaciological data synthesis	166
Ohmura et al. (1996)	$P – E$	Modeled precipitation minus evaporation from ECHAM coupled model	197
Cullather et al. (1998)	$P – E$	Atmospheric moisture budget from ECMWF, 1985–94	151 ± 13
This study	$P – E$	Modeled precipitation minus sublimation from Polar MM5, Jul 1996–Jun 1999	186 ± 16
This study	$P – E – D$	Modeled precipitation minus sublimation and drift snow divergence from Polar MM5	181 ± 16
This study	P	Modeled precipitation from Polar MM5, Jul 1996–Jun 1999	215 ± 15
This study	P	NCEP-DOE AMIP-2 reanalysis, 1979–2000	180 ± 12
This study	P	15-yr ECMWF Re-analysis, 1979–93	173 ± 7
This study	P	ECMWF TOGA analysis, 1991–99	188 ± 20
This study	P	Dynamic retrieval method with ECMWF reanalysis data, 1979–93	179 ± 5
This study	P	Dynamic retrieval method with ECMWF analysis data, 1985–99	195 ± 16
This study	E	Modeled sublimation from Polar MM5, Jul 1996–Jun 1999	29 ± 1
This study	D	Divergence of drift snow transport from Polar MM5, Jul 1996–Jun 1999	5

5.4. The temporal variability of Antarctic precipitation

Here, the temporal variability of Antarctic precipitation and the recent precipitation trends over the Antarctic ice sheets are presented. The temporal changes present in the precipitation time series produced by the DRM are contrasted with those derived from the analysis and reanalysis forecast products, and they are also compared with available ice core accumulation measurements.

a. Interannual variations of precipitation over Antarctica and its sub regions

Figure 5.11a compares the monthly mean modeled precipitation over all of Antarctica from various methods.
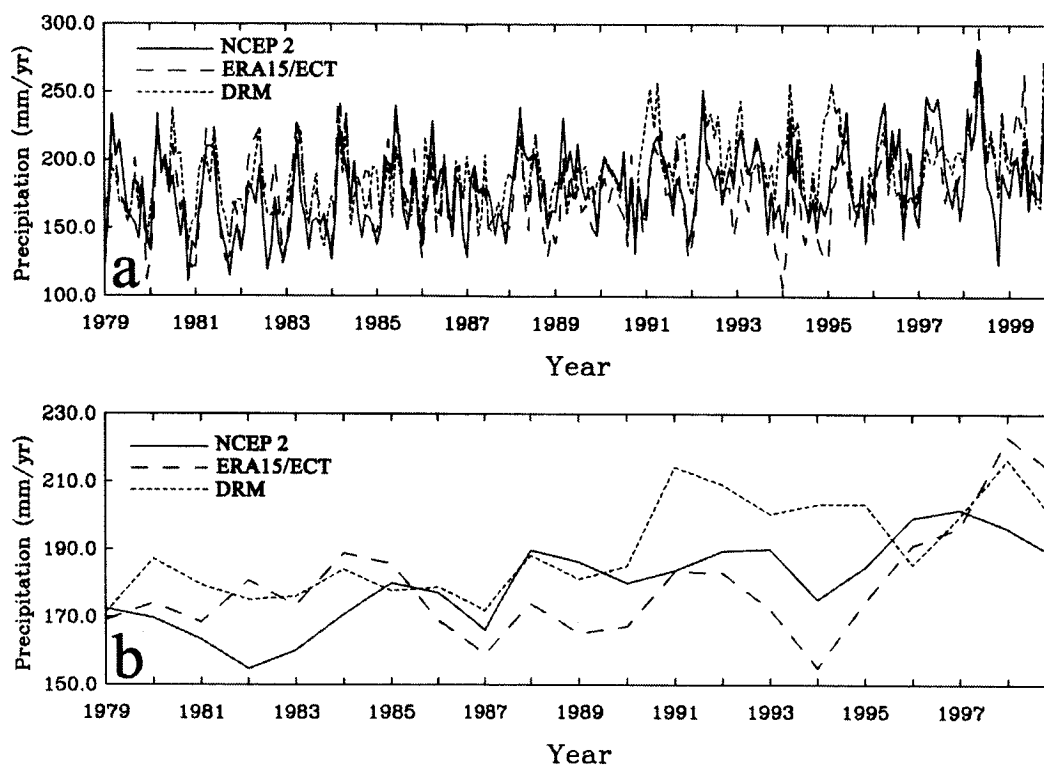

Figure 5.11 (a) Monthly and (b) annual time series for the modeled precipitation over all of Antarctica.
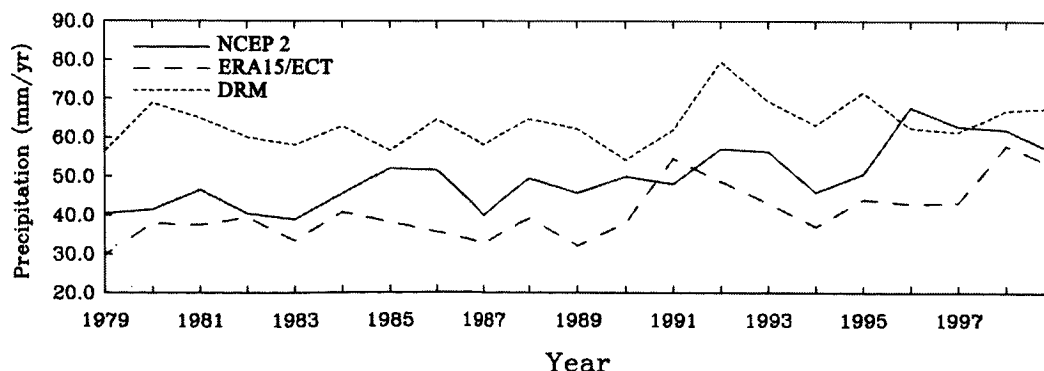

Figure 5.12 Annual time series for the modeled precipitation over Antarctica for elevations higher than 2000 m.
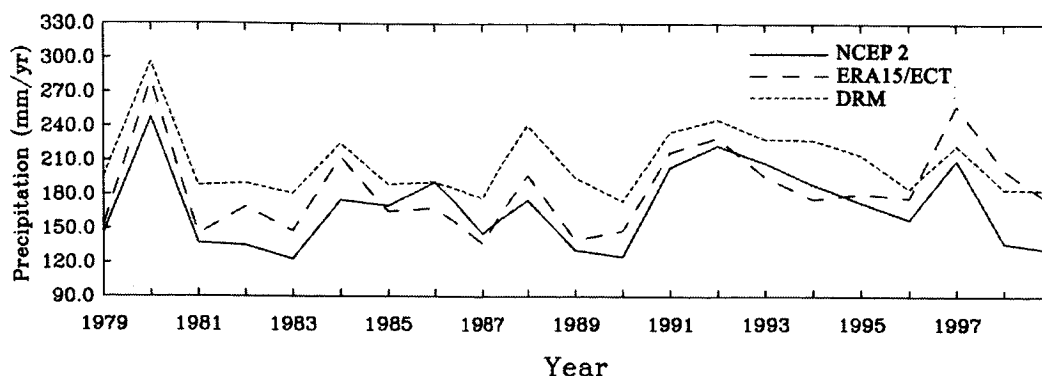
Figure 5.13 Annual time series for the modeled precipitation over the West Antarctic sector bounded by 75°–90°S, 120°W–180°.
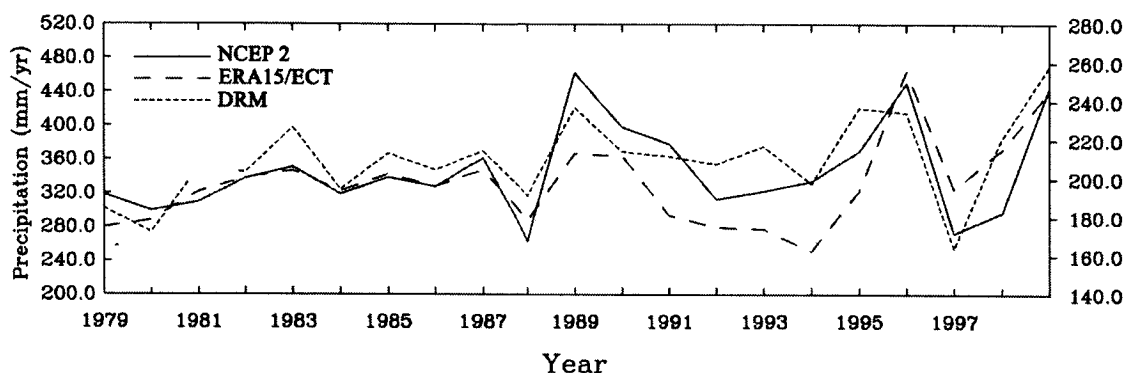

Figure 5.14 Annual time series for the modeled precipitation over South Atlantic sector bounded by 65°–75°S, 30°–60°W. Note that the right-hand scale is for DRM.

There is good agreement on seasonal time scales in modeled Antarctic precipitation among these data sets when averaged over all of Antarctica for both raw and detrended estimates (Table 5.3; r=~0.70; r^2=~0.50). The seasonality of modeled precipitation is generally identifiable with a maximum in winter and a minimum in summer. The annual time series for the modeled precipitation over all of Antarctica from various methods are shown in Fig. 5.11b. The estimates do not agree as well as for the seasonal case, especially for the detrended estimates, (r<~0.20; r^2<~0.04). In the DRM precipitation, the largest amount (215 mm yr^{-1}) occurs in 1998, and the smallest amount (176 mm yr^{-1}) occurs in 1987 and 1979. The 21-yr mean precipitation over all of Antarctica is 183 mm yr^{-1}, and the standard deviation is 15.3 mm yr^{-1}. The correlation between the ERA-15/ECT forecast precipitation and the DRM precipitation is poor from 1991-1995; these two time series converge by 1996. In September 1991 several major changes were made to the ECMWF forecast model, including increased horizontal resolution and dynamics modifications such as a new version of cloud treatment (ECMWF 1999). Inspection of the monthly mean ECT precipitation fields from this time through March 1995 reveal a significant degree of spectral noise; this problem disappeared with the implementation of a new version of the ECMWF forecast model in April 1995, which led to a greatly improved representation of cloud cover and forecast precipitation (ECMWF 1999). Better agreement between the DRM precipitation and ECT forecast precipitation after 1995 might indicate that the interannual variability of DRM Antarctic precipitation is more reliable during 1991-1995, since the method does not rely on the ECT precipitation fields, but rather on other ECT fields which were largely unaffected by the changes made in September 1991.

Because no cloud microphysics is included in the DRM, less artificial interannual variability will be introduced into DRM precipitation compared to the ECT forecast precipitation due to changing cloud and microphysics schemes.

Table 5.3. Monthly and interannual correlation (r) and variance (r^2) statistics for the raw and detrended time series in Figs. 5.11–16. Correlations that meet the 95% confidence interval are shown in bold type.

	Raw				Detrended			
	Monthly		Interannual		Monthly		Interannual	
	r	r^2	r	r^2	r	r^2	r	r^2
Fig.5.11: Precipitation over all of Antarctica								
ERA-15–ECT vs NCEP2	**0.73**	0.53	**0.5**	0.25	**0.71**	0.50	0.18	0.03
DRM vs ERA-15–ECT	**0.71**	0.50	**0.41**	0.17	**0.69**	0.48	0.08	0.01
DRM vs NCEP2	**0.67**	0.45	**0.58**	0.34	**0.61**	0.37	0.04	0.00
Fig5.12: Precipitation above 2000 m								
ERA-15–ECT vs NCEP2	**0.52**	0.27	**0.63**	0.40	**0.46**	0.21	0.2	0.04
DRM vs ERA-15–ECT	**0.48**	0.23	**0.51**	0.26	**0.48**	0.23	0.39	0.15
DRM vs NCEP2	**0.46**	0.21	0.37	0.14	**0.46**	0.21	0.15	0.02
Fig5.13: Precipitation over the West Antarctic sector								
ERA-15–ECT vs NCEP2	**0.85**	0.72	**0.82**	0.67	**0.85**	0.72	**0.83**	0.69
DRM vs ERA-15–ECT	**0.9**	0.81	**0.83**	0.69	**0.91**	0.83	**0.86**	0.74
DRM vs NCEP2	**0.81**	0.66	**0.87**	0.76	**0.82**	0.67	**0.88**	0.77
Fig5.14: Precipitation over the South Atlantic sector								
ERA-15–ECT vs NCEP2	**0.76**	0.58	**0.68**	0.46	**0.76**	0.58	**0.66**	0.44
DRM vs ERA-15–ECT	**0.71**	0.50	**0.61**	0.37	**0.71**	0.50	**0.57**	0.32
DRM vs NCEP2	**0.75**	0.56	**0.76**	0.58	**0.75**	0.56	**0.75**	0.56
Fig5.15: Modeled precipitation vs FB9815 ice core								
DRM vs measured	n/a	n/a	0.42	0.18	n/a	n/a	0.26	0.07
ERA-15–ECT vs measured	n/a	n/a	0.50	0.25	n/a	n/a	0.35	0.12
NCEP 2 vs measured	n/a	n/a	0.18	0.03	n/a	n/a	0.10	0.01
Fig5.16: Modeled precipitation vs South Pole snow stakes								
DRM vs measured	n/a	n/a	0.49	0.24	n/a	n/a	0.34	0.12
ERA-15–ECT vs measured	n/a	n/a	0.61	0.37	n/a	n/a	−0.21	0.04
NCEP 2 vs measured	n/a	n/a	−0.07	0.00	n/a	n/a	−0.07	0.01

Table 5.4. Temporal trend and uncertainty (at 95%) of the linear regression (mm yr^{-2} water equivalent) for the interannual data series in Fig. 11. Bold numbers represent trends that are significant at the 95% confidence level with respect to zero.

Dataset	Trend	Uncertainty	Years
Fig. 13: Precipitation over all of Antarctica			
DRM	**1.65**	0.80	1979–99
ERA-15–ECT	**1.35**	1.10	1979–99
NCEP2	**1.67**	0.59	1979–99

The annual time series for the modeled precipitation from various methods over Antarctica for elevations higher than 2000 m are shown in Fig. 5.12. It shows that the DRM precipitation over high elevations is much larger than that obtained from NCEP2, ECT and ERA-15 simulated precipitation. As discussed in the previous section, simulated precipitation is significantly underestimated in the interior of Antarctica by ECT, ERA-15 and NCEP2 in comparison with measured accumulation. Based on the results in Table 5.1, the DRM precipitation provides a better quantitative estimate of precipitation over the interior of Antarctica than the simulated precipitation estimates. The relative agreement between the estimates above 2000 m is similar to that for the estimates for the entire continent (Table 5.3), although the seasonal (monthly) correlations are lower, suggesting the differences in the precipitation algorithms are most marked over the continental interior. Because precipitation in the South Atlantic sector around the Weddell Sea, and the West Antarctic sector around the

Ross Sea (Fig. 5.1) is found to be highly correlated and anticorrelated with the SOI for the last two decades (Guo 2002, Guo et al. 2003b), special attention is paid to these two sectors. Figure 5.13 shows the annual time series for the modeled precipitation over the West Antarctic sector bounded by 75°-90°S, 120°W-180°. All three data sets agree closely with each other in reproducing both the seasonal (not plotted) and interannual variations in mean precipitation averaged over the West Antarctic sector (Table 5.3); all of the estimates correlate significantly at >0.80 for monthly and interannual scales for both the raw and detrended time series. Annual time series for the modeled precipitation over the South Atlantic sector bounded by 65°-75°S, 30°-60°W are shown in Fig. 5.14. Although precipitation over the South Atlantic sector is substantially underestimated by the DRM due to omission of mesoscale convection and associated precipitation and assumed high value of $c\ r$, good agreement is found in the seasonal (not plotted) and interannual variations in South Atlantic precipitation from the various methods. Monthly correlations are >0.70 and interannual correlations range from 0.57 to 0.76 for both raw and detrended estimates. As discussed in Guo et al. (2003b), the good agreements in the seasonal and interannual variations in these sectors indicate that the ENSO signals in the interannual precipitation variations are strong enough to survive reproduction by methods with different representation of physical processes. Outside West Antarctica, especially in the continental interior, the correspondence in interannual variations among these data sets is generally less than that found in the these two sectors.

b. Comparison of the interannual variations at measurement sites in Antarctica between the measured accumulation and modeled precipitation

Recently measured time series of net water equivalent accumulation at sites FB9815 and South Pole are compared to the retrieved precipitation from DRM and forecast precipitation from analysis and reanalysis data sets. These sites were selected because they provide a reasonable sampling of the environments in the interior of the Antarctic continent, and few choices are available for data comparison. The locations of these sites are shown in Fig. 5.1. The precipitation amounts at the grid points from various methods are interpolated to the measurement locations.
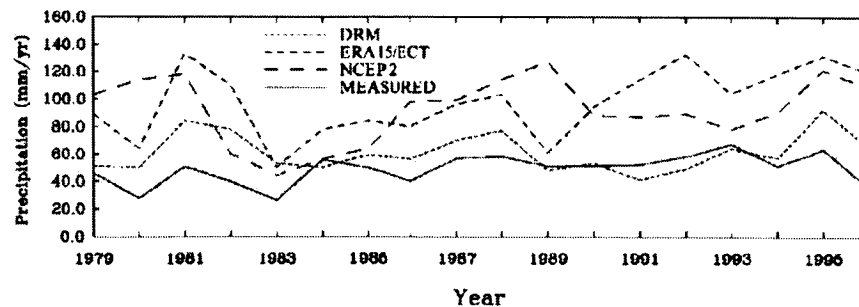
Figure. 5.15 The interannual variations of measured accumulation and modeled precipitation from various methods at the ice core site FB9815.

Figure 5.15 shows the interannual variations of the modeled precipitation from the various methods and the measured accumulation for 1979-96 at FB9815 (Oerter et al. 2000). There is reasonable agreement in the interannual variations between the measured accumulation and both the DRM and ERA15/ECT precipitation for the raw estimates (Table 5.3). The correlation between the measured accumulation and DRM precipitation is 0.42, and 0.50 for the measured accumulation and ERA15/ECT, and both are significant. The NCEP 2 accumulation does not correlate significantly for the raw data, and none of the estimates correlate significantly

for the detrended case. Both NCEP2 and ERA15/ECT appear to overestimate precipitation, considering the small sublimation and drift snow effects (Figs. 5.4 and 5.5) at this site, while the DRM estimates closely match the measured accumulation.
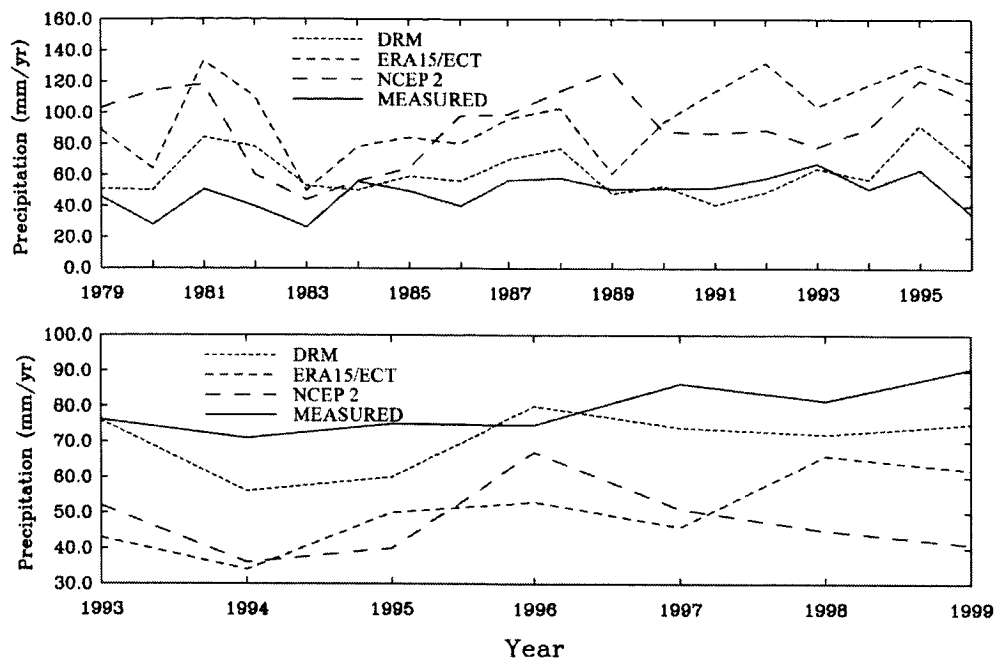

Figure 5.16 The interannual variations of measured accumulation (from 236 snow stakes) and modeled precipitation from various methods at the South Pole.

Figure 5.16 shows the interannual variations of modeled precipitation from the various methods and those of measured accumulation for 1993-1999 at South Pole Station (Mosley-Thompson et al. 1999). The measured accumulation values shown in Fig. 5.16 are annual accumulation averages for the 236 snow stakes of the South Pole OSU 1992 Network. It is found that the interannual variability of modeled precipitation at South Pole is not well represented by any of the methods. None of the estimates correlates significantly at the 95% confidence level with the measured precipitation for the raw or the detrended time series (Table 5.3), although the correlations for DRM and ERA15/ECT are 0.49 and 0.61, respectively for the raw time series. Due to the small sample size (7 yr), the data were also tested at the 90% confidence level; none of the correlations are significant at this level either. As noted in the previous section, precipitation in the interior of Antarctica is significantly underestimated by ECT, ERA-15 and NCEP2 (Table 1). Compared to forecast precipitation from ECT, ERA-15, and NCEP2, DRM precipitation follows the measured annual mean accumulation more closely.

c. Recent precipitation trends over the Antarctic ice sheets

The interannual variations of the mean precipitation from various methods over all of Antarctica for the last two decades are shown in Fig. 5.11. The reasonable agreement among the three methods (r ranges from 0.43 to 0.60; Table 5.3) implies a validation of the upward trend of +1.3 to +1.7 mm yr^{-1} from 1979-1999 (Table 5.4), which is significant at the 95% confidence level for all three datasets. This upward trend is in agreement with other studies (e.g., Morgan et al. 1991, Bromwich and Robasky 1993, Mosley-Thompson et al. 1995), and is notable in view of the complex trends in Antarctic surface temperatures (Comiso 2000, Doran et al. 2002).

Despite the reasonable agreement between the trends, overall it is noteworthy that there are temporal differences. The NCEP2 trend is almost consistently upward from 1982-1999. The ERA15/ECT trend is indistinguishable before 1994, when it turns abruptly upward. The DRM trend occurs mainly due to a "step" between two precipitation plateaus that occurs in 1990-1991; at this time ECT fields replace ERA15 in the DRM calculations.
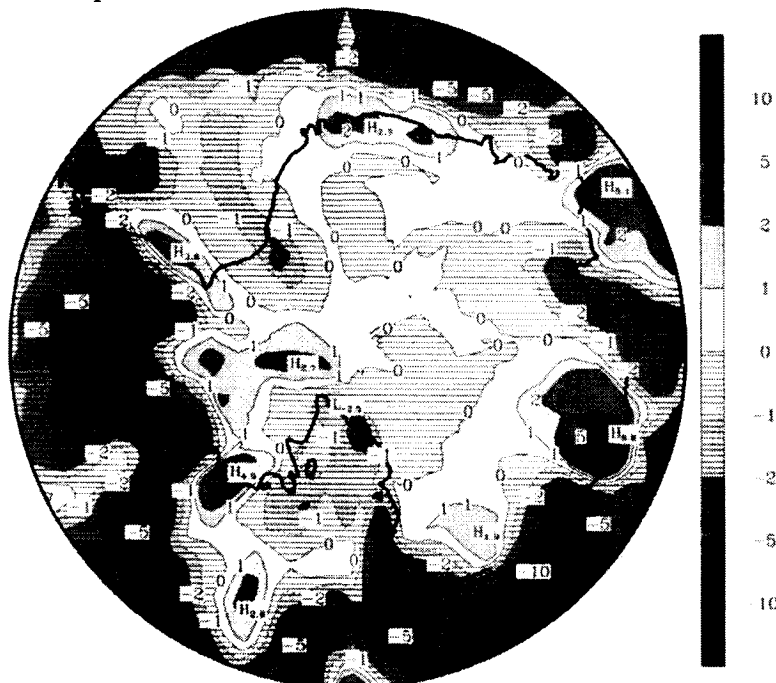

Figure 5.17 Temporal trend of the linear regression line (mm yr^{-2} water equivalent) for the forecast precipitation from ERA-15 (1979–93).
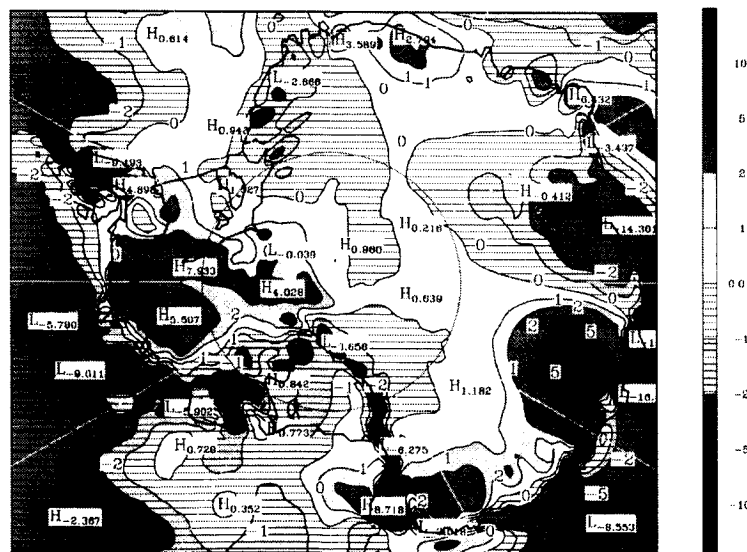

Figure 5.18 Temporal trend of the linear regression line (mm yr^{-2} water equivalent) for the retrieved precipitation amount from the dynamic retrieval method with ERA-15 (1979–93).

Because the use of a consistent data assimilation scheme helps avoid the artificial discontinuities of operational analyses, atmospheric reanalyses are particularly valuable for investigation of recent climate variability. Figures 5.17 and 5.18 show the spatial distribution of the linear trend from ERA-15 forecast precipitation and DRM precipitation with ERA-15. Although these two figures span the period 1979-1993, they are thought to generally depict the sign and spatial distribution of the trends throughout the 1980s and 1990s. Similar spatial patterns are present in the linear trend of the DRM precipitation with ECT (1991-1999), which is not shown here. Both increases and decreases can be found in recent precipitation rates over Antarctica. In general, there is reasonable agreement in the pattern of precipitation rate variation between these two figures. First, small changes in recent precipitation rate variations are found in the interior of Antarctica. A small increase in the recent precipitation rate around South Pole is consistent with the results of Mosley- Thompson et al. (1999). Second, there are two areas that show significant increases: central West Antarctica and the area around Law Dome (near 110°E). The recent increases in the precipitation rate around Law Dome are in agreement with previous findings from Morgan et al. (1991). Third, it is also found that the precipitation trend is weakly downward over much of the continental interior. This area, due to its high topography, is somewhat isolated from large synoptic systems in the Southern Ocean, and the implied increase in moisture fluxes toward Antarctica due to changes in the heat content of the Southern Ocean (discussed below) may have less of an impact here. Additional ice cores should be used to test the validity of the precipitation trends over Antarctica, such as those being collected by the ITASE project.

The simulated precipitation increase for 1979-1999 indicates that Antarctic precipitation removes an additional ~0.05 mm y^{-1} from the global ocean. This offset is small in relation to the observed global sea level rise of ~2 mm yr^{-1} (e.g., Douglas and Peltier 2002). The precipitation increase is consistent with the positive trend in sea surface temperatures observed in the midlatitudes of the Southern Ocean over the latter half of the 20th Century (Casey and Cornillon 2001) that encompass the source region of Antarctic precipitation (Delaygue et al. 1999).

5.5. Summary

Atmospheric numerical simulation and dynamic retrieval method with atmospheric numerical analyses are used to assess the spatial and temporal variability of Antarctic precipitation for the last two decades. First, the Polar MM5 has been run over Antarctica to study the Antarctic precipitation. With a horizontal resolution of 60km, the Polar MM5 has been run for the period of July 1996 through June 1999 in a series of short-term forecasts from initial and boundary conditions provided by the ECMWF operational analyses. In comparison with climatological maps, the major features of the spatial distribution of Antarctic precipitation are well captured by the Polar MM5. Drift snow effects on redistribution of surface accumulation over Antarctica are also assessed with surface wind fields from Polar MM5 in this study. There are complex divergence and convergence patterns of drift snow transport over Antarctica, especially along the coast. It is found that areas with large drift snow transport convergence and divergence are located around escarpment areas where there is large katabatic wind acceleration. In addition, areas with large snow transport divergence are generally accompanied by areas with large snow transport convergence nearby, indicating that drift snow transport is of local importance for the redistribution of the snowfall

The precipitation for Antarctica from 1979-1999 has been retrieved by a vertical motion calculation using ECMWF operational analyses (ECT, 1985-1999) and reanalysis (ERA-15, 1979-1993). The dynamic retrieval method is applied to retrieve the precipitation over Antarctica from 1979-1999 in this study. In comparison with glaciological estimates and Polar MM5 simulations, most major features in the spatial distribution of Antarctic accumulation are well captured by the dynamic retrieval results. In comparison with predicted values from ERA-15 (1979-1993), ECT (1991-1999), and NCEP DOE AMIP 2 (NCEP2, 1979-1999), dynamic retrieval calculations capture more mesoscale features of the precipitation distribution over Antarctica. In comparison with available ice core measurements from Dronning Maud Land the interannual variability of the Antarctic precipitation is reasonably represented by the dynamic retrieval results, having a significant correlation. However, in comparison with snow stake measurements from South Pole the correlation is not significant. The DRM precipitation is quantitatively more accurate than the NCEP2 and ERA15/ECT precipitation at both sites, following the measured accumulation more closely. A significant upward trend of +1.3 to +1.7 mm yr^{-1} for 1979-1999 is found from retrieved and forecast Antarctic precipitation that is consistent with results reported by other investigators. This indicates that additional water is being extracted from the global ocean and locked up in the Antarctic ice sheets, about 0.05 mm y^{-1}. While there is good agreement in this trend between all of the datasets, the interannual variability about the trend is not well captured on the continental scale. However, on the subcontinental scale, the interannual variability about the trend is well resolved for sectors in West Antarctica and the South Atlantic. It is also noted that the precipitation trend is weakly downward over much of the continent.

References

Aebischer, U., and C. Schar, 1998: Low-level potential vorticity and cyclogenesis to the lee of the Alps. *J. Atmos. Sci.*, **55**, 186-207.

Anthes, R.A., Y.-H. Kuo, and J.R. Gyakum, 1983: Numerical simulations of a case of explosive marine cyclogenesis. *Mon. Wea. Rev.*, **111**, 1174-1188.

Abdalati, W., and K. Steffen (1997), Snowmelt on the Greenland ice sheet as derived from passive microwave satellite data, *J. Clim.*, **10**, 165– 175.

Abdalati, W., and K. Steffen (2001), Greenland ice sheet melt extent: 1979–1999, *J. Geophys. Res.*, **106**(D24), 33,983– 33,988.

Ambach, W. (1989), Effects of climatic perturbations on the surface ablation regime of the Greenland ice sheet, west Greenland, *J. Glaciol.*, **35**(121), 311 – 316.

Aoki, S., and Coauthors, 1998: Preliminary investigation of palaeoclimate signals recorded in the ice core from Dome Fuji station, East Dronning Maud Land, Antarctica. *Ann. Glaciol.*, **27**, 338–342.

Ball, F.K., 1960: Winds on the ice slopes of Antarctica. *Antarctic Meteorology, Proceedings of the Symposium in Melbourne*, 1959, Pergamon Press, New York, 9-16.

Barry, R.G., 1981: *Mountain weather and forecast*, Methuen & Co., 313pp.

Barry, R.G., and G.N. Kiladis, 1982: Climatic characteristics of Greenland. *Climatic and Physical Characteristics of the Greenland Ice Sheet*, U. Radok, R.G. Barry, D. Jenssen, R.A. Keen, G.N. Kiladis, and B. McInnes, Eds., CIRES, Univ. of Colorado, 7-33.

Björnsson, H., F. Pálsson, M. T. Guðmundsson and H. H. Haraldsson, 1998: Mass balance of western and northern Vatnajökull, Iceland, 1991-1995. *Jökull*, **45, 35-58.**

Bintanja, R. (1998), The contribution of snowdrift sublimation to the surface mass balance of Antarctica, Ann. Glaciol., 27, 251–259.

Bintanja, R. (2001), Snowdrift sublimation in a katabatic wind region of the Antarctic ice sheet, J. Appl. Meteorol., 40, 1952– 1966.

Bintanja, R., and C. H. Reijmer, 2001: A simple parameterization for snowdrift sublimation over Antarctic snow surfaces. *J. Geophys. Res.*, **106,** 31 739–31 748.

Bougeault, P., 1983: A non-reflective upper boundary condition for limited-height hydrostatic models. *Mon. Wea. Rev.*, **111**, 420-429.

Box, J. E. (2001), Surface water vapor exchanges on the Greenland ice sheet derived from automated weather station data, Ph.D. thesis, Univ. of Colo., Boulder.

Box, J. E. (2002), Survey of Greenland instrumental temperature records: 1873–2001, *Int. J. Climatol.*, **22**, 1829– 1847.

Box, J. E., and A. Rinke (2003), Evaluation of Greenland ice sheet surface climate in the HIRHAM regional climate model, *J. Clim.*, **16**, 1302–1319.

Box, J. E., and K. Steffen (2001), Sublimation estimates for the Greenland ice sheet using automated weather station observations, *J. Geophys. Res.*, **106**(D24), 33,965– 33,982.

Box, J.E., D.H. Bromwich, and L.-S. Bai, 2004: Greenland ice sheet surface mass balance 1991-2000: application of Polar MM5 mesoscale model and in-situ data. *J. Geophys. Res.*, **109**, doi:10.1029/2003JD004451.

Bromwich, D.H., 1989: Satellite analyses of Antarctic katabatic wind behavior. *Bull. Amer. Meteor. Soc.*, **70**, 738-749.

Bromwich, D.H., J.J. Cassano, T. Klein, G. Heinemann, K.M. Hines, K. Steffen, and J.E. Box, 2001: Mesoscale modeling of katabatic winds over Greenland with the Polar MM5. *Mon. Wea. Rev.,* **129,** 2290-2309.

Bromwich, D. H., R. I. Cullather, Q.-S. Chen, and B. M. Csatho, 1998: Evaluation of recent precipitation studies for Greenland Ice Sheet. *J. Geophys. Res.,* **103,** 26007-26024.

Bromwich, D.H., Q.-S. Chen, Y.-F. Li, and R.I. Cullather, 1999: Precipitation over Greenland and its relation to the North Atlantic Oscillation. *J. Geophys. Res.,* **104,** 22103-22115.

Bromwich, D.H., F.M. Robasky, R.A. Keen and J.F. Bolzan, 1993: Modeled variations of precipitation over the Greenland ice sheet. *J. Clim.,* **6,** 1253-1268.

Bromwich. D.H., R.-Y Tzeng and T.R. Parish. 1994: Simulation of the modern Arctic climate by the NCAR CCM1. *J. Clim.,* **7,** 1050-1069.

Bromwich, D. H., Y. Du, and K. M. Hines (1996), Wintertime surface winds over the Greenland ice sheet, *Mon. Weather Rev.,* **124,** 1941 – 1947.

Bromwich, D. H., J. Cassano, T. Klein, G. Heinemann, K. Hines, K. Steffen, and J. E. Box (2001a), Mesoscale modeling of katabatic winds over Greenland with the Polar MM5, *Mon. Weather Rev.,* **129,** 2290–2309.

Bromwich, D. H., Q. S. Chen, L. S. Bai, E. N. Cassano, and Y. Li (2001b), Modeled precipitation variability over the Greenland ice sheet, *J. Geophys. Res.,* **106**(D24), 33,891–33,908.

Bromwich, D. H., 1988: Snowfall in high southern latitudes. *Rev. Geophys.,* **26,** 149–168.

——, 1990: Estimates of Antarctic precipitation. *Nature,* **343,** 627–629.

——, and F. M. Robasky, 1993: Recent precipitation trends over thepolar ice sheets. *Meteor. Atmos. Phys.,* **51,** 259–274.

——, ——, R. A. Keen, and J. F. Bolzan, 1993: Modeled variations of precipitation over the Greenland ice sheet. *J. Climate,* **6,** 1253–1268.

——, A. N. Rogers, P. Kallberg, R. I. Cullather, J. W. C. White, and K. J. Kreutz, 2000: ECMWF analyses and reanalyses depiction of ENSO signal in Antarctic precipitation. *J. Climate,* **13,** 1406–1420.

——, J. J. Cassano, T. Klein, G. Heinemann, K. M. Hines, K. Steffen, and J. E. Box, 2001a: Mesoscale modeling of katabatic winds over Greenland with the Polar MM5. *Mon. Wea. Rev.,* **129,** 2290–2309.

Brook, E. J., T. Sowers and J. Orchardo, 1996: Rapid variation in atmospheric methane concentration during the past 110,000 years. *Science,* **273,** 1087-1091.

Buzzi, A., and A. Tibaldi, 1978: Cyclogensis in the lee of the Alps: A case study. *Quart. J. R.*

Budd, W. F., W. R. J. Dingle, and U. Radok, 1966: The Byrd snowdrift project: Outline and basic results. *Studies in Antarctic Meteorology,* M. J. Rubin, Ed., Antarctic Research Series, Vol. 9, Amer. Geophys. Union, 71–134.

Cassano, J.J., J.E. Box, D.H. Bromwich, L. Li, and K. Steffen, 2001: Evaluation of Polar MM5 simulations of Greenland's atmospheric circulation. *J. Geophys. Res.,* **106,** 33,867-33,890.

Chu, P.C., and C.W. Fan, 1997: Sixth-order difference scheme for sigma coordinate ocean models. *J. Phys. Oceanog.,* **27,** 2064-2071.

Carrasco, J.F., and D.H. Bromwich, 1994: Climatological aspects of mesoscale cyclogenesis over the Ross Sea and Ross Ice Shelf regions of Antarctica. *Mon. Wea. Rev.,* **122,** 2405-2425.

Cassano, J.J., J.E. Box, D.H. Bromwich, L. Li, and K. Steffen, 2001: Verification of Polar MM5 simulations of Greenland's atmospheric circulation. *J. Geophys. Res.,* **106,** 33,867-33,890

Chapman, W.L., and J.E. Walsh, 1993: Recent variations of sea ice and air temperature in high latitudes. *Bull. Amer. Meteor. Soc.*, **74**, 33-47.

Chen, Q.-S., 1987: *The dynamics of synoptic and sub-synoptic weather systems*. Science Press (China), 100pp.

Chen, Q.-S., D.H. Bromwich, and L.-S. Bai, 1997: Precipitation over Greenland retrieved by a dynamic method and its relation to cyclonic activity. *J. Clim.*, **10**, 839-870.

Chen, Q.-S. and D.H. Bromwich, 1999: An equivalent isobaric geopotential height and its application to synoptic analysis and a generalized ω –equation in σ –coordinates. *Mon. Wea. Rev.*, **127**, 145-172

Csatho, B., H. Xu, R. Thomas, D. Bromwich, and Q.-S. Chen, 1997: Comparison of accumulation and precipitation maps of the Greenland ice sheet. *Eos. Trans. AGU*, Fall Meet. Suppl. F9.

Cullather, R.I., Bromwich, D.H. and M.C. Serreze, 2000: The atmosphere hydrologic cycle over the Arctic Basin from reanalyses Part I. Comparison with observations and previous studies. *J. Clim.*, **13**, 923-937.

Cappelen, J., B. V. Jørgensen, E. V. Laursen, L. S. Stannius, and R. S. Thomsen (2001), The observed climate of Greenland, 1958–99: With climatological standard normals, 1961– 90, Tech. Rep. 00– 18, 152 pp.,

Chen, Q.-S., D. H. Bromwich, and L.-S. Bai (1997), Precipitation over Greenland retrieved from a dynamic method and its relation to cyclone activity, *J. Clim.*, **10**, 839–870.

Chu, P. C., and C. Fan (1997), Sixth-order difference scheme for sigma coordinate ocean models, *J. Phys. Oceanogr.*, **27**, 2064– 2071.

Church, J. A., J. M. Gregory, P. Huybrechts, M. Kuhn, C. Lambeck, M. T. Nhuan, D. Qin, and P. L. Woodworth (2001), Changes in sea level, in Climate Change 2001: The Scientific Basis, edited by J. T. Houghton et al., pp. 639– 694, Cambridge Univ. Press, New York.

Clark, P. U., N. G. Pisias, T. F. Stocker, and A. J. Weaver (2002), The role of the thermohaline circulation in abrupt climate change, Nature, 415, 863–869, doi:10.1038/415863a.

Cuffey, K. M., and S. J. Marshall (2000), Substantial contribution to sea level rise during the last interglacial from the Greenland ice sheet, *Nature*, **404**, 591–594.

Casey, K. S., and P. Cornillon, 2001: Global and regional sea surface temperature trends. *J. Climate,* **14**, 3801–3818.

Cassano, J. J., J. E. Box, D. H. Bromwich, L. Li, and K. Steffen, 2001: Verification of Polar MM5 simulations of Greenland's atmospheric circulation. *J. Geophys. Res.,* **106**, 33 867–33 890.

Chen, Q.-S., and Y.-H. Kuo, 1992: A harmonic-sine series expansion and its application to the partitioning and reconstruction problem in a limited area. *Mon. Wea. Rev.,* **120**, 91–112.

——, and D. H. Bromwich, 1999: An equivalent isobaric geopotential height and its application to synoptic analysis and a generalized v equation in s coordinates. *Mon. Wea. Rev.,* **127**, 145–172.

——, ——, and D. H. Bromwich, 1996: A balanced ageostrophic initialization with a fixed external wind boundary value for limited-area models. *J. Meteor. Soc. Japan,* **74**, 325–342.

——, L. Bai, and D. H. Bromwich, 1997a: A harmonic-Fourier spectral limited-area model with an external wind lateral boundary condition. *Mon. Wea. Rev.,* **125**, 143–167.

——, D. H. Bromwich, and L. Bai, 1997b: Precipitation over Greenland retrieved by the dynamic method and its relation to cyclonic activity. *J. Climate,* **10**, 839–870.

Colle, B. A., K. J. Westrick, and C. F. Mass, 1999: Evaluation of MM5 and Eta-10 precipitation forecasts over the Pacific Northwest during the cool season. *Wea. Forecasting*, **14**, 137–154.

Comiso, J. C., 2000: Variability and trends in Antarctic surface temperatures from in situ and satellite infrared measurements. *J. Climate*, **13**, 1674–1696.

Csatho, B., H. Xu, R. Thomas, D. Bromwich, and Q.-S. Chen, 1997: Comparison of accumulation and precipitation maps of the Greenland ice sheet. *Eos. Trans. AGU*, Fall Meet. Suppl. F9.

Cullather, R. I., D. H. Bromwich, and M. L. van Woert, 1998: Spatial and temporal variability of Antarctic precipitation from atmospheric methods. *J. Climate*, **11**, 334–367.

Davis, C.A., and K. Emanuel, 1991: Potential vorticity diagnostics of cyclogenesis. *Mon. Wea. Rev.*, **119**, 1929-1953.

Davies, H.C., and A.M. Rossa, 1998: PV frontogenesis and upper-tropospheric fronts. *Mon. Wea. Rev.*, **126**, 1528-1539.

Dorsey, H. G. Jr., 1945: Some meteorological aspects of the Greenland ice cap. *J. Meteor.*, **2**, 135-142.

Doyle, J.D. and M.A. Shapiro, 2000: A multi-scale simulation of an extreme downslope windstorm over complex topography. *Meterol. Atmos. Phys.*, **74**, 83-101.

Drinkwater, K.F. 2004. Atmospheric and sea-ice conditions in the Northwest Atlantic during the decade, 1991-2000. *J. Northw. Atl. Fish. Sci.*, **34**: 1-11.

Dan. Meteorol. Inst., Copenhagen. Cassano, J., J. E. Box, D. H. Bromwich, L. Li, and K. Steffen (2001), Verification of Polar MM5 simulations of Greenland's atmospheric circulation, J. Geophys. Res., 106(D24), 33,867– 33,890.

De'ry, S. J., and M. K. Yau (2001), Simulation of blowing snow in the Canadian Arctic using a double-moment model, Boundary Layer Meteorol., 99(2), 297–316.

De'ry, S. J., and M. K. Yau (2002), Large-scale mass balance effects of blowing-snow and surface sublimation, J. Geophys. Res., 107(D23), 4679, doi:10.1029/2001JD001251.

Delaygue, G., V. Masson, and J. Jouzel, 1999: Climatic stability of the geographic origin of Antarctic precipitation simulated by an atmospheric general circulation model. *Ann. Glaciol.*, **29**, 45–48.

Doran, P. T., and Coauthors, 2002: Antarctic climate cooling and terrestrial ecosystem response. *Nature*, **415**, 517–520.

Douglas, B. C., and W. R. Peltier, 2002: The puzzle of global sea level rise. *Phys. Today*, **55**, 35–40.

Drinkwater, M. R., D. G. Long, and A. W. Bingham, 2001: Greenland snow accumulation estimates from satellite radar scatterometer data. *J. Geophys. Res.*, **106**, 33 935–33 950.

Dudhia, J., 1993: A nonhydrostatic version of the Penn State–NCAR mesoscale model: Validation tests and simulation of an Atlantic cyclone and cold front. *Mon. Wea. Rev.*, **121**, 1493–1513.

ECMWF, 1999: The description of the evolution of the ECMWF forecasting system and corresponding archive. ECMWF, Reading, United Kingdom, 122 pp.

Einarsson, M.A. 1984: Climate of Iceland. World Survey of Climatology, Vol. 15, Climate of the Oceans, edited by H. van Loon, p. 673-697, Elsevier.

Egger, J., 1974: Numerical experiments on lee cyclogenesis. *Mon. Wea. Rev.*, **102**, 847-860.

Francis, J.A., 2002: Validation of reanalysis upper-level winds in the Arctic with independent rawinsonde data. *Geophys. Res. Lett.*, **29**, 10.1029/2001GL014578.

Frei, C. and C. Schaer, 1998: A precipitation climatology of the Alps from high-resolution rain-gauge observations. *Int. J. Climatol.*, **18**, 873-900.

Fettweis, X., J. P. van Ypersele, H. Galle'e, and F. Lefebre (2003), Modelling of the 1991 Greenland summer with the coupled atmosphere-snow regional climate model MAR, paper presented at 7th International Conference on Polar Meteorology and Oceanography, Am. Meteorol. Soc.,

Fletcher, N. H., 1962: *Physics of Rain Clouds.* Cambridge University Press, 386 pp.

Gallee, H., 1998: Simulation of blowing snow over the Antarctic ice sheet. *Ann. Glaciol.*, **26**, 203–206.

Genthon, C., and G. Krinner, 2001: Antarctic surface mass balance and systematic biases in general circulation models. *J. Geophys. Res.*, **106**, 20 653–20 664.

Giovinetto, M. B., and C. R. Bentley, 1985: Surface balance in ice drainage systems of Antarctica. *Antarct. J. U.S.*, **20**, 6–13.

Grell, G. L., J. Dudhia, and D. R. Stauffer, 1994: A description of the fifth-generation Penn State/NCAR Mesoscale Model (MM5). NCAR Tech. Note NCAR/TN-398 1 STR, 122 pp.

Guo, Z., 2002: Spatial and temporal variability of modern Antarctic precipitation. Ph.D. dissertation, The Ohio State University, 150 pp.

——, D. H. Bromwich, and J. J. Cassano, 2003: Evaluation of Polar MM5 simulations of Antarctic atmospheric circulation. *Mon. Wea. Rev.*, **131**, 384–411.

——, ——, and K. M. Hines, 2004: Modeled Antarctic precipitation. Part II: ENSO modulation over West Antarctica. *J. Climate*, **17**, 448–465.

Grell, G.L., J. Dudhia, and D.R. Stauffer, 1995: A description of the fifth-generation Penn State / NCAR mesoscale model (MM5). NCAR Tech. Note NCAR/TN-398+STR.

Gates, W. L., U. Cubasch, G. A. Meehl, J. F. B. Mitchell, and R. J. Stouffer, 1993: An intercomparison of selected features of the control climates simulated by coupled ocean-atmosphere general circulation models. WCRP-82, WMO/TD-No. 574, World Climate Research Program, World Meteorological Organization, Geneva, Switzerland, 46pp.

Geng, Q.-Z. and M. Sugi, 2001: Variability of the North Atlantic cyclone activity in winter analyzed from NCEP-NCAR reanalysis data. *J. Climate*, **14**, 3863-3873.

Georgi, J., 1933: Greenland as a switch for cyclones. *Geograph. J.*, **81**, 344-345.

Grell, G.A., 1993: Prognostic evaluation of assumptions used by cumulus parameterizations. *Mon. Wea. Rev.*, **121**, 764-787.

Grootes, P.M., M. Stuiver, J.W.C. White, S. Johnsen, and J. Jouzel, 1993: Comparison of oxygen isotope records from the GISP2 and Greenland ice cores. *Nature*, **366**, 552-554.

Grootes P. M. and M. Stuiver, 1997: Oxygen 18/16 variability in Greenland snow and ice with 10^{-3} - to 10^{5} -year time resolution. *J. Geophys. Res.*, **102**, 26455-26470.

Guo, Z., D.H. Bromwich, and J.J. Cassano, 2003: Evaluation of Polar MM5 simulations of Antarctic atmospheric circulation. *Mon. Wea. Rev.*, **131**, 384-411.

Galle'e, H., and P. Pettre' (1998), Dynamical constraints on katabatic wind cessation in Ade'lie Land, Antarctica, J. Atmos. Sci., 55, 1755– 1770.

Garratt, J. R. (1994), The Atmospheric Boundary Layer, 334 pp., Cambridge Univ. Press, New York.

Glover, R. (1999), Influence of spatial resolution and treatment of orography on GCM estimates of the surface mass balance of the Greenland ice sheet, J. Clim., 12, 551–563.

Greuell, W., B. Denby, R. S. W. van de Wal, and J. Oerlemans (2001), Ten years of mass-balance measurements along a transect near Kangerlussuaq, Greenland, J. Glaciol., 47(156), 157–158.

Hamilton, R. A., 1958: The meteorology of north Greenland during the midsummer period. *Quart. J. Roy. Meteor. Soc.* **84**, 142-158.

Hastenrath S, and L. Greischar, 2001: The North Atlantic oscillation in the NCEP-NCAR reanalysis. *J. Climate*, **14**, 2404-2413.

Hines, K.M., D.H. Bromwich, and R.I. Cullather, 1997a: Evaluating Moist Physics for Antarctic Mesoscale Simulations. *Annals Glaciol.*, **25**, 282-286.

Hines, K.M., D.H. Bromwich, and Z. Liu, 1997b: Combined Global Climate Model and Mesoscale Model Simulations of Antarctic Climate. *J. Geophys. Res.*, **102(D12)**, 13, 747-13,760.

Hobbs, W. H., 1945: The Greenland glacial anticyclone. *J. Meteor.*, **2**, 143-153.

Hoke, J.E. and R.A. Anthes, 1976: The initialization of numerical models by a dynamical initialization technique. *Mon. Wea. Rev.*, **104**, 1551-1556.

Hoskins, B.J., 1990: Theory of extratropical cyclones. *Extratropical Cyclones*, C. Newton and E.O. Holopainen, Eds., Amer. Meteor. Soc., 63-80.

Hoskins, B.J., M.E. McIntyre, and A.W. Robertson, 1985: On the use and significance of isentropic potential vorticity maps. *Q. J. R. Meteoro. Soc.*, **111**, 877-946.

Hurrell, J.W., 1995: Decadal trends in the North Atlantic Oscillation: regional temperatures and precipitation. *Science*, **269**, 676-679.

Hyannis, Mass., 12– 16 May. Galle'e, H., and P. G. Duynkerke (1997), Air-snow interactions and the surface energy and mass balance over the melting zone of west Greenland during the Greenland Ice Margin Experiment, J. Geophys. Res., 102(D12), 13,813– 13,824.

Hack, J. J., B. A. Boville, B. P. Briegleb, J. T. Kiehl, P. J. Rasch, and D. L. Williamson (1993), Description of the NCAR Community Climate Model (CCM2), NCAR Tech. Note NCAR/TN-382 + STR, 108 pp., Natl. Cent. For Atmos. Res., Boulder, Colo.

Hamilton, G. S., and I. M. Whillans (2000), Point measurements of the mass balance of the Greenland ice sheet using precision vertical GPS surveys, J. Geophys. Res., 105(B7), 16,295– 16,301.

Hanna, E., and P. Valdes (2001), Validation of ECMWF (re)analysis surface climate data, 1979– 1998, for Greenland and implications for mass balance modelling of the ice sheet, Int. J. Climatol., 21, 171–195.

Hanna, E., P. Huybrechts, and T. Mote (2002), Surface mass balance of the Greenland ice sheet from climate analysis data and accumulation/runoff models, Ann. Glaciol., 35, 67– 72.

Henneken, E. A. C., A. G. C. A. Meesters, N. J. Bink, H. F. Vugts, and F. Cannemeijer (1997), Ablation near the equilibrium line on the Greenland ice sheet, southwest Greenland, July 1991, Z. Gletscherkd. Glazialgeol., 33(2), 173– 184.

Huff, R., N. J. Cullen, and K. Steffen (2002), AWS measurements of surface ablation on the Kaltenböck, R., and F. Obleitner, 1999: On a low cloud phenomenon at the Breidamerkurjökull glacier, Iceland. *Boundary-Layer Meteor.*, **92**, 145-162.

Hack, J. J., B. A. Boville, B. P. Briegleb, J. T. Kiehl, P. J. Rasch, and D. L. Williamson, 1993: Description of the NCAR community climate model (CCM2). NCAR Tech. Note NCAR/TN-382 1 STR, 108 pp.

Haltiner, G. J., and R. T. Williams, 1980: *Numerical Prediction and Dynamical Meteorology.* John Wiley and Sons, 477 pp.

Herron, M. M., 1982: Impurity sources of F2, Cl2, NO2, and 3 SO22 in Greenland and Antarctic precipitation. *J. Geophys. Res.*, 4 **87**, 3052–3060.

Hines, K. M., D. H. Bromwich, and Z. Liu, 1997: Combined global climate model and mesoscale model simulations of Antarctic climate. *J. Geophys. Res.*, **102**, 13 747–13 760.

——, ——, and G. J. Marshall, 2000: Artificial surface pressure trends in the NCEP–NCAR reanalysis over the Southern Ocean and Antarctica. *J. Climate*, **13**, 3940–3952.

IPCC working group I, 2001: Climate Change 2001: The scientific basis. Edited by J. T. Houghton, Y. Ding, D.J. Griggs, M. Noguer, P. J. van der Linden and D. Xiaosu, Cambridge University Press, 944pp.

Janjic', Z. I., 1994: The step-mountain eta coordinate model: Further developments of the convection, viscous sublayer, and turbulence closure schemes. *Mon. Wea. Rev.*, **122**, 927–945.

Janssens, I., and P. Huybrechts (2000), The treatment of meltwater retention in mass-balance parameterizations of the Greenland ice sheet, *Ann. Glaciol.*, **31**, 133–140.

Jellinek, H. H. G. (1957), Compressive strength properties of snow, 16 pp., U.S. Army Snow Ice and Permafrost Estab., Hanover, N. H.

Key, J., C. Fowler, J.Maslanik, T. Haran, T. Scambos, andW. Emery (2002), The Extended AVHRR Polar Pathfinder (APP-x) Product, v 1.0, digital media, Space Sci. and Eng. Cent., Univ. of Wisc., Madison.

Krabill, W., W. Abdalati, E. Frederick, S. Manizade, C. Martin, J. Sonntag, R. Swift, R. Thomas, W. Wright, and J. Yungel (2000), Greenland ice sheet: High-elevation balance and peripheral thinning, *Science*, **289**, 428–430.

Kalnay E, and Coauthors, 1996: The NCEP/NCAR 40-year reanalysis project. *Bull. Amer. Meteor. Soc.*, **77**, 437-471.

Kapsner, W.R., R.B. Alley, C.A. Schuman, S. Anandakrishnan, and P.M. Grootes, 1995: Dominant influence of atmospheric circulation on snow accumulation in Greenland over the past 18,000 years. *Nature*, **373**, 52-54.

Kistler, R.E., 1974: A study of data simulation techniques in an autobarotropic primitive equation channel model. M.S. thesis, The Pennsylvania State University, 84 pp.

Kistler, R., and Coauthors, 2001: The NCEP-NCAR 50-year reanalysis: monthly means CD-ROM and documentation. *Bull. Amer. Meteor. Soc.*, **82**, 247-267.

Klemp, J.B., and D.R. Durran, 1983: An upper boundary condition permitting internal gravity wave radiation in numerical mesoscale models. *Mon. Wea. Rev.*, **111**, 430-444.

Kopp, W., and R. Holzapfel, 1939: Beitrage zum Mechanismus des Witterungsverlaufs uber Gronland. *Wiss. Ergeb. Deut. Gronland-Expedition Alfred Wegener, 1929 und 1930/1931*, 4,274-325.

Kristjansson, J.E., and H. McInnes, 1999: The impact of Greenland on cyclone evolution in the North Atlantic. *Q. J. R. Meteorol. Soc.*, **125**, 2819-2834.

Kuo, Y.-H., and S. Low-Nam, 1990: Prediction of nine explosive cyclones over the western Atlantic Ocean with a regional model. *Mon. Wea. Rev.*, **118**, 3-25.

Kuo. Y.-H., R.J. Reed, and S. Low-Nam, 1991: Effects of surface energy fluxes during the early development and rapid intensification stages of seven explosive cyclones in the western Atlantic. *Mon. Wea. Rev.*, **119**, 457-476.

Li, L. and D.H. Bromwich, 2001: Cyclone activity around the Greenland Ice Sheet for last 50 years. 6th Conference on Polar Meteorology and Oceanography. Amer. Met. Soc., San Diego, May 14-18, 2001, 61-64.

Lefebre, F., H. Galle'e, J.-P. van Ypersele, and W. Greuell (2003), Modeling of snow and ice melt at ETH Camp (west Greenland): A study of surface albedo, J. Geophys. Res., 108(D8), 4231, doi:10.1029/2001JD001160.

Li, L., and J. W. Pomeroy (1997), Estimates of threshold wind speeds for snow transport using meteorological data, *J. Appl. Meteorol.*, **36**, 205–213.

Legrand, M., and R. J. Delmas, 1987: A 220-year continuous record of Volcanic H2SO4 in the Antarctic ice sheet. *Nature,* **327,** 671–676.

Liu, H., K. C. Jezek, and B. Li, 1999: Development of an Antarctic digital elevation model by integrating cartographic and remotely sensed data: A geographic information system based approach. *J. Geophys. Res.,* **104,** 23 199–23 213.

Mann, G. W., P. S. Anderson, and S. D. Mobbs (2000), Profile measurements of blowing-snow at Halley, Antarctica, J. Geophys. Res., 105(D19), 24,491–24,508.

Mosley-Thompson, E., J. R. McConnell, R. C. Bales, Z. Li, P.-N. Lin, K. Steffen, L. G. Thompson, R. Edwards, and D. Bathke (2001), Local to regional-scale variability of Greenland accumulation from PARCA cores, J. Geophys. Res., 106(D24), 33,839–33,851.

Mote, T. L. (2003), Estimation of runoff rates, mass balance, and elevation changes on the Greenland ice sheet from passive microwave observations, J. Geophys. Res., 108(D2), 4056, doi:10.1029/2001JD002032.

Murphy, B. F., I. Marsiat, and P. Valdes (2002), Atmospheric contributions to the surface mass balance of Greenland in the HadAM3 atmospheric model, J. Geophys. Res., 107(D21), 4556, doi:10.1029/2001JD000389.

Moss, M. E., C. P. Pearson, and A. I. McKerchar, 1994: The SOI as a predictor of the probability of low streamflows in New Zealand. *Water Resources Res.,* **30,** 2717–2727.

Manley. G., 1938: Meteorological observations of the British East Greenland Expedition 1935-1936. *Q. J. R. Meteorol. Soc.,* **64,** 253-276.

McGinley, J., 1982: A diagnosis of Alpine lee cyclogenesis. *Mon. Wea. Rev.,* **110,** 1271-1287.

McManus, J.F., G.C. Bond, W.S. Broecker, S. Johnsen, L. Labeyrie, and S. Higgins, 1994: High-resolution climate records from the North Atlantic during the last interglacial. *Nature,* **371,** 326-329.

Meehl, G. A., 1997: Modification of surface fluxes from component models in global coupled models. *J. Clim.,* **11,** 2811-2825.

Meehl, G.A., and W.M. Washington, 1990: CO_2 climate sensitivity and snow-sea-ice albedo parameterizations in an atmospheric GCM coupled to a mixed-layer ocean model. *Clim. Change,* **16,** 283-306.

Meehl, G.A. and W.M. Washington, 1995: Cloud albedo feedback and super greenhouse effect in a global coupled GCM. *Climate Dyn.,* **11,** 399-411.

Meyers, M.P., P.J. DeMott, and W.R. Cotton, 1992: New primary ice-nucleation parameterizations in an explicit cloud model. *J. Appl. Meteorol.,* **31,** 708-721.

Meyers, M. P., P. J. DeMott, and W. R. Cotton, 1992: New primary ice-nucleation parameterizations in an explicit cloud model. *J. Appl. Meteor.,* **31,** 708–721.

Morgan, V. I., I. D. Goodwin, D. M. Etheridge, and C. W. Wookey, 1991: Evidence from Antarctic ice cores for recent increases in snow accumulation. *Nature,* **354,** 58–60.

Mosley-Thompson, E., L. G. Thompson, J. F. Paskievitch, M. Pourchet, A. J. Gow, M. E. Davis, and J. Kleinman, 1995: Recent increase in South Pole snow accumulation. *Ann. Glaciol.,* **21,** 131–138.

——, J. F. Paskievitch, A. J. Gow, and L. G. Thomspon, 1999: Late 20th century increase in South Pole snow accumulation. *J. Geophys. Res.,* **104,** 3877–3886.

Oerlemans., J., H. Björnsson, M. Kuhn, F. Obleitner, F. Palsson, C.J.P.P. Smeets, H.F. Vugts and J. De Wolde, 1999: Glacio-meteorological investigations on Vatnajökull, Iceland, summer 1996: An overview. *Boundary-Layer Meteor.,* **92,** 3-26.

Ohmura. A., and N. Reech, 1991: New precipitation and accumulation distribution maps for Greenland. *J. Glaciol.,* **37,** 140-148.

Olafur, H., and H., Olafsson, 2002: Downscaling experiments with the MM5 model. (http://www.vedur.is/english)

Ohmura, A., and N. Reeh (1991), New precipitation and accumulation maps for Greenland, J. Glaciol., 37(125), 140– 148.

Ohmura, A., M. Wild, and L. Bengtsson (1996), A possible change in mass balance of Greenland and Antarctic ice sheets in the coming century, J. Clim., 9, 2124– 2135.

Ohmura, A., P. Calanca, M. Wild, and M. Anklin (1999), Precipitation, accumulation, and mass balance of the Greenland ice sheet, Z. Gletscherkd. Glazialgeol., 35(1), 1– 20.

Oerter, H., F. Wilhelms, F. Jung-Rothenha"usler, F. Go"ktas, H. Miller, W. Graf, and S. Sommer, 2000: Accumulation rates in Dronning Maud Land, Antarctica, as revealed by dielectric-profiling measurements of shallow firn cores. *Ann. Glaciol.,* **30,** 27–34.

Ohmura, A., M. A. Wild, and L. Bengtsson, 1996: A possible change in mass balance of Greenland and Antarctic ice sheets in the coming century. *J. Climate,* **9,** 2124–2135.

Pan, Z., E. Takle, W. Gutowski, and R. Turner, 1999: Long simulation of regional climate as a sequence of short segments. *Mon. Wea. Rev.,* **127,** 308-321.

Parish, T.R. and D.H. Bromwich, 1991: Continental-scale simulation of the Antarctic katabatic wind regime. *J. Climate,* **4,** 135-146.

Pauley, P. M., and S. J. Nieman, 1992: A comparison of quasigeostrophic and nonquasigeostrophic vertical motions for a rapidly intensifying marine extratropical cyclone. *Mon. Wea. Rev.,* **120,** 1108–1134.

Petterssen, S., 1956: *Weather Analysis and Forecasting,* 2nd ed., Vol. I, McGraw-Hill, 428pp.

Petermann Gletscher, Greenland, Eos Trans. AGU, 83(47), Fall Meet. Suppl., F314.

Pfeffer, W. T., M. F. Meier, and T. H. Illangasekare (1991), Retention of Greenland runoff by refreezing: Implications for projected future sealevel change, J. Geophys. Res., 96(C12), 22,117–22,124.

Pinto, J. O., J. A. Curry, A. H. Lynch, and P. O. G. Persson (1999), Modeling clouds and radiation for the November 1997 period of SHEBA using a column climate model, J. Geophys. Res., 104(D6), 6661– 6678.

Pomeroy, J. W., and R. Essery (1999), Turbulent fluxes during blowingsnow: Field tests of model sublimation predictions, Hydrol. Processes, 13, 2963– 2975.

Putnins, P. (1970), The climate of Greenland, in Climates of the Polar Regions, World Surv. of Climatol., vol. 12, edited by S. Orvig, pp. 3–112, Elsevier Sci., New York.

Putnins, P., 1970: The climate of Greenland. *World Survey of Climatology.* Climate of the Polar Regions. Vol.14, Elsevier, 3-109.

Petit, J. R., J. Jouzel, M. Pourchet, and L. Merlivat, 1982: A detailed study of snow accumulation and stable isotope content in Dome C (Antarctica). *J. Geophys. Res.,* **87** (C6), 4301–4308.

Powers, J.G., A.J. Monaghan, A.M. Cayette, D.H. Bromwich, Y-H. Kuo, and K.W. Manning, 2003: Real-time mesoscale modeling over Antarctica: The Antarctic Mesoscale Prediction System (AMPS). *Bull. Amer. Meteor. Soc.,* **84,** 1533-1545.

Qian, J.-H., A. Seth, and S. Zebiak, 2003: Reinitialized versus continuous simulations for regional climate downscaling. *Mon. Wea. Rev.,* **131,** 2857-2874.

Reisner, J., R. M. Rasmussen, and R. T. Bruintjes, 1998: Explicit forecasting of supercooled liquid water in winter storms using the MM5 mesoscale model. *Quart. J. Roy. Meteor. Soc.,* **124,** 1071–1107.

Rinke, A., K. Dethloff, A. Spekat, W. Enke, and J. H. Christensen, 1999a: High resolution climate simulations over the Arctic. *Polar Res.,* **18** (2), 1-9.

Rinke, A., K. Dethloff, and J.H. Christensen, 1999b: Arctic winter climate and its interannual variations simulated by a regional climate model. *J. Geophys. Res.,* **104,** 19027-19038.

Rinke, A., and K. Dethloff, 2000: On the sensitivity of a regional Arctic climate model to initial and boundary conditions. *Clim. Res.,* **14,** 101-113.

Rogers, J.C., 1984: The association between the North Atlantic Oscillation and the Southern Oscillation in the Northern Hemisphere. *Mon. Wea. Rev.,* **112,** 1999-2015.

Rögnvaldsson, O., P. Crochet, and H. Ólafsson, 2004: Estimation of precipitation in complex terrain. 10th Conference on Mesoscale Processes, American Meteorological Society, Boston, P1.19.

Rasmussen, E.A., P.S. Guest, and K.L. Davidson, 1997: Synoptic and mesoscale atmospheric features over the ice-covered portion of the Fram Strait in spring. *J. Geophys. Res.,* **102,** 13975-13986.

Rasmussen, L., 1989: Greenland winds and satellite imagery, VEJRET, special issue in English, Ed. N.W. Nilsen, the Danish Meteorological Society.

Ringler, T.D. and K.H. Cook, 1999: Understanding the seasonality of orographically forced stationary waves: Interaction between mechanical and thermal forcing. *J. Atmos. Sci.,* **56,**1154-1174.

Rogers, J.C., 1984: The association between the North Atlantic Oscillation and the Southern Oscillation in the Northern Hemisphere. *Mon. Wea. Rev.,* **112,** 1999-2015.

Rogers, J.C., and H. van Loon, 1979: The seasaw in winter temperatures between Greenland and northern Europe, part II: Some ocean and atmospheric effects in middle and high latitudes. *Mon. Wea. Rev.,* **107,** 509-519.

Rogers, J. C., and M. J. McHugh, 2002: On the separability of the North Atlantic oscillation and Arctic oscillation. *Clim. Dyn.,* **19,** 599-608.

Rognvaldsson, O., and H. Olafsson, 2002: Mountain waves over Greenland and the icelandic trough. (http://www.vedur.is/~haraldur/rit.html)

Reeh, N., C. Mayer, H. Miller, H. H. Thomson, and A. Weidick (1999), Present and past climate control on fjord glaciations in Greenland: Implications for IRD-deposition in the sea, Geophys. Res. Lett., 26, 1039– 1042.

Rignot, E. J., S. P. Gogineni, W. B. Krabill, and S. Ekholm (1997), North and northeast Greenland ice discharge from satellite radar interferometry, Science, 276, 934– 937.

Reijmer, C. H., M. R. van den Broeke, and M. P. Scheele, 2002: Air parcel trajectories and snowfall related to five deep drilling locations in Antarctica based on the ERA-15 dataset. *J. Climate,* **15,** 1957–1968.

Reisner, J., R. M. Rasmussen, and R. T. Bruintjes, 1998: Explicit forecasting of supercooled liquid water in winter storms using the MM5 mesoscale model. *Quart. J. Roy. Meteor. Soc.*, **124**, 1071–1107.

Schmidt, R. A. (1982), Properties of blowing-snow, Rev. Geophys., 20, 39–44.

Steffen, K., and J. E. Box (2001), Surface climatology of the Greenland ice sheet: Greenland Climate Network 1995 – 1999, J. Geophys. Res., 106(D24), 33,951– 33,964.

Steffen, K., and T. DeMaria (1996), Surface energy fluxes of Arctic winter sea ice in Barrow Strait, J. Appl. Meteorol., 35, 2067– 2079.

Sturm, M., J. Holmgren, M. Ko¨nig, and K. Morris (1997), The thermal conductivity of seasonal snow, J. Glaciol., 43(143), 26– 41.

Sardie, J. M. and T. T. Warner, 1983: On the mechanism for the development of polar lows. *J. Atmos. Sci.*, **40**, 869-881.

Schwerdtfeger, W., 1972: The vertical variation of the wind through the friction-layer over the Greenland ice cap. *Tellus*, **24**, 13-16.

Schwierz, C., R. Fehlmann and H.C. Davies, 1999: Greenland and the ambient synoptic-scale flow. IUGG 1999 Symposia. Birmingham, UK. July 18th-30th, 1999. MI05/E/04-A1

Scorer, R.S, 1988: Sunny Greenland. *Quart. J. Roy. Meteor. Soc.*, **114**, 3-39.

Serreze, M.C., 1995: Climatological aspects of cyclone development and decay in the Arctic. *Atmos.-Ocean*, **33**, 1-23.

Serreze, M. C., J. A. Maslanik, J. R. Key, and R. F. Kokaly (1995), Diagnosis of the record minimum in Arctic sea ice area during 1990 and associated snow cover extremes, Geophys. Res. Lett., 22, 2183–2186.

Serreze, M.C., F. Carse, R.G. Barry, and J.C. Rogers, 1997: Icelandic low cyclone activity: Linkages with the NAO and relationships with recent changes in the Northern Hemisphere circulation. *J. Clim.*, **10**, 453-464.

Stearns, C.R., G.A. Weidner, and L.M. Keller, 1997: Atmospheric circulation around the Greenland Crest. *J. Geophys. Res.*, **102**, 13801-13812.

Steffen, K., and J. Box, 2001: Surface climatology of the Greenland ice sheet: Greenland climate network 1995-1999. *J. Geophys. Res.*, **106**, 33951-33964.

Stoelinga, M.T., 1996: A potential vorticity-based study of the role of diabatic heating and friction in a numerically simulated baroclinic cyclone. *Mon. Wea. Rev.*, **124**, 849-874.

Stull, R.B., 1988: *An Introduction to Boundary Layer Meteorology*. Kluwer Acad. Press. Norwell, Mass.

Sinclair, M. R., 1994: A diagnostic model for estimating orographic precipitation. *J. Appl. Meteor.*, **33**, 1163–1175.

Taylor, K.C., C.U. Hammer, R.B. Alley, H.B. Clausen, D. Dahl-Jensen, A.J. Gow, N.S. Gundestrup, J. Kipfstuhl, J.C. Moore, and E.D. Waddington, 1993: Electrical conductivity measurements from the GISP2 and GRIP Greenland ice cores. *Nature*, **366**, 549-552.

Taylor, K.C., R.B. Alley, G.W. Lamorey, and P.A. Mayewski, 1997: Electrical measurements on the GISP2 core. *J. Geophys. Res.*, **102**, 26511-26517.

Thompson, D. W. J, and J. M. Wallace, 1998: The Arctic oscillation signature in the wintertime geopotential height and temperature fields. *Geophys. Res. Lett.*, 25, 1297-1300.

Thompson, D. W. J, and J. M. Wallace, 2000: Annular modes in the extratropical circulation. Part I: month-to-month variability. *J. Clim.*, **13**, 1000-1016.

Tibaldi, S., A. Buzzi, and A. Speranza, 1990: Orographic cyclogenesis. *Extratropical Cyclones*, C. Newton and E.O. Holopainen, Eds., Amer. Meteor. Soc., 107-127.

Tabler, R. D. (1991), Snow transport as a function of wind speed and height, in Cold Regions Engineering: Proceedings, Cold Regions Sixth International Specialty Conference, pp. 729–738, Tech. Counc. on Comput. in Civ. Eng., Am. Soc. of Civ. Eng., Reston, Va.

Thomas, R. H., and PARCA Investigators (2001), PARCA 2001, Program for Arctic Regional Climate Assessment (PARCA): Goals, key findings, and future directions, J. Geophys. Res., 106(D24), 33,691–33,706.

Thompson, S. L., and D. Pollard (1997), Greenland and Antarctic mass balances for present and doubled atmospheric CO2 from the GENESIS version-2 global climate model, J. Clim., 10, 871–900.

Troen, I., and L. Mahrt (1986), A simple model of the atmospheric boundary layer: Sensitivity to surface evaporation, Boundary Layer Meteorol., 37, 129–148.

Turner, J., T. A. Lachlan-Cope, G. J. Marshall, E. M. Morris, R. Mulvaney, and W. Winter (2002), Spatial variability of Antarctic Peninsula net surface mass balance, J. Geophys. Res., 107(D13), 4173, doi:10.1029/2001JD000755.

Turner, J., W. M. Connolley, S. Leonard, G. J. Marshall, and D. G. Vaughan, 1999: Spatial and temporal variability of net snow accumulation over the Antarctic from ECMWF re-analysis project data. Int. J. Climatol., 19, 697–724.

Uccellini, L.W., 1990: Processes contributing to the rapid development of extratropical cyclones. Extratropical Cyclones, C. Newton and E.O. Holopainen, Eds., Amer. Meteor. Soc., 81-105.

van der Veen, C. J. (2002), Polar ice sheets and global sea level: How well can we predict the future?, Global Planet. Change, 32, 165– 194.

van de Wal, R. S. W., M. Wild, and J. R. de Wolde (2001), Short-term volume changes of the Greenland ice sheet in response to doubled CO2 conditions, Tellus, Ser. B, 53, 94– 102.

van Lipzig, N. P. M., E. van Meijgaard, and J. Oerlemans (1999), Evaluation of a regional atmospheric model using measurements of surface heat exchange processes from a site in Antarctica, Mon. Weather Rev., 127, 1994– 2011.

von Helmholtz, H., 1988: Uber atmospharische Bewegungen. Meteor. Zeit., 5, 329-340.

von Storch, H., H. Langenberg and F. Feser, 2000: A spectral nudging technique for dynamical downscaling purposes. Mon. Wea. Rev., 128, 3664-3673.

van den Broeke, M. R., 1997: Spatial and temporal variation of sublimation on Antarctica: Results of a high-resolution general circulation model. J. Geophys. Res., 102, 29 765–29 777.

Vaughan, D. G., J. L. Bamber, M. Giovinetto, J. Russell, and A. P. R. Cooper, 1999: Reassessment of net surface mass balance in Antarctica. J. Climate, 12, 933–946.

Winebrenner, D. P., R. J. Arthern, and C. A. Shuman, 2001: Mapping Greenland accumulation rates using observations of thermal emission at 4.5-cm wavelength. J. Geophys. Res., 106, 33 919–33 934.

Wingham, D. J., A. J. Ridout, R. Scharroo, R. J. Arthern, and C. K. Shum, 1998: Antarctic elevation change from 1992–1996. Science, 282, 456–458.

Walden, H., 1959: Statistisch-synoptische Untersuchung uber das Verhalten von Tiefdruchgebieten im Bereich von Gronland. Deutscher Wetterdienst, Seewetteramt, 20, 69pp.

White, P. W., 2002: IFS Documentation, Part VI: Technical and Computational Procedures (CY23R4), Ed. P. W. White, 161pp.

Whittaker., L.M., and L.H. Horn, 1984: Northern Hemisphere extratropical cyclone activity for four mid-season months. J. Clim., 4, 297-310.

Warren, S. G. (1982), Optical properties of snow, Rev. Geophys., 20, 67– 89. Wendler, G., C. Stearns, G. Weidner, G. Dargaud, and T. Parish (1997), On the extraordinary winds of Ade'lie Land, J. Geophys. Res., 102(D4), 4463– 4474.

Wild, M., and A. Ohmura (2000), Changes in mass balance of the polar ice sheets and sea level under greenhouse warming as projected in high resolution GCM simulations, Ann. Glaciol., 30, 197– 203.

Wild, M., P. Calanca, S. C. Scherrer, and A. Ohmura (2003), Effects of polar ice sheets on global sea level in high-resolution greenhouse scenarios, J. Geophys. Res., 108(D5), 4165, doi:10.1029/2002JD002451.

Xie, P. P., and P. A. Arkin, 1998: Global monthly precipitation estimates from satellite-observed outgoing longwave radiation. *J. Climate,* **11,** 137–164.

Yen, Y. C., 1981: Review of thermal properties of snow, ice and sea ice. U.S. Army Cold Regions Research and Engineering Laboratory, CRREL Rep. 81-10, 27 pp.

Zwally, H.J., W. Abdalati, T. Herring, K. Larson, J. Saba, and K. Steffen, 2002: Surface melt-induced acceleration of Greenland ice-sheet flow. *Science.,* **297,** 218-222.

Zuo, Z., and J. Oerlemans (1997), Contribution of glacier melt to sea level rise since AD 1865: A regionally differentiated calculation, Clim. Dyn., 13, 835– 845.

Zwally, H. J., and M. B. Giovinetto (2000), Spatial distribution of surface mass balance on Greenland, Ann. Glaciol., 31, 126–132.

Zwally, H. J., and M. B. Giovinetto (2001), Balance mass flux and ice velocity across the equilibrium line in drainage systems of Greenland, J. Geophys. Res., 106(D24), 33,717– 33,728.

Zwally, H. J., W. Abdalati, T. Herring, K. Larson, J. Saba, and K. Steffen (2002), Surface melt-induced acceleration of Greenland ice-sheet flow, Science, 297, 218– 222.